NANOSTRUCTURED ELECTRODES FOR ENERGY CONVERSION

by

RYAN THOMAS TUCKER

A thesis submitted in partial fulfillment of the requirements for the degree of

DOCTOR OF PHILOSOPHY

in

MEMS AND NANOSYSTEMS

Department of Electrical and Computer Engineering
University of Alberta

ABSTRACT

Nanoscale materials offer opportunities to employ unique physical phenomena and performance enhancement in many applications, including energy conversion. The coupling of functional materials properties and nanoscale morphologies is paramount for the successful implementation of nanostructured materials. The central theme of this thesis is the development and testing of functional nanostructured materials motivated by energy conversion applications. First, phase formation and doping are studied for metal oxide thin films comprised of arrays of high aspect ratio nanostructures fabricated by glancing angle deposition (GLAD). Second, morphology of branched nanowire structures is shown to be controllable by geometric modulation of the growth environment with a newly developed combination of vapour-liquid-solid (VLS) nanowire growth and GLAD.

Phase formation in the niobium–oxygen system is systematically explored for nanopillar array thin films. The formation of different oxide and oxynitride phases via high temperature annealing is shown to be dependent on the nanopillar array porosity as well as the annealing gas type and flow. Additionally, annealing-induced morphology changes are shown to be dependent on the degree of oxygen removal during reduction. The util-

ity of niobium oxide nanopillars as supports for platinum electrocatalysis is demonstrated, and the electrochemical performance of the combined catalyst is shown to be related to both the support morphology and phase.

Doping can enhance the electrical properties of metal oxide thin films; however, doping in evaporated thin films is challenging. Niobium doping in electron beam evaporated titanium dioxide thin films is shown to be possible, and the transparent conducting properties of the niobium-doped films are evaluated. The GLAD technique is also used to demonstrate the feasibility of doped nanostructured thin films.

The concept of geometric flux engineering is introduced for the growth of indium tin oxide branched nanowires via VLS-GLAD. A high degree of control over the number, size, and shape of nanowires in an array is demonstrated. Furthermore, diameter oscillation in nanowire branches is observed and a model is constructed to support the proposed mechanism of growth.

The advantages and challenges for nanostructured electrodes are discussed, and further suggestions for future research are made.

PREFACE

This thesis is an original work by Ryan T. Tucker. Significant portions of the thesis have been previously published and were completed in collaboration with other researchers. Throughout the entirety of the work, Prof. M.J. Brett has been the supervisory author, responsible for top-level direction, concept formation, and manuscript refinement.

The work in Chapters 2–4 was initiated as a part of a National Research Council Canada Technology Development Program coordinated by the NRC Institute for Fuel Cell Innovation and in direct collaboration with the group of Prof. D.P. Wilkinson at the University of British Columbia. Chapter 2 was published as R.T. Tucker, M.D. Fleischauer, R.M. Shewchuk, A.E. Schoeller, and M.J. Brett, "Phase formation and morphology control of niobium oxide nanopillars," *Materials Science and Engineering: B* **176**, 626–632 (2011); Chapter 3 was published as A. Bonakdarpour, R.T. Tucker, M.D. Fleischauer, N.A. Beckers, M.J. Brett, and D.P. Wilkinson, "Nanopillar niobium oxides as support structures for oxygen reduction electrocatalysts," *Electrochimica Acta* **85**, 492–500 (2012); and Chapter 4 was published as R.T. Tucker, N.A. Beckers, M.D. Fleischauer, and M.J. Brett, "Electron beam deposited Nb-doped TiO_2 toward nanostructured transparent conductive thin films," *Thin Solid Films* **525**, 28–34 2012. I was responsible for sample preparation, experimental design, morphology and crystallinity characterization, and manuscript composition. R.M. Shewchuk and A.E. Schoeller contributed to sample preparation for the work in Chapter 2. M.D. Fleischauer was responsible for program coordination and made large contributions to crystallinity characterization and analysis, as well as equipment procurement, experimental design, and manuscript preparation. N.A. Beckers contributed to sample preparation, sol-gel synthesis and composition characterization for the work in Chapter 4, and manuscript preparation. A. Bonakdarpour, under the supervision of Prof. D.P. Wilkinson, was responsible for the electrochemistry experiments and analysis included in Chapter 3.

The work in Chapters 5 & 6 are part of a larger body of work studying the concept and implications of vapour-liquid-solid glancing angle deposition. While I originally discovered the VLS-GLAD growth of indium tin oxide branched nanowires in December 2010, the project evolved to a team comprised of myself, A.L. Beaudry, J.M. LaForge, and M.T. Taschuk. Chapter 5 was published as A.L. Beaudry, R.T. Tucker, J.M. LaForge, M.T. Taschuk, and M.J. Brett, "Indium tin oxide nanowhisker morphology con-

trol by vapour-liquid-solid glancing angle deposition," *Nanotechnology* **23**, 105608 (2012) and is included in the patent application R.T. Tucker, A.L. Beaudry, J.M. LaForge, and M.J. Brett, "Branched Nanowires and Method of Fabrication," United States Patent Application #14/092,720 (2013). Parts of Chapter 6 were published as R.T. Tucker, A.L. Beaudry, J.M. LaForge, M.T. Taschuk, and M.J. Brett, "A little ribbing: Flux starvation engineering for rippled indium tin oxide nanotree branches," *Applied Physics Letters* **101**, 193101 (2012). I designed and built the heated stage used for the VLS-GLAD film fabrication and contributed to sample preparation, experimental design, morphology characterization, property–parameter correlation, and manuscript composition. Additionally, I conceptualized and coded the model for diameter oscillations presented in Chapter 6. A.L. Beaudry contributed to sample preparation, morphology measurements, and analysis. J.M. LaForge was responsible for crystallinity characterization and analysis, and contributed insight into kinetic growth and manuscript preparation. M.T. Taschuk was largely responsible for task management, and made significant contributions to concept formation, experimental design, and manuscript preparation. Further reports on the VLS-GLAD technique with significant contributions from each member of the aforementioned team include the following publications: A.L. Beaudry, J.M. LaForge, R.T. Tucker, P. Li, M.T. Taschuk, and M.J. Brett, "Flux engineering for indium tin oxide nanotree crystal alignment and height dependent branch orientation," *Crystal Growth & Design* **13**, 212–219 (2013); M.T. Taschuk, R.T. Tucker, J.M. LaForge, A.L. Beaudry, M.R. Kupsta, and M.J. Brett, "Towards engineered branch placement: Unreal™ match between vapour-liquid-solid glancing angle deposition nanowire growth and simulation," *Journal of Applied Physics* **114**, 244304 (2013); J.M. LaForge, T.L. Cocker, A.L. Beaudry, K. Cui, R.T. Tucker, M.T. Taschuk, F.A. Hegmann, and M.J. Brett, "Conductivity control of as-grown branched indium tin oxide nanowire networks," *Nanotechnology* **25**, 035701 (2014); and A.L. Beaudry, J.M. LaForge, R.T. Tucker, J.B. Sorge, N.L. Adamski, P. Li, M.T. Taschuk, and M.J. Brett, "Directed branch growth in aligned nanowire arrays," *Nano Letters* **14**, 1797–1803 (2014).

All graphics included in this thesis are my original work and should be used only with permission from the assigned copyright holders.

For my grandparents,
Lawrence & Helen Milan
and Bert & Jean Tucker.

ACKNOWLEDGMENTS

I offer my sincere gratitude to all of you who have supported me and the work presented in this thesis. I hope I've managed to name you all here:

Thank you to Prof. Michael Brett, my supervisor, for taking me in when I had far too much hair, for letting me follow my seemingly crazy ideas, for footing the bill, and for mentorship, conversation, and direction far beyond scientific endeavors.

My two mentors, Dr. Michael Fleischauer and Dr. Michael Taschuk. Although always at odds with one another, the two of you have rubbed off on me far more than I would ever want to admit (phrasing?). Your combined and sometimes opposing views and guidance are responsible for any balance and effectiveness I appear to have as a scientist.

The numerous faculty members who have engaged and supported my academic career: Prof. Steve Bergens, Prof. Jillian Buriak, Prof. Raymond DeCorby, Prof. Anastasia Elias, Prof. Mark McDermott, Prof. Jim McMullin, Prof. Karthik Shankar, Prof. Lorenz Sigurdson, Prof. Jeremy Sit, Prof. Douglas Thomson, Prof. Thomas Thundat, Prof. Ying Tsui, and Prof. Jon Veinot. Jillian, your good cop/bad cop demeanor has always been a source of both fear and inspiration. Jeremy, thank you for caring enough to edit this from cover to cover! Dr. Sigurdson, the opportunity that you gave me really set this all in motion.

My many collaborators and co-authors from other institutions: Dr. Arman Bonakdarpour and Prof. David Wilkinson from University of British Columbia; Prof. Benoît Limoges, Prof. Véronique Balland, and Amelié Forget from Univeristé Paris Diderot; and Prof. Erik Bakkers and the Photonics of Semiconductor Nanophysics group from Technische Universiteit Eindhoven.

The organizations who funded me and my work, and the people behind those organizations: Natural Sciences and Engineering Research Council, Alberta Innovates: Technology Futures (previously Alberta Ingenuity), Killam Trust, National Institute for Nanotechnology, and the University of Alberta.

The technical staff who were a constant source of knowledge, support, and often good conversation whenever I sought your expertise: Ben Bathgate, Stephanie Bozic, George Braybrook, Kai Cui, Herbert Dexel, Jason Dibbs, Glenn Elaschuk, Dr. Eric Flaim, Keith Franklin, Melissa Hawrelechko,

Mike Hume, Dr. Dimitre Karpuzov, Terry Kugler, Peng Li, Scott Munro, Martin Riedner, Daniel Salamon, Les Schowalter, and Reiner Schwarze.

The wonderful support staff of the Faculty of Engineering and Department of Electrical & Computer Engineering for going above and beyond your duties to enable me: Pinder Bains, Michelle Foley, Kathleen Forbes, Linda Jiao, Erin Lee, Nona McDonagh, and Sandra Peake-Thibodeau. Most of all thank you to Audrey Lin, for your neverending patience, kindness, and support.

The many colleagues and friends during my time at University of Alberta: Allan Beaudry, Dr. Nicole Beckers, Dr. Louis Bezuidenhout, Diana Car, Leah Coumont, Salma Elmallah, Dr. Sonja Francis, Dr. Nathan Gerein, Balazs Gyenes, Dr. Jane Hall, Dr. Ken Harris, Ikaros Hauge, Dr. Matt Hawkeye, Dr. Peter Hrudey, Dr. Jeff Huang, Graham Hunt, Dr. Steven Jim, Dr. Joel Kelly, Dr. Katie Krause, Josh Krabbe, Martin Kupsta, Dr. Jon Kwan, Dr. Josh LaForge, Abeed Lalany, Dr. Viktor Leontyev, Dr. Ang Li, Dr. Sean McClure, Dr. Shaune McFarlane, Anthony Oko, Dr. Dave Rider, De-ann Rollings, Dr. Jason Sorge, Ryan Shewchuk, Josh Siewert, Dan Smetaniuk, Dr. Michael Thomas, Dr. Jaron van Dijken, Dr. Andy van Popta, Dr. Nick Wakefield, Dr. Brian Worfolk, Dr. Marcel Verheijen, and Dr. Ilaria Zardo.

Specifically, I would like to thank Mike Taschuk, Josh LaForge, and Allan Beaudry for being the most effective team I've ever worked within. The development of VLS-GLAD with you guys will certainly be a highlight of my career.

"Team Fuel Cell" – mainly Mike Fleischauer and Nicole Beckers – we made a great team, but I'm glad we've all found better projects to work on!

Al – my deskmate for far too long. Thanks for the shenanigans, but mostly for having my back in the trenches.

To all of my friends and family away from the academy for the encouragement, and for at least pretending you found my research interesting.

My grandparents, I'm dedicating this to you because I see parts of each of you in the way I work and I carry that proudly with me.

Mom, dad, and Jessica. Thank you for not just supporting me, but being my longest serving fans (and letting me win at the *Memory* game as a kid!). You guys have been there for me my entire life and I would've never made it here without you.

My closest friends – Denise, Mike, Christina – thank you guys for the constant entertainment and the support hidden as mockery. You keep me sane and always on my toes.

Sus. Thank you for being my number one fan, support, and critic. I appreciate you and every little bit of it.

CONTENTS

TABLES

FIGURES

SYMBOLS AND ABBREVIATIONS

α	Glancing deposition angle
β	Peak full-width at half-maximum
$\gamma(t)$	Vapour flux modulation function
$\gamma_{\text{rotation}}(t)$	Flux modulation due to rotation
$\gamma_{\text{shutter}}(t)$	Flux modulation due to shuttering
η	Power conversion efficiency
θ	X-ray diffraction angle
λ	Wavelength
ρ	Resistivity
ρ_{min}	Minimum reported resistivity
ϱ	Mass density
τ_{LS}	Liquid–solid crystallization time
τ_{rot}	Period of rotation
ϕ_{TC}	Haacke figure of merit
φ	Substrate rotation angle
a	Vapour flux envelope constant
d	Crystal layer thickness
r	Radius of droplet and branch
r_0	Initial droplet radius
t	Time
t_{i}	Time step i
t_{max}	Branch growth time
Δt	Time step length
A	Projected vapour area
E_g	Bandgap energy
F_N	Smith and Snyder figure of merit
K	Scherrer equation constant
$\mathcal{L}$	Crystallite size
$L(t)$	Instantaneous branch length

L_{max}	Branch length
M	Molar mass
R	Vapour flux rate
R_s	Sheet resistance
SA_{geo}	Geometric surface area
T	Temperature
T_{vis}	Optical transmittance averaged over visible wavelengths
T_m	Melting temperature
V	Droplet volume
$\dot{V}_{in}$	Rate of incoming volume
$\dot{V}_{out}$	Rate of outgoing volume

ATO	Antimony-doped tin oxide (Sb-doped SnO_2)
AZO	Aluminum-doped zinc oxide (Al-doped ZnO)
BE	Binding energy
CV	Cyclic voltammogram
DSSC	Dye-sensitized solar cell
ECSA	Electrochemical surface area
EDX	Energy dispersive X-ray spectroscopy
FTO	Fluorine-doped tin oxide (F-doped SnO_2)
GLAD	Glancing angle deposition
HRTEM	High-resolution transmission electron microscopy
ITO	Indium tin oxide (Sn-doped In_2O_3)
LED	Light-emitting diode
NP	Nanoparticle
NSTF	Nanostructured thin film
OCP	Open circuit potential
OLED	Organic light-emitting diode
ORR	Oxygen reduction reaction
PDF	Powder diffraction file
PLD	Pulsed laser deposition
QCM	Quartz crystal monitor
RDE	Rotating disk electrode
RHE	Reversible hydrogen electrode
SAED	Selected-area electron diffraction
SEF	Surface enhancement factor

SEM	Scanning electron microscopy
TCO	Transparent conductive oxide
TEM	Transmission electron microscopy
TNO	Niobium-doped titanium oxide (Nb-doped TiO_2)
TTFT	Transparent thin film transistor
VLS	Vapour-liquid-solid
VLS-GLAD	Vapour-liquid-solid glancing angle deposition
XPS	X-ray photoelectron spectroscopy
XRD	X-ray diffraction

1

Background

1.1 Energy

The current outlook on global energy usage clearly indicates that fossil fuel based energy sources are unsustainable. Such energy sources face the issues of both limited cost-appropriate supply and high greenhouse gas emissions, neither of which is easily solved [1]. With this era of inexpensive liquid fuels nearing its end, alternative energy sources are of great social, commercial, and academic interest. The total global energy consumption as reported by the BP Statistical Review of World Energy 2013 [2] is shown in Figure 1.1. Energy usage has beyond tripled in the past 50 years. At the same time as this upward trend is broken, traditional energy sources must be replaced with sustainable alternatives in order to mitigate the side effects of energy overuse in a growing population.

A large variety of alternative energy sources have been suggested, most involving capture of power from natural sources such as sunlight, wind, tidal forces, and geothermal heat. Other alternative energy concepts involve fuels or chemical reactions with fewer harmful by-products (such as bio-fuels and hydrogen). The ultimate future energy landscape will likely be

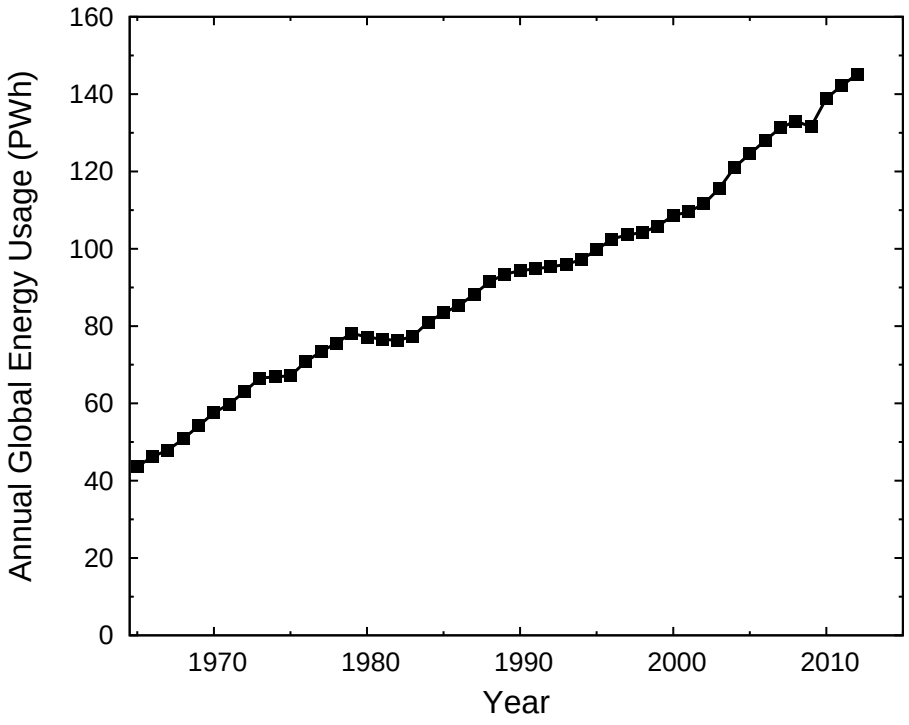

Figure 1.1. *Total annual worldwide energy consumption from 1965 to 2012. Data from [2].*

a mixture of energy sources specifically tailored to regional resources and needs. While numerous options for alternative energy are available, most still require either improved performance or reduced cost in their respective fabrication or energy extraction processes to become commercially viable solutions. In essence, alternative energy sources are widely known, but *energy conversion* will be the key to widely accessing sustainable energy and converting to and from stored energy. Continued development of efficient, sensible energy conversion devices and processes is imperative for moving toward a future with a sustainable, stable energy supply.

Energy is mainly found or used in light, heat, mechanical, electrical, or chemical form. Of these forms of energy, electrical energy is particularly

notable as it has been widely accepted as a standard means of transporting energy to end use. The electrical grid offers significant infrastructure and inertia to develop systems that convert from sustainable energy sources to electrical energy. While the electrical grid paradigm is itself open for mass innovation, new energy conversion technology that can fit within the existing framework is essential for improving energy usage in the near term. Of the multitude of energy conversion processes currently under research, development, or deployment, this research will focus on materials development for photovoltaic and electrochemical conversion. Photovoltaic devices convert energy from light to electricity and electrochemical cells convert chemical energy into electrical energy.

Materials are at the heart of energy conversion, and further development of advanced functional materials will lead the way for more efficient use of more sustainable energy sources. The focus of this thesis is the development of the very materials required for improved generations of energy conversion devices. Nanoscale features offer significant opportunity for surface area and structural engineering in energy conversion devices. The successful combination of nanostructured morphology with specific material properties is crucial. Herein, methods for making desirable nanostructured materials are presented and demonstrated through extensive experimental work. The advanced materials are characterized, analyzed, and in some cases modeled to offer understanding of how both functional properties and nanoscale morphologies can be simultaneously designed for.

This introduction chapter is structured as follows: the opportunity for nanoscale engineering to impact energy conversion processes will be explored, along with the primary fabrication techniques used throughout this thesis. (Section 1.2). A basic introduction and discussion of device limitations is given for each of photovoltaic devices (Section 1.3) and electrochemi-

cal cells (Section 1.4). The background and current state-of-the-art of each of nanostructured fuel cell catalyst supports and three-dimensional transparent electrodes will then be reviewed (Sections 1.5 & 1.6, respectively) before an outline of the remainder of the thesis (Section 1.7).

1.2 Nanostructured Materials

The unifying theme for the two classes of energy conversion device discussed to this point is the concept of using of high surface area electrodes in an attempt to improve performance.

A roughened surface has a higher surface area than its footprint area. This *surface enhancement factor* (the ratio of the real surface area to the geometric footprint area) is always greater than or equal to unity, and increases with roughness or porosity. Higher surface areas are achieved in surfaces with high aspect ratio features, but this increase in feature dimensions normal to a flat surface requires more material and changes the overall morphology. For a topology of a given height, increasing the number density while maintaining the same aspect ratio of features results in an increased surface area. Reducing features below $\sim$μm in size to the nanoscale regime enables surfaces that appear macroscopically flat, but can have surface area enhancements on the order of 10 to 100 times. Herein lies the power of using nanostructuring – a very small amount of material can be exploited for an incredibly high surface area.

Nanostructures can be synthesized in many shapes and varieties, but in general can provide extremely high surface areas with a very small amount of material. In the case of nanostructured electrodes, the best configuration consists of high aspect ratio nanostructures affixed to a common conductor. In practice, a planar conductor with high aspect ratio nanostructures protruding normal to the surface gives both a high surface area and elec-

trical access to each of the structures. This "nanopillar array" architecture has been used for a wide variety of applications [3], including high surface area sensors [4–6], transistors [7], biological interaction devices [8–10], electrodes for displays [11] and solar cells [12–14], and catalyst supports for electrochemistry [15] or water splitting [16, 17].

In each of these different applications, material properties are of equal importance to the nanostructured morphology. The marriage of functional properties to controllable nanoscale morphology adds a layer of complexity to nanostructured electrode fabrication. Composition, crystallinity, and surface properties must be considered and controlled in addition to impurities and defects to achieve the desired combination of optical, electrical, chemical, and mechanical properties in a nanostructured material. As such, a significant portion of this thesis project has been devoted to the exploration and development of nanostructures with distinct functional properties before any demonstration of application.

Of the many different ways of producing nanostructures, two methods are heavily used in this project. Glancing angle deposition and vapour-liquid-solid nanowire growth are reviewed in Sections 1.2.1 and 1.2.2, respectively.

1.2.1 Glancing Angle Deposition

Glancing angle deposition (GLAD) is directed self-assembly technique used for fabricating nanostructured thin films [18–20]. The GLAD technique uses geometrical shadowing of highly collimated vapour flux to drive columnar thin film growth. Through engineering of the flux geometry during growth, arrays of complex nanostructures can be sculpted using this technique.

The basic premise of GLAD thin film growth is shown in Figure 1.2. When a substrate is tilted at a large angle (depicted as α, the deposition

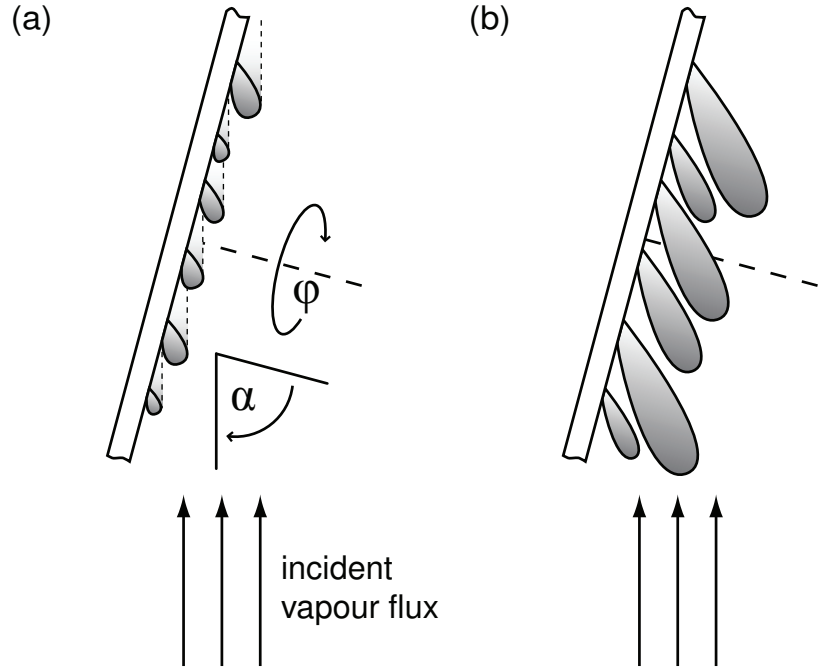

Figure 1.2. *Schematic representation of columnar thin film growth via glancing angle deposition. Vapour flux is incident on the substrate at a highly oblique angle α from the substrate normal. Rotation about substrate normal by angle φ can be used for complex structure control.*

angle) relative to a collimated vapour source, nucleating film material casts trailing shadows from the vapour incident on the surface (Figure 1.2(a)). These shadowed regions prevent incident vapour from reaching the surface or film nuclei behind topological features, thus promoting growth of the highest features. This process results in the competitive growth of columnar features, as shown to develop in Figure 1.2(b). The most basic case results in the formation of an array of tilted columns. The addition of controlled rotation about the substrate normal axis (by the azimuthal angle φ) enables changes in the direction of shadowing, and therefore makes more complex

structures possible. Nanostructured films comprised of arrays of slanted posts, vertical posts, zig-zags, helices, and polygonal spirals – and vertical combinations thereof – have all been demonstrated by GLAD [20].

The GLAD technique has been used for nanostructuring of metals, semiconductors, oxides, and organic materials. In fact, GLAD is nearly material independent and can be used for essentially any material which can be formed into a collimated vapour and subsequently condensed on a surface. This material non-specificity is one of the most appealing features of GLAD, meaning that the technique can be used to create nanostructured thin films of materials for which chemical synthesis routes have not yet been developed.

The properties of GLAD films have been extensively reported on by previous researchers [20]. For application as a nanostructured electrode, the surface area of GLAD films is highly important. Krause *et al.* [21, 22] have reported a detailed study of the surface area of TiO_2, SiO_2, and SnO_2-In_2O_3 GLAD films, revealing several important conclusions. Early studies of obliquely deposited films showed increasing intercolumn separation with increasing α, so it should be expected that the surface area of GLAD films is highly dependent on the deposition angle. In addition to the intercolumn spacing, α also affects the micro- and mesoporosity of the film columns, which is present as a fine, "feathery" microstructure [23]. The $\sim$nm sized pores are responsible for an order of magnitude enhancement in surface area compared to the solid geometry of only the columns, and are especially important to consider when GLAD films interact with gas and liquid phases [24, 25].

Chapters 2–4 use GLAD for fabrication of nanopillar metal oxide thin films. Crystal phase formation (Chapter 2) and composition (Chapter 4) are studied to achieve desirable properties for application demonstration

(Chapter 3). The geometric principles of GLAD are then used to affect kinetic crystal growth in Chapters 5 and 6.

1.2.2 Vapour-Liquid-Solid Nanowire Growth

The vapour-liquid-solid (VLS) growth mechanism allows for the crystalline growth of nanowires [26–28]. VLS growth exploits the solubility of one material in another near supersaturation at temperatures above the mixture's eutectic point. A schematic of the process is shown in Figure 1.3. A liquid "catalyst" droplet is used to mediate the phase reaction by collecting growth material from the vapour phase. After continued collection of growth material, the catalyst droplet will become supersaturated with the growth material, and under ideal conditions will precipitate a solid crystal of the growth material from the catalyst. Under stable temperature and vapour source conditions, layers will continue to precipitate, making high aspect ratio crystal growth possible.

The first demonstration of VLS growth was for Si whiskers using Au as a catalyst material [26]. While the Au/Si system remains the archetype for VLS growth, numerous other materials have demonstrated Au-catalyzed VLS growth: group IV materials (Ge [29], $Si_{1-x}Ge_x$ [30]), III–V materials [31] (e.g., GaP [32], InP [33], InSb [34]), and oxide materials (e.g., Sn-In_2O_3 [35], ZnO [36]). Additionally, VLS growth can be mediated by other metals, such as In-catalyzed Si [37], Sn-catalyzed Si [38], and In-catalyzed InAs [39]. In addition to two-material catalyst/growth systems, self-catalyzed VLS growth has been documented. Of specific interest to the research presented here, indium tin oxide (Sn-In_2O_3 or ITO) undergoes self-catalyzed VLS growth at a relatively low temperature [40]. In this case, In-Sn acts as a liquid droplet with In-Sn-O as a growth material.

In contrast to the GLAD process described in the previous section, VLS-

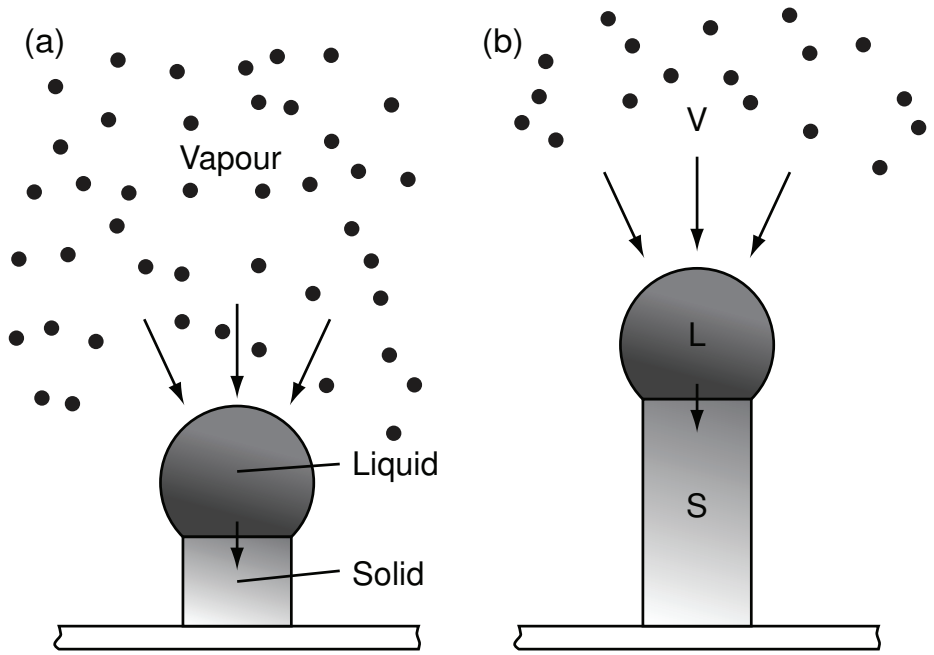

Figure 1.3. *Schematic representation of the vapour-liquid-solid growth mechanism. The liquid catalyst droplet (L) collects growth material from the vapour phase (V) and precipitates a solid crystal (S).*

grown nanostructures have a number of different properties which make them appealing in certain applications, including single crystal structures and low-dimensionality. However, the VLS reaction is not universal, as it depends entirely on the temperature–phase behavior of the materials in question. For this reason, VLS growth is not an option for many materials. VLS growth also offers limited control over shape, size, and spacing of nanostructured features, all of which the GLAD process is well suited for.

Different nanostructuring techniques are better suited for attaining different types of properties, as is evidenced by the contrast between the physical GLAD and chemical VLS methods. Chapters 5 and 6 are focused on

using a hybrid VLS-GLAD growth to achieve high controllable morphology single-crystal branched ITO nanowires for high surface area transparent conducting applications.

1.3 Photovoltaic Devices

Photovoltaic devices convert energy in the form of photons to conducting electrons [41, 42]. In practice, photovoltaics are typically aimed at capturing energy from the sun, and most are designed to most efficiently match the solar spectrum. The basic operation of a photovoltaic device involves (i) the absorption of light as excitons, (ii) the dissociation excitons into charge carriers, and (iii) the collection of charges from the device. Balancing and improving the efficiency of each of these three steps is the route to improving the overall conversion efficiency of a photovoltaic device.

Photovoltaics are widely commercially available in many forms, however, there are very few places in the world where photovoltaic devices are used for significant primary power generation. The wide-spread use of solar cells for utility power generation is limited by the cost/power ratio compared to other energy sources. Reducing the lifetime $/W of photovoltaic devices through a combination of reduced cost (manufacturing and installation), improved lifetime, and increased power conversion efficiency will make photovoltaics increasingly viable for utility-scale power generation.

Semiconductor materials are used in photovoltaic devices, with crystalline Si accounting for the large majority of manufactured photovoltaic devices [41]. While Si-based photovoltaics are the incumbent – largely due to Si processing knowledge transferred from the semiconductor electronics industry [41, 43] – numerous other photovoltaic material systems have been demonstrated, including thin film photovoltaics (CdTe [44, 45], chalco-

genides [46,47], or amorphous Si [43]), organic photovoltaics (OPVs) [48–51], and quantum dot solar cells [52, 53]. The dawn of these new photovoltaic technologies promised simultaneous "low cost" and "high performance" energy conversion in mechanically flexible packages; however, in recent years large scale crystalline Si photovoltaic manufacturing has continued to improve performance while cutting costs. This effect of the economics of scale has left many new technologies very far behind in $/W metrics, meaning the cost-case for thin film and organic photovoltaics may never materialize.

Nonetheless, while there was a large scale opportunity for high performance organic photovoltaic devices at the beginning of this research project, there continues to be niche opportunities and scientifically interesting discoveries for the field.

1.3.1 Organic Photovoltaic Devices

Organic photovoltaic devices (OPVs) operate in a very similar manner to inorganic photovoltaic devices, absorbing light and converting the energy into electrical charges. However, rather than utilizing a *p-n* junction for absorption and charge separation, the photoactive layer in OPVs consists of an electron-*donor* and electron-*acceptor* heterojunction [54]. Photons are absorbed by the acceptor layer as an exciton (a bound electron–hole pair). If the exciton diffuses to a donor–acceptor junction before relaxing as thermal energy, it will dissociate into an electron in the acceptor layer and hole in the donor layer. Early OPV devices used planar bi-layer heterojunctions [48], where the donor and acceptor were thin ($\sim$100 nm) layers between one transparent and one metal electrode. Advancements in OPV design introduced the *bulk heterojunction* (architecture shown in Figure 1.4) to overcome limited exciton diffusion lengths. A bulk heterojunction photoactive layer is a finely mixed layer of donor and acceptor material, each with $\sim$nm sized

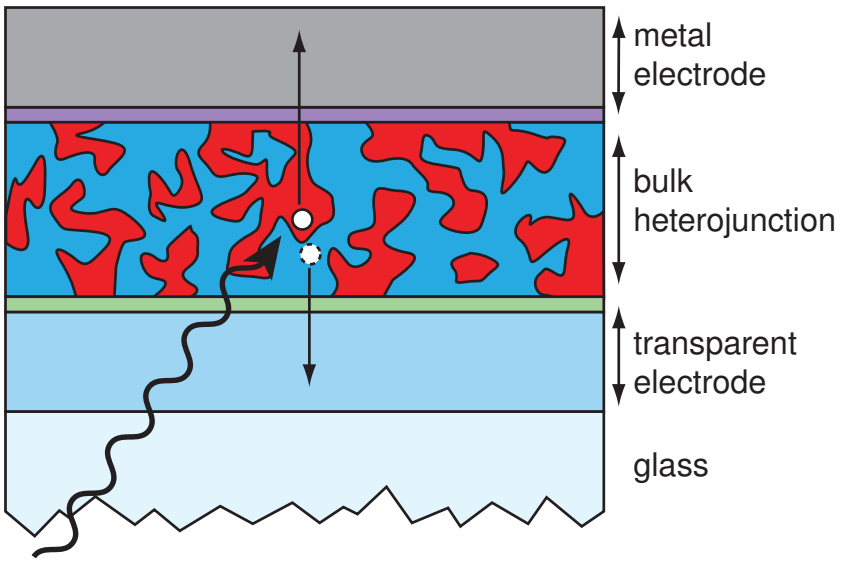

Figure 1.4. *Schematic representation of a typical organic photovoltaic device with a bulk heterojunction photoactive layer sandwiched between transparent and metal electrodes. Layers without labels correspond to commonly used charge injection layers.*

domains [55]. While the bulk heterojunction concept vastly improved the performance (specifically improved short circuit current leading to increased power conversion efficiency) of OPV devices, several limitations still exist.

The record power conversion efficiency for research grade OPV cells has improved from $\eta \approx 5\%$ [56] to $\eta \approx 11\%$ [57] during the time of this research; however, this performance is still lower than inorganic devices based on either crystalline Si or thin film materials. OPV efficiency is limited by light absorption, as many organic materials have limited absorption outside of visible wavelengths. Additionally, charge extraction in most OPV photoactive materials require thin layers, which generally do not absorb all available light. OPV efficiency is also limited in the exciton dissociation and charge extraction processes, with electrons and holes often recombining in the bulk

heterojunction before extraction.

Many approaches have been taken to ameliorate the different loss mechanisms in OPV devices. Better processing and new materials with superior intrinsic absorption or charge transfer properties have shown improvements to OPV performance. Another way to overcome device limitations is to change the OPV device architecture, as was done with the introduction of the bulk heterojunction. The use of nanostructured electrodes to improve the performance of OPVs is discussed in Section 1.6.2.

1.4 Electrochemical Cells

Electrochemical cells convert energy between chemical bonds and electricity. While some electrochemical cells can cause chemical reactions with the introduction of electrical energy, we are most interested in the class of electrochemical devices which extract electrical energy from chemical reactions for this background discussion.

Electrochemical fuel cells (often referred to simply as "fuel cells") are devices which facilitate a chemical reaction to extract energy stored in chemical bonds of a fuel and convert it into an electrical current. All fuel cells consist of an anode, a cathode, and an electrolyte to transfer charge, however, the materials and design of each of these components vary depending on the fuel and operation conditions of the cell. Fuel cells typically use a catalyst to enact oxidation or reduction reactions at the anode and cathode.

Fuel cells have been proposed as a potential solution for future power generation, specifically in remote and mobile applications. Currently, fuel cells are commercially available for remote power generation, however automobile fuel cells remain largely stalled in wide-spread availability and adoption [58]. Automobile fuel cells are hindered by three factors: (i) infrastructure, (ii) cost, and (iii) performance [59]. Infrastructure is an issue for

automobile fuels cells as the so-called "hydrogen economy" is necessary for dispersed fueling stations to make fuel cell-based transportation a viable option [58]. As with many infrastructure issues, it is very much a chicken-and-egg problem, where hydrogen production and fueling stations will not be invested in until fuel cell automobiles are more widely used; yet, fuel cell vehicles will not be widely adopted until fueling stations become more available.

Fuel cell cost and performance are linked, as is the case in many energy conversion devices, where cost/power is a very important metric. Performance includes output power, conversion efficiency, and durability, however for mobile applications, weight and size are also restrictions. Where cost is concerned, the largest cost component in vehicle fuel cells is the catalyst, which is typically Pt [60]. Recent reports calculate 72–94 g of Pt in an 85 kW automotive fuel cell stack, which at conservative estimates of \$45/g accounts for \$3,000–\$4,000 for Pt cost alone. Therefore, to improve the commercial viability of fuel cells for vehicles, power and durability must be increased while reducing the total mass of catalyst used in the cell. Research in non-noble metal catalysts may offer solutions for inexpensive catalyst layers in the future [61], but low-cost, high-performance alternatives have yet to be demonstrated.

Several different types of fuel cells exist, including those that operate at low temperatures ($<$100 °C, such as proton exchange membrane fuel cells) and those that operate at much higher temperatures ($>$700 °C, such as solid oxide fuel cells) [62]. Proton exchange membrane fuel cells have many properties which make them appealing for mobile applications, including fast start-up, responsive power density, reasonable size, and acceptable operating temperatures [63, 64]. For these reasons, significant research efforts continue to drive PEMFC development with the hopes of large-scale impact

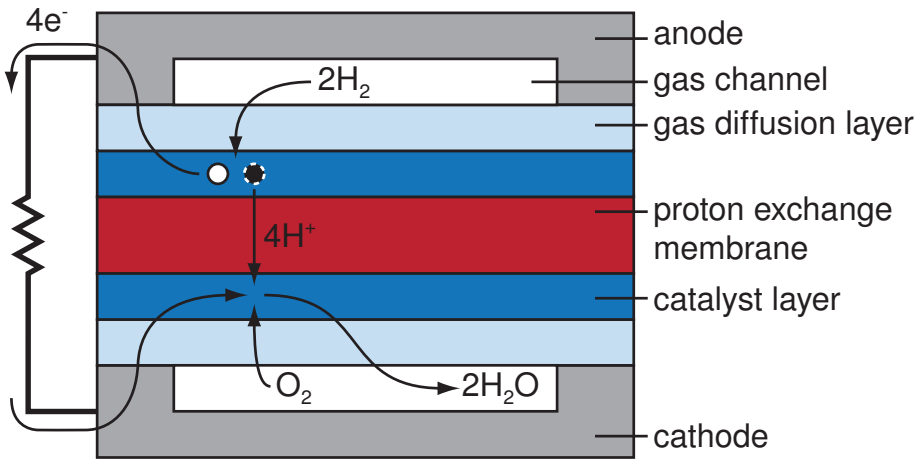

Figure 1.5. *Schematic representation of a single proton exchange membrane fuel cell and ideal process steps for hydrogen fuel reaction.*

on the automobile industry.

1.4.1 Proton Exchange Membrane Fuel Cells

Proton exchange membrane fuel cells – also known as polymer electrolyte membrane fuel cells (PEMFCs) – are hydrogen-fueled electrochemical cells. Typically, PEMFCs are complex multilayer devices, with a proton exchange membrane sandwiched between gas diffusion layers, catalyst electrodes, and flow field plates as depicted in Figure 1.5. Hydrogen fuel is oxidized at the anode into protons and electrons, and oxygen is reduced at the cathode into oxygen ions. Protons travel through the electrically insulating proton exchange membrane, while electrons create an electrical current which can do work in an external circuit. The protons, electrons, and oxygen ions then react producing water, which is the product of the reaction cell.

For this discussion, the limitations of current PEMFCs are more impor-

tant than the specifics of operation. Commercial PEMFCs most often use Pt supported on porous C as a catalyst layer. While these Pt/C catalyst layers have been demonstrated as manufacturable, there are many issues with both performance and lifetime mostly attributed to corrosion and water management issues [62, 65]. The small ∼nm-sized Pt particles have very high surface area; however, the random nature of the porous C network renders a notable fraction of the Pt nanoparticles electrically isolated. The performance per mass of Pt must be maximized in order to justify its inclusion in the cell. Furthermore, the Pt tends to migrate on the support and agglomerate during extended operation, leading to degradation in output power. Nanostructured catalyst supports have been demonstrated as a route to simultaneously improving the performance and durability of Pt-based fuel cell electrodes. The use of nanostructured catalyst supports is discussed in further detail in Section 1.5.2.

1.5 Fuel Cell Catalyst Supports

The catalyst layers are the core of the modern PEMFC design, acting as the site of the chemical reactions responsible for energy conversion in the cell. Catalyst layers exist between the electrolyte (membrane) and gas diffusion layers in each half cell, as shown in Figure 1.5. In the case of H_2/air-fed PEMFCs, oxidation of H_2 occurs at the anode and reduction of O_2 occurs at the cathode. Electrocatalysis at the anode turns out to be relatively easy, and Pt and other metal surfaces have been well developed at PEMFC anodes for quite some time [62]. The O_2 reduction reaction at the PEMFC cathode, however, has proved to be more difficult and considerable development is still required.

Pt and Pt-alloys have been the primary material of interest for cathodes, as these materials exhibit relatively high activity toward O_2 reduction [60,66].

Unfortunately, Pt- and other noble metal-based catalysts are prohibitively expensive to be used in large amounts, and must be carefully dispersed to maximize performance/cost. For this reason, catalyst supports are used to physically hold and electrically connect dispersed catalyst particles. In the ideal case, the functional catalyst material could be minimized to a monolayer-thick skin on an inexpensive support, offering optimal diffusion of reactants and products. Desirable materials for PEMFC catalyst supports should possess high electrical conductivity, high surface area, and high electrochemical stability in a corrosive fuel cell operating environment [67, 68]. Beyond this basic combination of properties, catalyst supports which lend to easy recovery of catalyst metals after disposal have an added advantage.

The following sections explore current commercial and state-of-the-art catalyst support materials as well as nanostructured fuel cell catalyst supports.

1.5.1 Catalyst Support Materials

The most popular PEMFC catalyst–support combination is Pt/C, where the C support is often Vulcan XC-72 or BP-2000 carbon black [69]. Finely ground C powders and inks have been traditionally used due to their high surface area, electrical conductivity, and ease of preparation and application to membrane (i.e., Nafion) layers. However, these uncontrolled dispersions can lead to poor catalyst usage and also have poor durability. Electrochemical surface area of the catalyst is lost during operation due to dissolution and agglomeration of the Pt nanoparticles or corrosion of the C support [64, 70]. In response, a variety of alternative, non-C materials have been explored as catalyst supports.

C-free catalyst supports have been explored across a wide array of material classes: metals, carbides, nitrides, oxides, and polymers [67, 70]. In

each case, researchers are seeking a material which has facile synthesis and exhibits some combination of the desired properties mentioned in the previous section. Antolini *et al.* [67], Shao *et al.* [68], and Wang *et al.* [70], among others, have reviewed the subject extensively.

Transition metal carbides have been utilized as catalyst supports since the 1970s and some (i.e., tungsten carbide – WC) have been shown to exhibit Pt-type electrocatalytic properties themselves. In fact, WC is thought to be the most promising of the transition metal carbide materials because of its low electronic resistivity (10^{-5} Ω cm), synergistic catalysis, and high resistance to catalyst poisons [68]. Regardless of the theoretically desirable properties of the WC catalyst support, Pt/WC catalysts are still reported with low electrochemical surface areas and poor performance requiring further development [71].

Metal oxide materials have also been extensively explored as catalyst supports. With electrical conductivity as a main limiting factor, many metal oxides are inexpensive and highly stable in under fuel cell operating conditions. While many intrinsic bulk metal oxides are electrically insulating, many sub-stoichiometric, doped, and nanostructured metal oxides have been shown to have acceptable electrical conductivity for catalyst support applications [67]. Primary interest has been in Sn-, Ti-, and W-based oxides; however, many other metal oxides have also been considered. The prime example of a sub-stoichiometric oxide catalyst support is the Ti-O system [72]. The so-called Magnéli phase materials of the form Ti_nO_{2n-1} possess relatively low electrical resistivity (10^{-4} Ω cm) and have been commercialized as a mixture containing several conductive Ti-O phases (Ti_3O_5, Ti_4O_7, etc.) [73]. The Nb-O system has received attention in recent years as NbO_2 has been singled out as having stability second only to TiO_2 and synergistic catalytic effects have been observed with Pt/Nb-O electrocatalysts [74,75]. Addition-

ally, while the NbO_2 phase is semiconducting (10^4 Ω cm), the NbO phase has a very low resistivity for an intrinsic metal oxide (10^{-4} Ω cm). Chapter 2 unfolds a systematic study of phase formation in high surface area nanostructured Nb-O, followed by a demonstration of the electrocatalytic potential of nanopillar Nb-O films in Chapter 3.

Metal-doping in TiO_2 has also been used as a route to attaining high electrical conductivity, with interstitial dopants of many different metals (e.g., Cr, W, Mo, Fe, Nb) attempted [76]. Many groups have shown Nb-doping of TiO_2 to be highly effective in enhancing the electrical conductivity with examples as transparent conductors and catalyst supports [77,78]. Specifically, Nb-TiO_2-supported Pt electrocatalysts have shown enhanced stability in comparison to the sub-stoichiometric Ti-O phases in addition to excellent electronic properties [78]. While promising results have been shown for the Nb-TiO_2 material itself, the combination of good composition control and high surface area nanoscale morphology is a necessity for commercial device applications. Chapter 4 will focus on composition control of Nb-TiO_2 for compatibility with the GLAD nanostructuring process.

1.5.2 Nanostructured Catalyst Supports

High surface area is highly sought after in PEMFC catalyst supports. Traditionally, powders and porous materials were used to achieve high surface area by decorating with small catalyst particles. While reasonable performance has been achieved using these stochastic morphologies, valuable catalyst material tends to be rendered inactive due to limited electronic or gas pathways resulting from the random nature of the support. High aspect ratio nanostructures, as introduced in Section 1.2, offer a superior architecture for good gas diffusion pathways, high surface area, and superior electrical connection.

Possibly the most widely known nanostructured catalyst support is the 3M Nanostructured Thin Film (NSTF) support [15, 79]. Developed in the mid-1990s, the nanowire network support is synthesized from an organic perylene material and has very high surface area. Debe *et al.* have shown Pt/NSTF electrocatalysts to have simultaneously higher activity and better voltage stability in direct comparison against Pt/C. The enhanced activity is attributed to the pseudo-ordered nature of the perylene wires, offering a large, accessible reaction surface. The high stability comes from a comparatively low increase in Pt grain size, attributed to the skin-like structure of the Pt on the support [15]. A variety of catalysts [80–82] and underlayers [83] have been tailored to the 3M NSTF supports, however, wide commercial application has yet to be achieved.

While the 3M NSTF support has changed the paradigm for nanostructured PEMFC catalyst supports, the perylene material is inherently limited to low temperature processes. Furthermore, the NSTF support material is electrically insulating, and relies on conduction though the Pt catalyst layer for electrical connection. These limiting factors leave an opportunity for thermally stable, electrically conductive materials of a similar morphology.

Several groups have used high aspect ratio C nanostructures such as carbon nanotubes and carbon nanorods a support materials [84,85]. Gasda *et al.* used patterned substrates and the GLAD nanostructuring process for highly controlled inter-nanorod porosity; the Pt/C nanorods with engineered pores were measured to have twice the current density of typical Pt/C nanorods which was attributed to enhanced O_2 transport to the catalyst surface [84].

There are several other examples of GLAD nanostructured thin films used as catalyst supports, primarily with metallic materials. Khudhayer *et al.* measured the electrocatalytic properties of GLAD Pt nanorods [86]. Unsurprisingly, the nanostructured catalyst exhibited high electrochemical surface

area (surface area enhancement factors can be calculated from the article to be in the range of 5–20), but have relatively poor Pt usage as indicated by the catalyst's mass activity. The same research group later used Cr nanorods as Pt supports, demonstrating comparable electrochemical surface area with 1/4 of the amount of Pt [87]. Interestingly, the activity normalized for Pt mass was not markedly different for the Cr-supported catalysts. High aspect ratio GLAD supports of different materials have also been fabricated and tested by Bonakdarpour *et al.* (Pt/Ti) [88], Francis *et al.* (Pt/Ni) [89], and Gasda *et al.* (Pt/CrN) [90]. Each of these cases have demonstrated surface area improvements relative to traditional particle supports, but still have limited performance – primarily attributed to the Pt morphology. Further studies and development of Pt coating techniques for nanostructured supports should lead to high performance nanopillar catalyst supports.

The concepts of metal oxide support materials and controlled high aspect ratio morphologies will be coupled for the study of nanopillar Nb-O and Nb-TiO_2 catalyst supports in Chapters 2–4. In contrast to metallic supports, phase and composition control is highly important for metal oxide supports, and many factors contribute to overall performance, as will be seen.

1.6 Transparent Electrodes

The combined functionality of optical transparency and electronic conductivity has enabled a range of technologies which are widely available today. Transparent conductors, which are typically thin layers, make optoelectronic devices such as heated windows, displays, light-emitting diodes (LEDs), organic light-emitting diodes (OLEDs), photovoltaics, organic photovoltaics, and transparent thin film transistors (TTFTs) possible [91,92].

Transparent conducting layers are used in applications where electrical current flow and light transmission are simultaneous requirements, often

desirable in orthogonal directions. As is implied by their name, the two most important properties for transparent conducting materials are optical transparency and electrical conductivity, where the balance of these two properties is application dependent. Generally, high optical transmittance (T_{vis}) is sought after for wavelengths in the visible range, with values of $>$80% considered good [91]. Transmission depends on the complex refractive index of the material and is impacted by neighbouring layers and the layer thickness. Electrical conductivity is typically measured in terms of material resistivity (ρ) and sheet resistance (R_s). While resistivity can indicate the quality of the material itself, sheet resistance is thickness-dependent and most often used as the conductivity metric for a transparent conducting layer. Sheet resistance values are considered good when below 100 $\Omega/\square$ and exceptional below 10 $\Omega/\square$, which are most often obtained with layers on the order of $\sim$100 nm with $\rho < 10^{-3}$ Ω cm [91].

Several figures of merit have been suggested in the literature for comparing transparent conductors. In this work, we have chosen to use the Haacke figure of merit (ϕ_{TC}), as displayed in Equation 1.1 [93],

$$\phi_{TC} = \frac{T_{vis}^{x}}{R_s} \tag{1.1}$$

where T_{vis} is averaged transmittance over the visible wavelength range (either 400 nm $< \lambda <$ 750 nm or 400 nm $< \lambda <$ 780 nm in this work), R_s is sheet resistance calculated from four-point probe measurements, and $x = 10$, as suggested by Haacke [93]. High quality transparent conductors have a Haacke figure of merit in the range of $1 \times 10^{-3}\ \Omega^{-1} < \phi_{TC} < 50 \times 10^{-3}\ \Omega^{-1}$. While other transparent conductor figures of merit would have also been suitable for comparing the materials developed in this work, the Haacke's factor was used for its simplicity, applicability to available measurement equipment, and historical significance.

1.6.1 Transparent Conducting Materials

Until recently, transparent conductors were exclusively thin layers of either metals or conducting metal oxide materials. Newer work has shown nanoscale materials, such as carbon nanotubes or metal nanowire networks to have significant potential as transparent conductors [94]. For metallic thin films, there is a very small range of thicknesses (< 50 nm) where low sheet resistance is possible and the layer is semi-transparent. For this reason, metal-based transparent conductors are limited to applications where low transmission is acceptable.

Significantly better transparent conducting properties have been demonstrated for wide-bandgap semiconducting metal oxides, which are extensively reviewed by Chopra *et al.* [91] and Granqvist & Hultaker [92], among others. Wide-bandgap ($E_g \gtrsim 3$ eV) semiconductors offer a large window of transparency across wavelengths, where the transmission at small wavelengths is limited by the onset of interband absorption. The high resistivity of these materials is countered by substitutional doping, typically with metal atoms that can donate an electron (for *n*-type transparent conducting material). Carrier concentrations in the range of 10^{19} – 10^{20} cm^{-3} can be reached through doping to significantly enhance the conductivity while still maintaining the plasma wavelength edge of the transparency window at high visible wavelengths. The combination of high carrier mobility and carefully balanced carrier concentration is crucial for high quality transparent conductors.

Originally observed for thin CdO layers [95], transparent conducting material development has heavily focused on doped In_2O_3, SnO_2, and ZnO thin films [91,92,96]. Specifically, Sn-In_2O_3 (ITO) has dominated commercial applications due to its well established high transparency ($T_{\text{vis}} \gtrsim 85\%$) and conductivity ($R_s \lesssim 10\,\Omega/\square$). Additionally, these high quality properties can

be achieved for ITO at low deposition temperatures with scalable sputtering processes [97]. The main drawback for ITO is the cost and reported pending scarcity of In [43], which has prompted a resurgence of research on reducing In content through nanostructuring and developing In-free transparent conductors. Regardless of the possibility of In scarcity if usage is massively increased, ITO continues to be widely used and will likely continue to be used for many niche applications as alternatives replace large-scale planar ITO layers.

Some of the most promising In-free transparent conducting oxides are F-SnO_2 (FTO) [98], Sb-SnO_2 (ATO) [99], Al-ZnO (AZO) [100], and Nb-TiO_2 (TNO) [77]. While these materials have not yet been widely adopted in industry, FTO is used in many research grade optoelectronic devices. Furthermore, the performance metrics of AZO and TNO are approaching those of ITO and continued development of routes to manufacturing them should result in increased availability of In-free transparent conductors in the future.

In addition to materials development, process integration is important for transparent conducting layers. Transparent conductor thin films are often used without patterning, as substrates for device fabrication; however, the availability and development of processing for patterning, and more recently nanostructuring, of transparent conducting layers is becoming more crucial for manufacturability.

1.6.2 Nanostructured Transparent Conductors

The combination of transparent conductive materials with high aspect ratio nanostructures offers a unique opportunity to alter the interaction of both light and charge with a device's transparent electrode layer. Nanostructures have been used to enhance the capture or extraction of light as well as the

capture or injection of charge carriers. This makes a high aspect ratio nanoelectrodes highly appealing for devices which require simultaneous optical and electrical processes, such as light-emitting [11], photovoltaic [101], photochemical [16], or spectroelectrochemical [102] devices.

In the case of the photochemical and spectroelectrochemical devices, high surface area is desirable to maximize the adsorption of surface species for electrochemical reactions. While optical transparency is only a material requirement for certain configurations of photochemical water-splitting devices, high aspect ratio nanowire arrays of metal oxides (e.g., TiO_2, ZnO, WO_3, Fe_2O_3) have been often chosen in this application [16]. The high surface area and electronic properties can be tuned for the photochemical reaction. Researchers have also demonstrated hierarchical branched nanowire structures as an integrated water-spitting system [17], where the ability to tailor properties and architecture of wide-bandgap metal oxide nanowires lends a path to improve performance. For the spectroelectrochemistry experiments, protein reaction kinetics were gleaned from simultaneous optical probing and electrochemical cycling of proteins adsorbed on a surface. Porous ITO nanopillar films enabled these studies due to their combined high surface area, and transparent conducting properties [102–104].

Possibly the largest use of nanostructured transparent electrodes has been in the field of organic optoelectronics, specifically for hybrid and organic photovoltaic devices. As outlined in Section 1.3.1, photon absorption and charge collection are two very important parts of the photovoltaic conversion process where efficiency can be lost. Many researchers have suggested and attempted the concept of decoupling light absorption and charge extraction through the use of a nanostructured electrode, as shown schematically in Figure 1.6. In this configuration, the transparent electrode is an array of high aspect ratio structures embedded into the photoactive

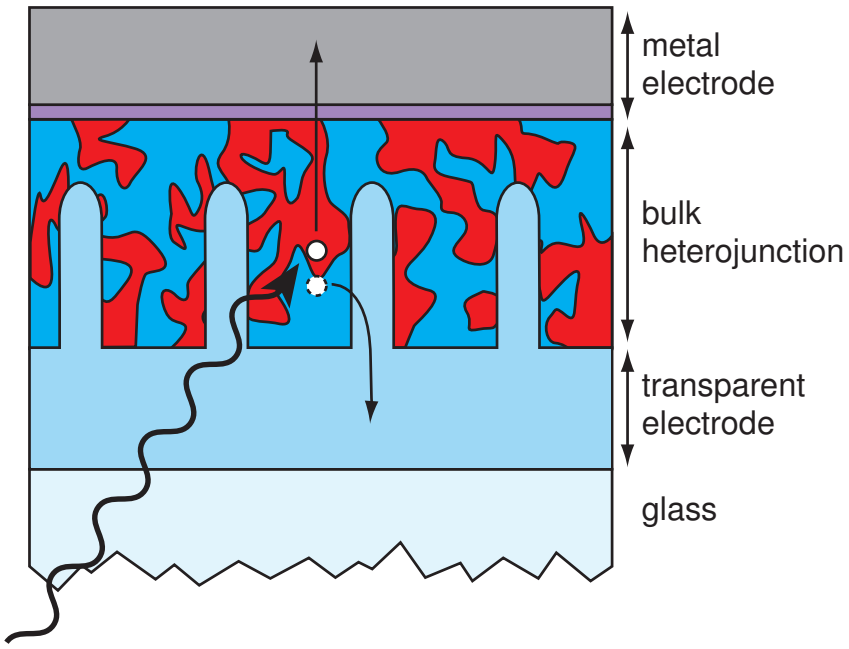

Figure 1.6. *Schematic representation of an organic photovoltaic device with high surface area nanostructured transparent electrode.*

material and enables a thicker bulk heterojunction and/or reduced distance for one of the charge carriers to travel for collection [105]. As collection is only improved for one of the charge carrier types (the hole for a "forward device" as in Figure 1.6), this architecture should have the largest impact on performance when a mobility imbalance exists between the donor/acceptor materials of a bulk heterojunction.

Nanostructured ITO electrodes have been used for dye-sensitized solar cells (DSSCs) by a number of researchers, seemingly starting with Joanni *et al.* [101, 106–108]. The three-dimensional ITO nanowires (up to 10s of μm in length) coated with TiO_2 showed improvements of up to 1.5×, with maximum efficiencies of $\eta \approx 4\%$ [107]. Efficiency improvement was largely attributed to increased electron transfer from the electrolyte to the 3D elec-

trode resulting in increased short-circuit currents.

For OPV integration, some of the first examples of nanostructured electrodes were published by Yu *et al.* [105] and Rider *et al.* [13]. As with TiO_2 coating in the DSSC device class, charge transfer layers are also highly important in OPV devices, where the hole-transporting poly(3,4-ethylenedioxythiophene)-polystyrene sulfonate (PEDOT:PSS) is often used. Yu *et al.* used spin-casting over ITO nanowires in contrast to the electropolymerization method onto GLAD ITO nanopillars by Rider *et al.*. Both groups report superior short-circuit currents for the nanostructured ITO, leading to enhanced power conversion efficiency (a relative increase of 14% (1 sun) – 38% (5 suns) for Yu and 31% (1 sun) for Rider). While the relative efficiency gains showed positive results, the absolute values were still $\eta < 4\%$, with the authors suggesting potential improvements to be had in processing, photoactive polymer choices, and ITO structure and quality.

During the time of this thesis work, several others have also reported on the benefits of nanostructured ITO as OPV electrodes [109–111]. In cases where efficiency improvements were observed, the combination of enhanced charge collection and superior optical effects (i.e., anti-reflection, transmission, scattering) at the electrode were deemed responsible for the increased short circuit current and fill factor [109]. Some three-dimensional ITO electrodes led to inferior OPV device performance, attributed to poor electrical properties of the ITO nanostructures (increased series resistance) and large probability of leakage current (decreased shunt resistance). For nanostructured transparent electrodes to improve device performance, it has become clear that the transparent conducting material must be of extremely high quality in addition to being well nanostructured.

In addition to efficiency improvement, nanowires have also been used in devices for their mechanical properties. ITO nanowire networks are less

susceptible to degradation caused by flexing than thin solid ITO films. An ensemble of cross-linked nanostructures are able to mechanically withstand a higher degree of bending or stretching while maintaining high conductivity pathways throughout the network [112]. High quality flexible transparent electrodes will enable mechanically bendable and stretchable OPV and display devices.

Nanostructured transparent electrodes can be further improved by using In-free alternative materials or by improving the properties and understanding of ITO nanowire arrays. Chapter 4 will focus on the development of nanostructured TNO films, aimed at the eventual application of a three-dimensional transparent electrode. In Chapter 5, techniques to improve ITO nanowire array growth will be studied, allowing for improved morphology and property control of ITO nanoelectrodes.

1.7 Thesis Outline

This thesis focuses on materials development for nanostructured catalyst supports and transparent conducting layers, rather than on the application of the materials in a device. The work in each of Chapters 2–6 has been previously published in some form as indicated at the beginning of each chapter.

The Nb-O system, which is of interest for PEMFC catalyst supports, is introduced in Chapter 2. Nanostructuring of Nb-O and combined crystalline phase formation and morphology control are studied across a range of nanopillar thin film structures. The effects of surface area and reducing anneal atmosphere on phase formation are revealed. The phase formation results from Chapter 2 are then exploited in Chapter 3, where nanostructured Nb-O thin films of different crystalline phases are tested as Pt catalyst supports. Both morphology and phase of the support affect the performance of the

overall catalyst structure.

The Nb-TiO_2 material system acts as the link between Nb-O and ITO materials, it is of interest as both a catalyst support and transparent conductor. Chapter 4 explores composition control on the properties of electron beam-deposited Nb-TiO_2, working toward GLAD nanostructured Nb-TiO_2 films.

Nanostructuring of transparent conductors is further studied in Chapter 5 with the introduction of the VLS-GLAD growth technique for branched ITO nanowires. The range of morphology control for branched ITO nanowire arrays through VLS-GLAD is shown in addition to the transparent conducting properties. Following, one of the unique features of VLS-GLAD is modeled and explained in Chapter 6 where diameter oscillations can be well controlled in the branches of VLS-GLAD ITO nanowires.

Finally, an overview and concluding remarks on the work are provided in Chapter 7.

2

Phase Formation in Nanostructured Niobium Oxides

A version of this chapter has been published:

R.T. Tucker, M.D. Fleischauer, R.M. Shewchuk, A.E. Schoeller, and M.J. Brett, "Phase formation and morphology control of niobium oxide nanopillars," Materials Science and Engineering: B **176**, *626–632 (2011) [25].*

2.1 Introduction

The combination of functional properties and nanoscale morphology is critical for nanotechnology-enabled devices. As the starting point in this thesis, phase formation in nanostructured metal oxides is explored as a route toward controlling the material properties and morphology. Metal oxides are becoming increasingly relevant for application in sensing, energy storage, and energy conversion devices [113]. These materials can exhibit a combination of desirable qualities including variable optical properties, tunable electrical conductivity, corrosion resistance, and temperature and chemical stability [67]. Advances in nanoscale processing have allowed for development of metal oxide nanowires, which offer great potential for enhancing

surface area, confinement, and charge transport properties of metal oxide-based devices [114,115]. While amorphous metal oxides have been used in semiconductor applications, the best electronic performance is observed for metal oxide films with a high degree of crystallinity. Development of controlled phase and morphology metal oxide nanostructures will have direct application to improvements in the electronics, sensing, and energy fields.

Various stoichiometric phases of the niobium-oxygen system (including NbO, NbO_2 and Nb_2O_5) have been used as electronic, optical, and catalytic materials [116]. Tetragonal NbO_2 has been wrongly identified as having relatively low electrical resistivity (6.7×10^{-2} Ω cm [74]) when the accepted value is on the order of 10^4 Ω cm [117]; however, NbO_2 is still believed to have high chemical stability [75]. Specific applications of niobium oxide films include oxygen reduction catalysts [74], electrochromic films [118], chemical sensors [119–121], blocking layers in solar cells [122], electron field emitters [123], and pollution abatement catalysts [124]. The large surface area to volume ratio of high aspect ratio nanostructures is expected to greatly improve metal oxide performance, specifically in sensing and catalysis applications. To date, minimal work has been carried out on the controlled nanostructuring of niobium oxides [125], and study of phase formation and phase transformation is even less explored.

One method used to fabricate high aspect ratio nanostructures is glancing angle deposition (GLAD), a bottom-up technique which exploits the extremes of the structure-zone model to fabricate structured thin films [18–20]. As described in Section 1.2.1, this physical vapour deposition method is based on self-shadowing of incident material when the vapour flux is at significantly large oblique angles to substrate normal. Glancing angles and complex substrate motion have been combined to fabricate thin films structured with arrays of vertical posts, zig-zags, and helices. One strength of

GLAD lies in the physical nature of the structuring, such that the technique can be applied to nearly any vacuum-compatible deposited material [20].

Formation of distinct phases in nanostructured metal oxides is essential for full exploitation of optical and electronic properties in device applications. Metal oxide films structured by GLAD are generally amorphous as deposited, and can be promoted to polycrystalline phases through high temperature processing [126, 127]. To date, most investigations have focused on adding oxygen, generally to return the film to the same stoichiometry as the source material. Annealing under specific gaseous environments (e.g., oxidizing or reducing) can extend the number of phases available at a certain annealing temperature. Under extreme conditions with additional gases present, phase transformation (e.g., from metal oxide to metal nitride) can be accomplished [128, 129].

This chapter explores phase formation and morphology change in nanopillar niobium oxide films fabricated by GLAD. As-deposited amorphous Nb-O films (deposited from Nb_2O_5) were annealed at high temperature in a reducing environment with various flow rates. The resulting phase and morphology of annealed films is explored for its dependence on both initial film structure and annealing conditions.

2.2 Experimental Methods

2.2.1 Thin Film Deposition

Nanopillar niobium oxide films were fabricated on *p*-type Si (100) substrates (University Wafer) via glancing angle deposition in a high vacuum chamber. A description of the GLAD process is given in Section 1.2.1 and Figure 1.2, where the deposition angle α is the angle between vapour flux and substrate normal and rotation in φ is about the substrate normal.

Niobium oxide source material (Nb_2O_5 pieces, 99.95 %, Alfa Aesar) was evaporated by electron beam to provide uniform vapour flux across the substrate area. The deposition flux rate was maintained at (10.0 ± 0.5) Å/s for all depositions, measured via a quartz crystal monitor (QCM) located near the substrate. Substrate motion for vertical post film structure was controlled by software with real-time film thickness feedback to achieve one rotation in φ every 10 nm of film growth while the deposition angle α was held constant.

2.2.2 High Temperature Annealing

Post-deposition processing of films involved high temperature annealing in a controlled reducing atmosphere. Films were annealed in a quartz tube (1 inch outer diameter) inside a temperature controlled Lindberg Blue tube furnace. The furnace was calibrated with several metal melting points (e.g., Cu, Ge) in the temperature range of interest. The annealing routine consisted of (i) 20 minute dwell to allow the annealing gas to purge the tube, (ii) temperature ramp to 1025 °C at 10 °C/min, (iii) dwell at 1025 °C for 1 hour, (iv) passive cooling to room temperature with the gas still flowing. Hydrogen forming gas (5% H_2/balance N_2, $<$ 5 ppm H_2O, Praxair) was allowed to flow through the tube with flow rate controlled by rotameter to adjust the strength of the reducing atmosphere. The rotameter was calibrated against a Lab-crest Flowrator kit; however, certainty of the forming gas flow rate was limited to 5% of the rotameter maximum, equivalent to 20 sccm for the 400 sccm rotameter. Changes in flow rate, furnace geometry, or system leaks had significant effects on the properties of annealed nanopillar films, as noted in initial calibration experiments prior to the results presented here.

2.2.3 Characterization

Film morphology of the prepared samples was observed via scanning electron microscopy (SEM, JEOL 6301F). Samples were coated with Cr to reduce charging effects before imaging in secondary electron imaging mode. Crystalline phase identification was performed using X-ray diffraction (XRD) on a Bruker D8 diffractometer with a Cu K_α source and area detector. XRD patterns were then compared to the powder diffraction file (PDF) database for known phase peak locations. X-ray photoelectron spectroscopy (XPS) was performed with a Kratos Axis 165 spectrometer to verify presence of elemental species. Relative concentrations of atomic species were obtained after sputtering away the film until readings were constant ($\sim$30 nm).

2.3 Results & Discussion

2.3.1 Niobium Oxide Thin Films

Solid thin films of Nb-O were deposited at near-normal incidence ($\alpha = 30°$). A cross-section view of an as-deposited film and representative XRD pattern are shown in Figure 2.1(a) and Figure 2.2, respectively. The film morphology is typical of dense planar films, with slight columnar structure present and the XRD pattern shows the as-deposited film to be amorphous, with no diffraction peaks present.

High temperature treatment in reactive gas environments can induce phase and composition changes in thin films. For oxygen-containing materials, annealing in the presence of H_2 reduces the O_2 content in the film while annealing in the presence of O_2 can increase the O_2 content in the film. The planar Nb-O films were annealed at high temperature in flowing 5% H_2 (balance N_2). Plan view SEM images of films deposited at $\alpha = 30°$ after annealing at 1025 °C with various 5% H_2/N_2 flow rates (100, 200, and

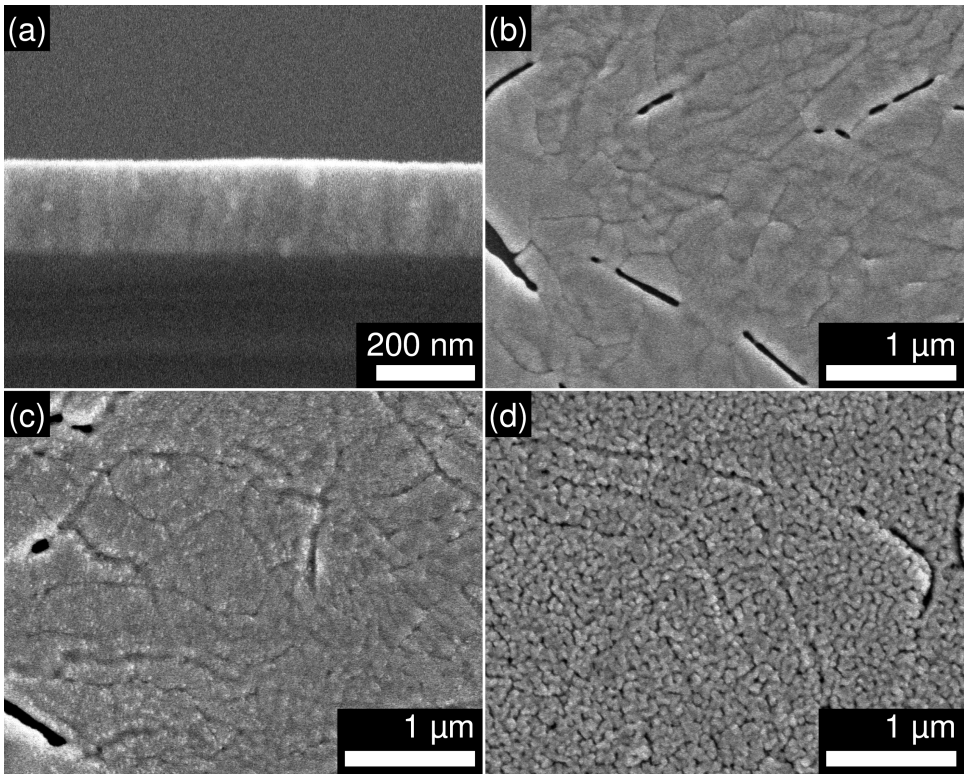

Figure 2.1. *Scanning electron microscopy images of planar niobium oxide films deposited at α = 30°, (a) cross-sectional view as-deposited, and plan view images after annealing at 1025 °C with (b) 100 sccm, (c) 200 sccm, and (d) 400 sccm 5% H_2/N_2.*

400 sccm) are shown in Figure 2.1(b)-(d). The films show stress-related cracking after annealing due to shrinking in volume with oxygen removal. The most reducing annealing condition (400 sccm 5% H_2/N_2, Figure 2.1(d)) shows development of columnar pores normal to the film, suggesting preferential removal of oxygen effectively etching at the morphological grain boundaries in the film.

XRD patterns of the annealed planar Nb-O films from Figure 2.1 are shown in Figure 2.2. After annealing, the planar Nb-O films are polycrystalline, with films annealed in less reducing environment ($\leq$ 200 sccm 5%

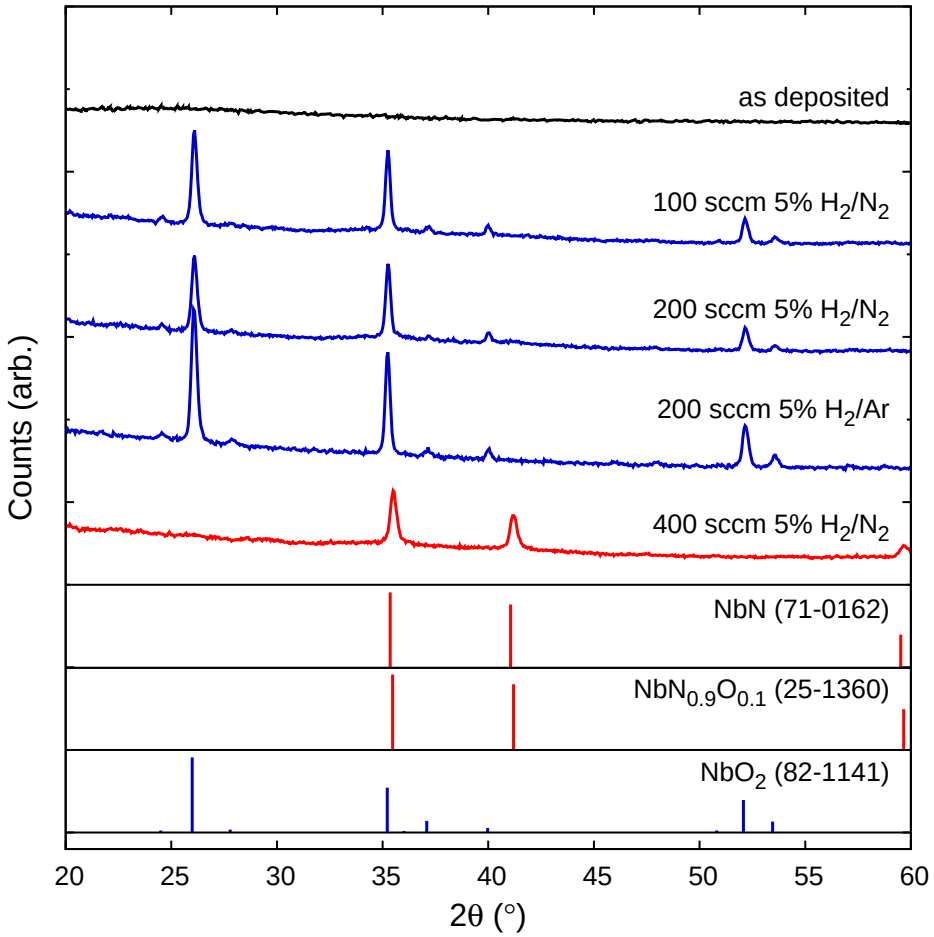

Figure 2.2. *X-ray diffraction patterns of planar niobium oxide films deposited at α = 30°, including a film prior to annealing (as deposited) and films after annealing at 1025 °C under either 200 sccm 5% H_2/Ar or 100–400 sccm 5% H_2/N_2. Reference NbO_2, $NbN_{0.9}O_{0.1}$, and NbN patterns (PDF 82-1141, 25-1360, and 71-0162, respectively) are included. Data from [25].*

H_2/N_2 or H_2/Ar) crystallizing into the NbO_2 phase. At flow rates in the $\leq$ 200 sccm range, both the N_2 and Ar-balanced forming gases have a similar effect on the film reduction (see Chapter 3 for 5% H_2/Ar annealing results). However, at higher flow rates, the N_2-based forming gas affects reaction of the N species with the film, leading to the formation of Nb-O-N compounds. Annealing under 400 sccm 5% H_2/N_2 leads to formation of a NbN_xO_{1-x} ($x = 0.9$ or $x = 1$) phase. The formation of oxynitride phases was at first unexpected, but is justified in the following section. Within the explored range of flow rates ($\leq$ 400 sccm), increasing the forming gas flow rate results in an increasingly reducing atmosphere for the anneal.

2.3.2 Nanopillar Niobium Oxide Thin Films

Motivated by the prospect of high surface area conductive niobium oxide catalyst supports, phase formation in porous Nb-O nanopillar films was investigated. Nanopillar niobium oxide films were grown at various deposition angles ranging from $\alpha = 30^\circ$ to $\alpha = 87^\circ$. Nanopillar niobium oxide films of 500 nm nominal thickness grown at deposition angles $\alpha = 70^\circ$, 80°, 84°, and 87° are shown in Figure 2.3; higher deposition angles resulted in both increased porosity and increased feature diameter.

The films deposited from Nb_2O_5 were shown to be amorphous by XRD, with patterns similar to Figure 2.2. After annealing the films were found to be polycrystalline. Notable changes to the nanopillar morphology are shown in Figure 2.4. For more porous nanopillar films, the post-annealed structures are a significant departure from the as-deposited films shown in Figure 2.3. Nanopillar GLAD films exhibit wilting (collapse) and clumping after annealing; however, the overall porosity is still correlated with initial deposition angle. Comparison of a film deposited at $\alpha = 70^\circ$ before and after annealing (Figure 2.3(a) to Figure 2.4(a)) reveals larger feature diameter and

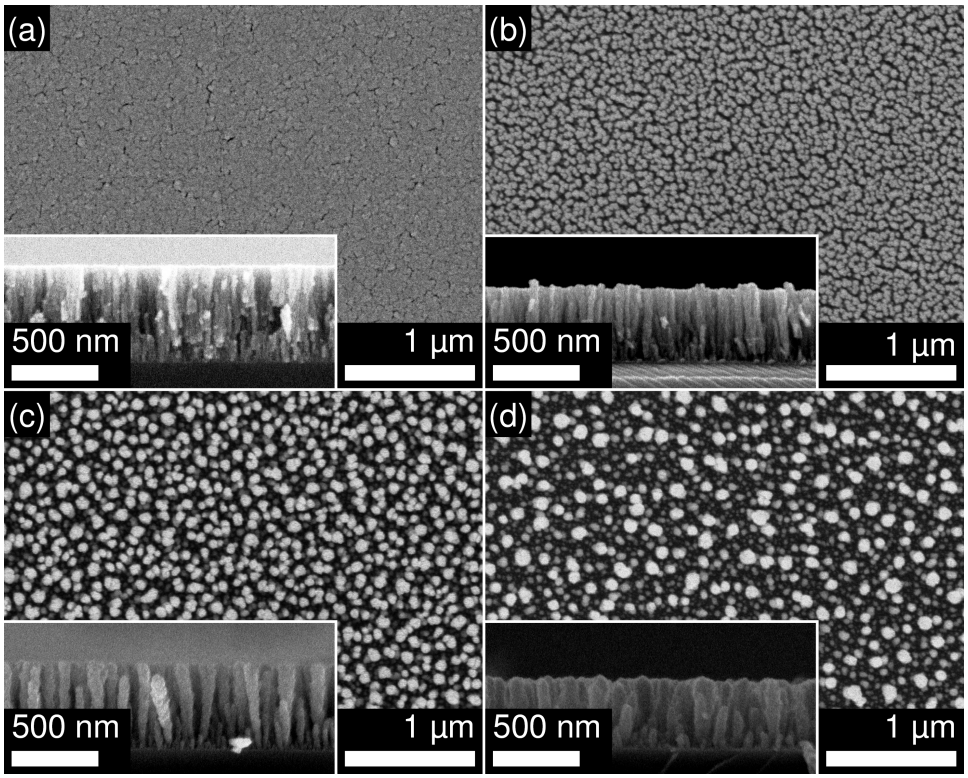

Figure 2.3. *Plan view scanning electron microscopy images of nanopillar niobium oxide films before annealing (cross-sectional images inset) deposited at (a) α = 70°, (b) α = 80°, (c) α = 84°, and (d) α = 87°. Images from [25] copyright © 2011 Elsevier.*

defined pores after annealing. Similar changes are noted for Figure 2.4(b)-(d), with additional wilting present for increasingly separated features.

The phase formation observed was largely dependent on annealing gas environment. When the films were annealed in either air or N_2 gas, the pillar structures completely coalesced into faceted Nb_2O_5 crystals of ∼500 nm diameter. Alternatively, annealing in hydrogen-containing environments, such as forming gas, enabled access to lower oxygen content phases such as NbO_2 or further reduced phases. Figure 2.5 displays XRD patterns of the different porosity niobium oxide nanopillar films from Figure 2.4 along with peak positions for NbO_2, $NbN_{0.9}O_{0.1}$, and NbN. Past a certain point of

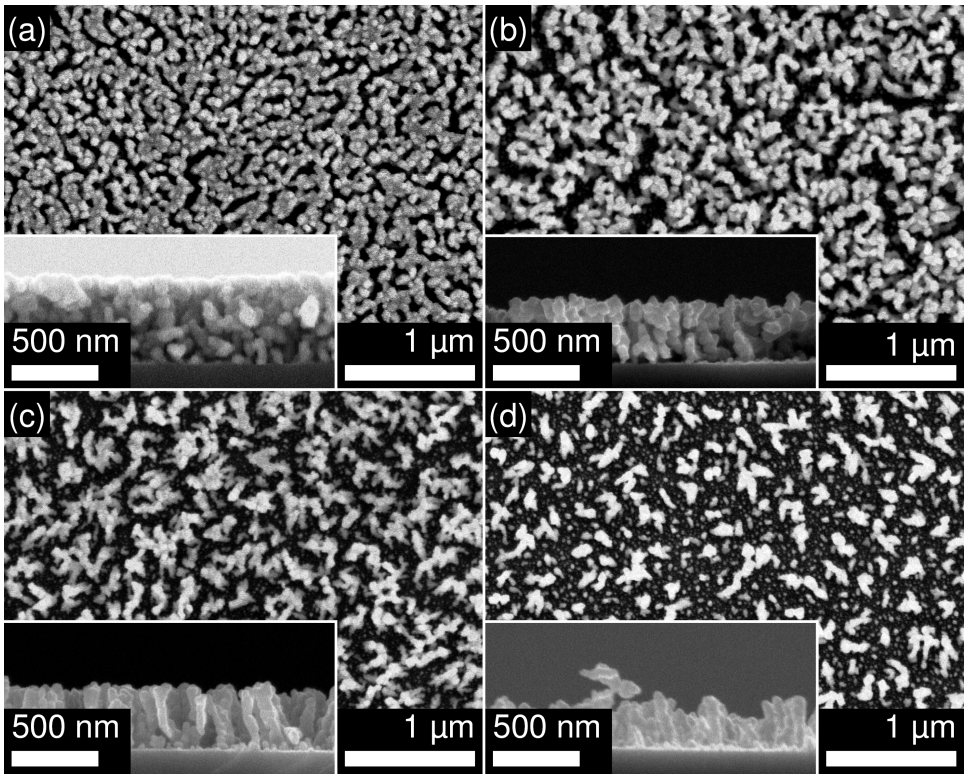

Figure 2.4. *Plan view scanning electron microscopy images of nanopillar niobium oxide films (cross-sectional images inset) after annealing at 1025 °C with 200 sccm 5% H_2/N_2 flow. Films deposited at (a) α = 70°, (b) α = 80°, (c) α = 84°, and (d) α = 87°. Images from [25] copyright © 2011 Elsevier.*

oxygen reduction, the films absorb nitrogen from the 5 % H_2/N_2 forming gas (nitrogen is used as a carrier gas for safety reasons). A cubic niobium oxynitride (NbN_xO_{1-x}) phase [130] was present in both mixtures with NbO_2, and on its own at high forming gas flow rates. The films matching this NbN_xO_{1-x} phase cannot be clearly distinguished between $NbN_{0.9}O_{0.1}$ or NbN through our XRD.

XPS was used to verify the elemental content during this phase transformation. XPS spectra of annealed Nb-O films are shown in Figure 2.6, with sample atomic concentrations calculated for each of these phases and shown in Table 2.1. The films were observed to have substantial nitrogen content

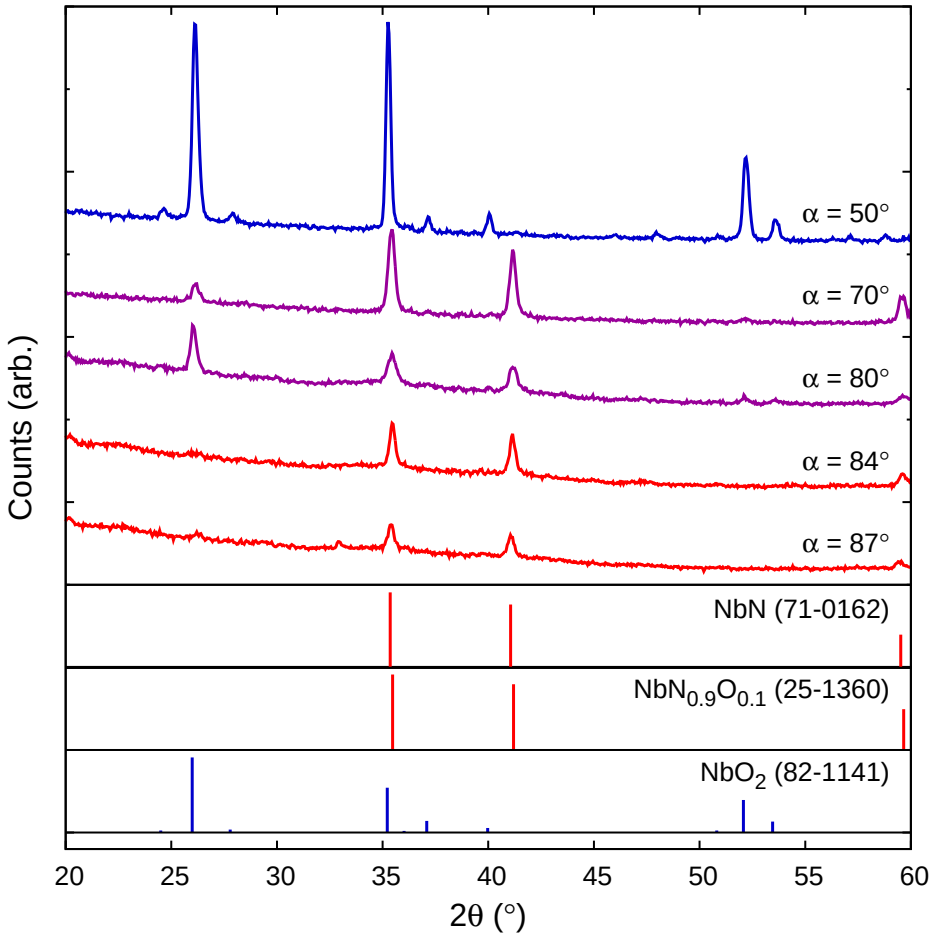

Figure 2.5. *X-ray diffraction patterns of nanopillar niobium oxide films deposited at different deposition angles α after annealing at 1025 °C with 200 sccm 5% H_2/N_2 flow. Reference NbO_2, $NbN_{0.9}O_{0.1}$, and NbN patterns (PDF 82-1141, 25-1360, and 71-0162, respectively) are included. Data from [25].*

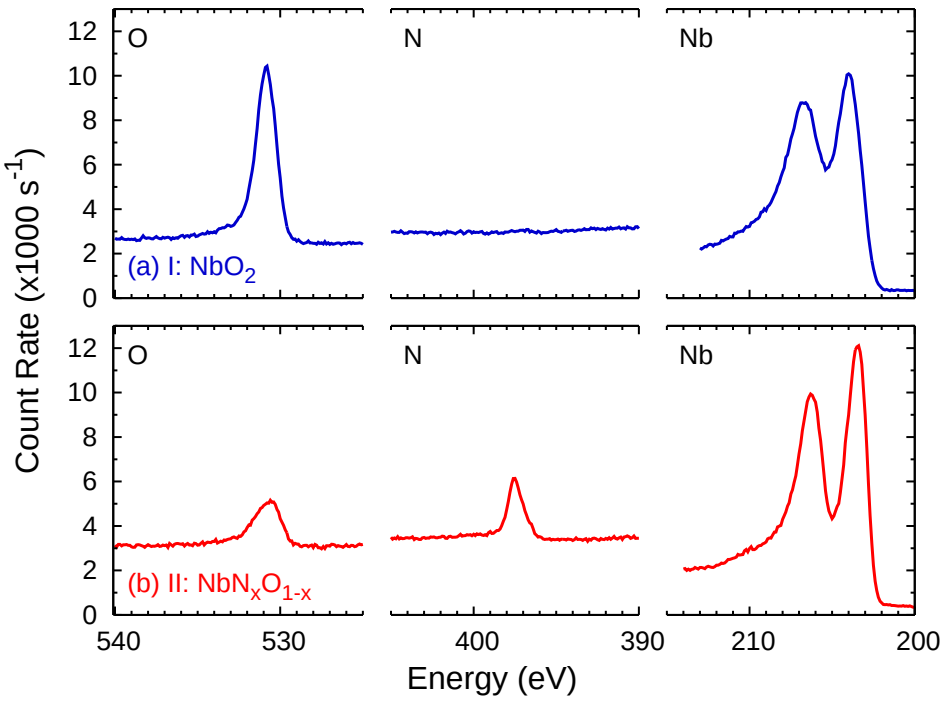

Figure 2.6. *X-ray photoelectron spectra of O, N, and Nb peaks from niobium oxide films annealed at 1025 °C, resulting in either (a) phase I: NbO_2 or (b) phase II: NbN_xO_{1-x}.*

when the crystalline phase matched the NbN_xO_{1-x} pattern and virtually zero nitrogen content for films matching the NbO_2 phase, confirming the formation of nitrides in highly reduced films. Transformation from Nb_2O_5 to NbN has been reported for heated nanoparticles in precursor gases with accessible nitrogen [129]. A similar mechanism for nitrogen substitution is presented here where we suggest that the Nb-O catalyzes N_2 decomposition, and the cubic nitride phases are more energetically favorable when sufficient oxygen has been removed. Our hypothesis that some oxygen may remain after these annealing processes was confirmed by XPS, suggesting the NbN_xO_{1-x} phase to be mostly $NbN_{0.9}O_{0.1}$.

The general trend apparent in Figure 2.5 is that films deposited at higher

Table 2.1. *Phase designations for niobium oxide nanopillar films after annealing and sample atomic concentration of Nb, O, and N from X-ray photoelectron spectroscopy data.*

	Phase	Structure	at.% Nb	at.% O	at.% N
I	NbO_2	tetragonal	46.3	52.9	0.8
II	NbN_xO_{1-x}	cubic	50.3	20.8	29.0

deposition angles form further reduced phases under the same reducing conditions. A dense film ($\alpha = 30^\circ$ or 50°) has reduced to NbO_2 (I) and very sparse films ($\alpha = 84^\circ$ or 87°) have reduced to NbN_xO_{1-x} (II). Films of intermediate porosity ($\alpha = 70^\circ$ or 80°) consist of a mixture of NbO_2 and NbN_xO_{1-x} (I+II); the XRD patterns for $\alpha = 70^\circ$ and 80° in Figure 2.5 clearly contains peaks of both NbO_2 and NbN_xO_{1-x} phases. A similar trend was observed for the other forming gas flow rates at which experiments were conducted, including 50, 100, and 400 sccm.

We suggest that films deposited at higher deposition angles are more suitable for diffusion and reaction of the forming gas due to the increased porosity and feature spacing. Our results indicate that the susceptibility to reduction of these films is correlated to both surface area and volume. The more porous films have less material volume for the same nominal thickness, further contributing to more rapid reduction.

Increased forming gas flow rate was observed to significantly suppress coalescence of features, and thus reduce morphology degradation, as shown in Figure 2.7. A niobium oxide film deposited at $\alpha = 80^\circ$ is shown after annealing at various forming gas flow rates (50, 100, 200, 400 sccm). While coalescence is prevalent in a weaker reducing environment/lower flow rate (50 sccm, Figure 2.7(a)), the thin vertical post structures are left more intact after annealing in a stronger reducing environment/higher flow rate (400 sccm, Figure 2.7(d)). This trend is consistent for forming gas flow rates between

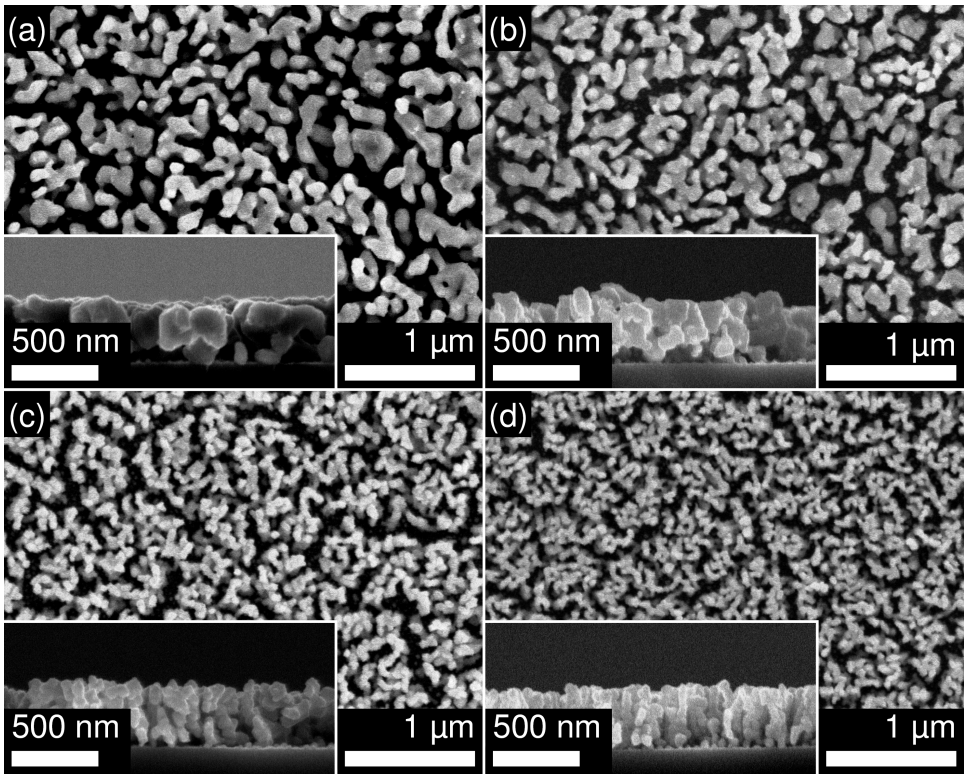

Figure 2.7. *Plan view scanning electron microscopy images of a nanopillar niobium oxide film ($\alpha = 80°$, cross-sectional images inset) after annealing at 1025 °C with 5% H_2/N_2 flow rates of (a) 50 sccm, (b) 100 sccm, (c) 200 sccm, and (d) 400 sccm. Images from [25] copyright © 2011 Elsevier.*

these two extremes (100 sccm, Figure 2.7(b) and 200 sccm, Figure 2.7(c)).

XRD patterns for the GLAD film ($\alpha = 80°$) annealed at various forming gas flow rates (shown in Figure 2.7) are displayed in Figure 2.8 along with peak positions for NbO_2, $NbN_{0.9}O_{0.1}$, and NbN. Higher forming gas flow rates lead to further oxygen reduction in final film phases. For this $\alpha = 80°$ GLAD film, a 50 sccm forming gas flow rate resulted in NbO_2 phase formation (I) and 400 sccm forming gas flow rate resulted in NbN_xO_{1-x} phase formation (II). Intermediate forming gas flow rates (100 and 200 sccm) result in mixtures of NbN_xO_{1-x} and NbO_2 (I+II).

Properties, including molar weight, mass density, and melting point for

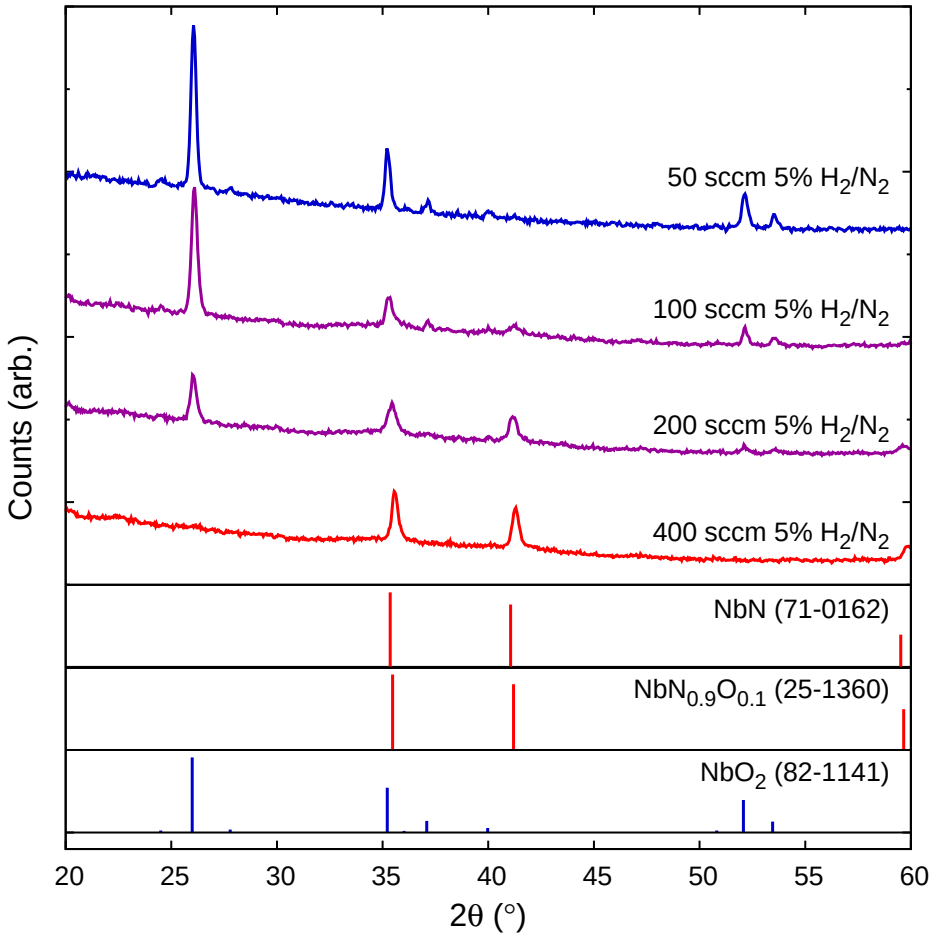

Figure 2.8. *X-ray diffraction patterns of a nanopillar niobium oxide film (α = 80°) after annealing at 1025 °C with 5% H_2/N_2 flow rates of 50–400 sccm. Reference NbO_2, $NbN_{0.9}O_{0.1}$, and NbN patterns (PDF 82-1141, 25-1360, and 71-0162, respectively) are included. Data from [25].*

Table 2.2. *Properties of select niobium oxide, oxynitride, and nitride phases along with calculated volume containing 1 mol Nb atoms*[a].

	Weight (g/mol)	Density (g/cm^3)	Melting Point (°C)	Volume (cm^3/mol Nb)
Nb_2O_5	265.81	4.47	1500	29.7
NbO_2	124.91	5.90	1901	21.2
$NbN_{0.9}O_{0.1}$	107.11	8.28[b]	-	12.9
NbN	106.91	8.47	2300	12.6

[a] All values from [131] unless noted.
[b] Values from [132].

Nb_2O_5, NbO_2, $NbN_{0.9}O_{0.1}$, and NbN are given in Table 2.2 [131, 132]. Assuming the niobium content in the film is constant and only oxygen and nitrogen content are altered through the processing, the volume of relevant compounds normalized to 1 mol Nb was calculated. The volume is reduced from 29.7 cm^3/mol Nb to 12.6 cm^3/mol Nb if the film is completely reduced from as-deposited Nb_2O_5 to NbN. Greater than half of the volume can be lost through this phase transformation process, likely contributing to the morphology change differences observed for different phases. Another contributing factor is the melting temperature of the newly formed phases. In the case of the phases explored here, the melting points of the post-annealed films are greater for increasingly reduced phases, increasing from 1500 °C for Nb_2O_5 to 2300 °C for NbN in Table 2.2. We suggest that higher melting temperature in reduced films is responsible for the observed structural preservation of nanopillars during annealing in high forming gas flow rates.

To summarize the relationship between film porosity and reducing environment, a partial, qualitative phase map is constructed in relation to the fabrication parameters of deposition angle α and forming gas flow rate. The phase map is shown in Figure 2.9 for deposition angles $\alpha = 30°$, 50°, 70°, 80°, 84°, 87° and flow rates 50, 100, 200, 400 sccm annealed for 1 h at 1025 °C.

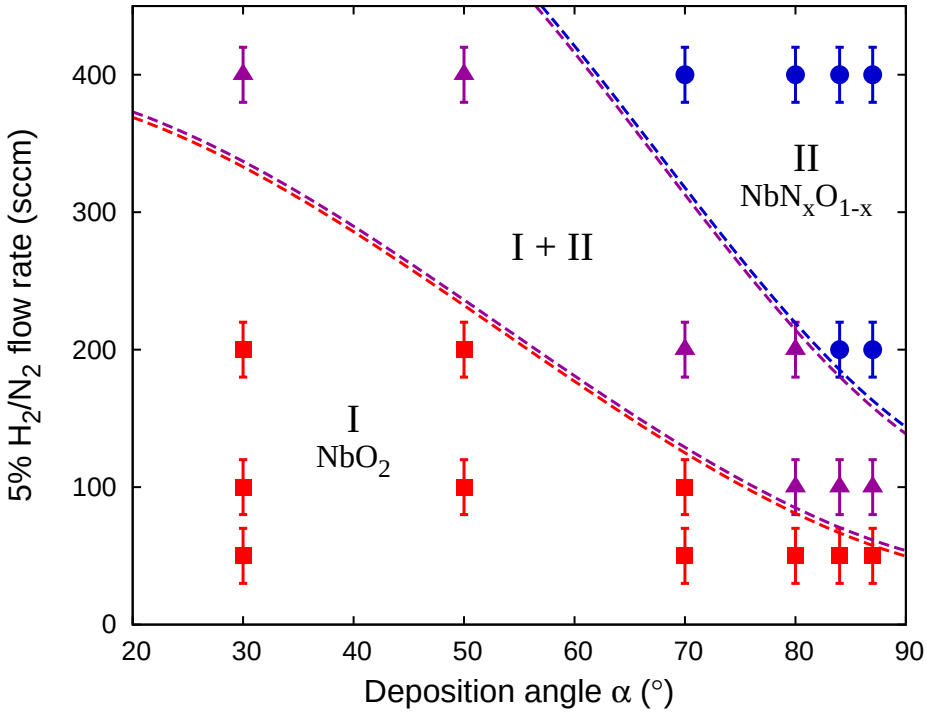

Figure 2.9. *Summary of phase formation for nanopillar niobium oxide films annealed at 1025 °C according to 5% H_2/N_2 flow rate and deposition angle. Crystalline phases determined to be I: NbO_2, II: NbN_xO_{1-x}, or a mixture I+II from X-ray diffraction patterns. Error bars represent uncertainty in flow control rotameter and contours are drawn to aid in the visualization of possible phase regions. Data from [25].*

The XRD patterns for each film at each annealing condition were carefully analyzed and determined to be primarily comprised of either of two crystalline phases, or a mixture thereof. As first shown in Table 2.1, phase region I matches with NbO_2 XRD pattern and has virtually zero nitrogen content. Phase II is a cubic niobium oxynitride phase with XRD patterns matching to cubic NbN_xO_{1-x} phases with similar composition and lattice constant (i.e., $NbN_{0.9}O_{0.1}$, NbN). In cases where there was evidence of multiple phases, a mixture of phases I + II was designated. These phase designations were

then plotted according to deposition angle and forming gas flow rate, with uncertainty indicated, to aid in the visualization of the trends described above. Qualitative contours are also included as possible phase boundaries. Both higher forming gas flow rates and more porous GLAD films lead to increased oxygen removal. The phase map acts as a guide for achieving the appropriate Nb-O or Nb-N phase for a particular application. A multidimensional phase diagram including variations in annealing time and temperature, along with studies of impact on pore size distribution, would allow for fabrication of films of given phase and porosity/morphology as required for a variety of catalyst applications.

The relationship between morphology and phase formation has been investigated for the niobium-oxygen-nitrogen system. The susceptibility to phase transformation due to porosity is expected to be present in other metal oxide systems. The exact mechanisms for phase transformation, and specific phases that may be formed, will most certainly vary with material system and cannot be projected here.

2.4 Conclusion

Through studies of annealed niobium oxide nanopillar films, we have developed a parameter-based phase map to demonstrate unique phase formation trends in porous nanostructured films. Distinct polycrystalline phases of tetragonal NbO_2, cubic NbN_xO_{1-x}, and mixtures thereof, were observed after annealing in a reducing environment. A strong link was shown between morphology and phase formation in structured thin films after annealing, such that both initial porosity and forming gas flow rate affect resultant morphology and crystallinity. More porous films are more readily reduced to low oxygen content phases, and phase transformation to niobium nitride is induced in extreme cases. Higher forming gas flow rates deter coalescence

of features, preserving surface area and offering a degree of morphology control attributed to increase in melting point through phase transformation. It is hoped that the ability to form niobium oxide and nitride films of desirable crystalline phase with limited physical deterioration to nanostructured features will increase use of functional nanopillar films in related applications.

The study of phase formation in niobium oxide nanopillars explored in this chapter was motivated by the requirement of distinct phase nanopillar arrays for electrocatalyst supports. We demonstrated annealing in 5% H_2/N_2 for the formation of NbO_2 and NbN_xO_{1-x} phases, and annealing in 5% H_2/Ar for the formation of Nb_2O_5 and NbO_2 phases. In Chapter 3, this understanding will be used for the fabrication of nanopillars of Nb_2O_5, NbO_2, and NbO crystalline phases. The electrochemical properties of Pt-coated niobium oxide nanopillars of these various phases will be shown and demonstrate the importance of crystalline phase for electrocatalytic performance.

3

Nanostructured Niobium Oxide Catalyst Supports

A version of this chapter has been published:

A. Bonakdarpour, R.T. Tucker, M.D. Fleischauer, N.A. Beckers, M.J. Brett, and D.P. Wilkinson, "Nanopillar niobium oxides as support structures for oxygen reduction electrocatalysts," Electrochimica Acta **85**, *492–500 (2012) [133].*

3.1 Introduction

The previous chapter focused on the development of nanopillar Nb-O films of different phases for the application as fuel cell catalyst supports. Proton exchange membrane fuel cells (PEMFC) are reviewed in detail in Section 1.4 and have potential as efficient and clean power sources for portable, stationary and transportation applications [58,66]. However, there are several barriers that prevent their wide spread commercialization including cost and durability of components like membranes and catalysts [59,64]. One of the main contributors to the overall cost of PEMFCs originates from high Pt loadings required to overcome the kinetic activation losses in the cathodic electroreduction of oxygen to water [59,60]. The most commonly employed

electrocatalyst at present consists of 2–4 nm Pt nanoparticles dispersed on high surface area carbon blacks such as XC-72 or BP-2000 [60]. Significant research in the past few years has revealed that carbon corrosion, which occurs in the presence of Pt catalysts and an elevated electrochemical potential, is one of the main failure modes of the widely used Pt/C electrocatalyst [69, 134–136]. For these reasons, there is a significant amount of current research on alternative catalyst supports [68, 70]. Ideal catalyst support materials should exhibit chemical and electrochemical stability under the acidic conditions, electrochemical potential, and operating temperature range of fuel cells. They should also possess adequate electrical conductivity, high surface areas, and allow for facile production and integration in electrode structures.

A review of catalyst support materials and nanostructured fuel cell catalyst supports is given in Sections 1.5.1–1.5.2. For the purposes of this chapter, high aspect ratio catalyst support structures have been developed (notably the nanostructured thin film (NSTF) supports by 3M [15]) and have shown high stability and specific activity for Pt and non-Pt catalysts. New nanostructured support materials, such as carbon nanotubes [137] and conductive metal oxides [67, 68, 73] have been suggested to overcome the electrical conductivity, high temperature processing, and water management challenges of the NSTF support. The challenge is to structure the metal oxides with a high surface area morphology and accessible pores as outlined in Section 1.5.2, however, fabrication of specific compositions and phases of nanopillar structures is complex and limited methods have been shown to be viable for prototype fabrication.

The glancing angle deposition (GLAD) process enables the fabrication of nanostructured thin films from a wide range of materials, including organics, metals, and metal oxides [18, 19]. Taschuk *et al.* provide a review of the

GLAD technique, and common applications such as optical coatings and high speed sensors [20]. Briefly, GLAD depends on a combination of highly oblique vapour incidence angles, self-shadowing, limited adatom mobility, and finely controlled substrate motion to nanostructure films of a variety of useful morphologies – the technique is introduced in more detail in Section 1.2.1. High surface area nanopillar catalysts and supports fabricated via GLAD have been demonstrated for many materials including Ti [88], C [84], CrN [90], and Pt [86].

In the previous chapter, it was shown that GLAD-deposited amorphous Nb-O can be transformed into nanostructured NbO_2, Nb-O, or Nb-O-N through controlled-atmosphere high temperature annealing [25]. Here, we report on the electrochemical activity of Pt-coated GLAD nanostructured Nb_2O_5, NbO_2, and NbO + NbO_2 catalysts, with an emphasis on how the interplay between crystalline phase and nanostructured morphology affects the electrocatalytic performance. Further electrochemical characterization of the catalysts for the oxygen reduction reaction in acidic media is reported in Reference [133].

3.2 Experimental Methods

3.2.1 Thin film deposition

Niobium oxide catalyst supports were grown by GLAD on mirror-polished 5 mm diameter glassy carbon disks (Tokai) and *p*-type Si (100) substrates (University Wafer). Nb_2O_5 pieces (99.95%, Alfa Aesar) were used as received and evaporated by an electron beam in a custom deposition chamber (Kurt J. Lesker Company). Nb_2O_5 was evaporated at a rate of 1 nm/s for a total nanopillar thickness of 500 nm. The deposition angle α was fixed at 84° between the incident flux and substrate normal. Substrates were rotated

about their normal (rotated in φ) at a rate of one rotation per 10 nm of film growth to achieve a vertical nanopillar morphology.

Films were annealed in a temperature-controlled 1 inch diameter tube furnace (Lindberg Blue M) to achieve appropriate phase formation. The annealing program consisted of (i) a 20 min annealing gas purge at 25 °C, (ii) a temperature ramp to 1000 °C at a rate of 10 °C/min, (iii) a 1 h dwell at 1000 °C, and (iv) passive cooling to below 90 °C with flowing annealing gas. The annealing gas was either Ar (99.998%, Praxair) or hydrogen forming gas (5% H_2/balance Ar, Praxair). The flow of the annealing gas was controlled via mass flow controller units (MKS Instruments). After annealing, magnetron sputtering was used to deposit 0.1 mg/cm^2 of Pt on the nanopillar supports. The Ar process gas pressure was maintained at 7 mTorr throughout the sputtering process. Pt was deposited at a rate of 4 nm/min using a magnetron power density of 1.6 W/cm^2.

3.2.2 Physical Characterization

X-ray diffraction (XRD) was performed to determine phase and crystallinity of the niobium oxide samples. Scans were collected from films on Si witness substrates using a Bruker D8 diffractometer with a Cu K_α radiation (λ = 0.15418 nm) source and Hystar area detector. Scans collected from films on glassy carbon substrates used the aforementioned system and a Rigaku Ultimate IV diffractometer in thin film (parallel beam) mode. The beam incidence angle was held fixed at 0.5° while the detector was scanned from 20° to 60° scattering angle at a rate of 0.25° or 1.0°/min. Phase identification was performed using the powder diffraction file (PDF) database.

The Scherrer equation was used to estimate the Pt particle size from XRD spectra. The Scherrer equation uses the full-width at half-maximum (β) of diffraction peaks to calculate the limit of the crystalline particle's dimension

($\mathcal{L}$), as shown in Equation 3.1,

$$\mathcal{L} = \frac{K\lambda}{\beta \cos(\theta)}, \tag{3.1}$$

where K is a dimensionless constant (Scherrer suggests K = 0.93), λ is the X-ray radiation wavelength, and θ is half of the scattering angle [138].

Scanning electron microscopy (SEM) images were obtained using a Hitachi S-4800 instrument. Plan view images were taken on both Si and glassy carbon substrates before and after Pt deposition. Cross-sectional view images were only feasible with Si substrates, because they could be cleaved to provide a side view of the GLAD posts.

3.2.3 Electrochemical Characterization

Electroanalytical investigations were performed using a Pine rotating disk electrode (RDE) system, a Pt counter electrode (Radiometer Analytical), a Cl^--free Hg/Hg_2SO_4 reference electrode (Radiometer Analytical), and 0.1 M double distilled $HClO_4$ (GFS Chemicals). The Pine instrumentation consisted of an AFCBP1 bipotentiostat, an AFMSRCE rotator and a change-disk E4TQ RDE electrode. The cell (125 ml three neck, Ace Glass) was saturated with either N_2 or O_2 (both 99.998%, Praxair) by running gas for about 5 min through a porous dispersion tube (Ace Glass). All measurements were performed at ambient temperature (21 $\pm$ 0.5) $^\circ$C and pressure (760 Torr). Electrochemical potentials mentioned here are referenced to the reversible hydrogen electrode (RHE); reported current densities are normalized by either the geometric or electroactive surface area of the electrodes.

Extreme care was taken to ensure the cleanliness of the glassware, cell parts, and samples during handling and setup. Glassy carbon disks were handled in aluminum collars during all steps except for the controlled atmosphere annealing. An ultem jig (DPM Solutions) described in Ref. [81] was

used to facilitate sample transfer.

Samples were first electrochemically cleaned by sweeping their potential between 50 mV and the open circuit potential (OCP), which was approximately 1050 mV, at 500 mV/s until steady state cyclic voltammograms (CV) were obtained. Low scan rate CVs were then acquired in the range of OCP to 50 mV (the onset of H_2 evolution) at 10 and 50 mV/s. CV measurements were then repeated using upper cut-off potentials of 1200 and 1400 mV. Electrochemical stability of the samples was examined using 3000 potential cycles in the range of 50 to 1300 mV at a rate of 500 mV/s.

The electrochemically active surface area (ECSA) of a sample was estimated by integrating charge for the H^+_{des} region of the CVs collected under saturated N_2 conditions and using the common 210 $\mu C/cm^2$ Pt conversion factor [60]. The surface enhancement factor (SEF) was obtained by dividing the ECSA by the geometric surface area SA_{geo} (also called footprint area – 0.16 cm^2 for a 4.5 mm diameter film on a 5 mm diameter disk) as shown in Equation 3.2.

$$\text{SEF} = \frac{\text{ECSA}}{SA_{\text{geo}}} \tag{3.2}$$

While different metrics have been used to compare catalyst performance (e.g., electrochemical surface area, area-specific activity, or mass-specific activity), the SEF factor provides a simple parameter which is easily related to the surface area of the nanostructured support.

3.3 Results & Discussion

3.3.1 Pristine Morphology and Crystallinity

SEM images of the as-deposited films are shown in Figure 3.1. The oblique and cross-sectional images provided as Figure 3.1(a)–(b) display the results

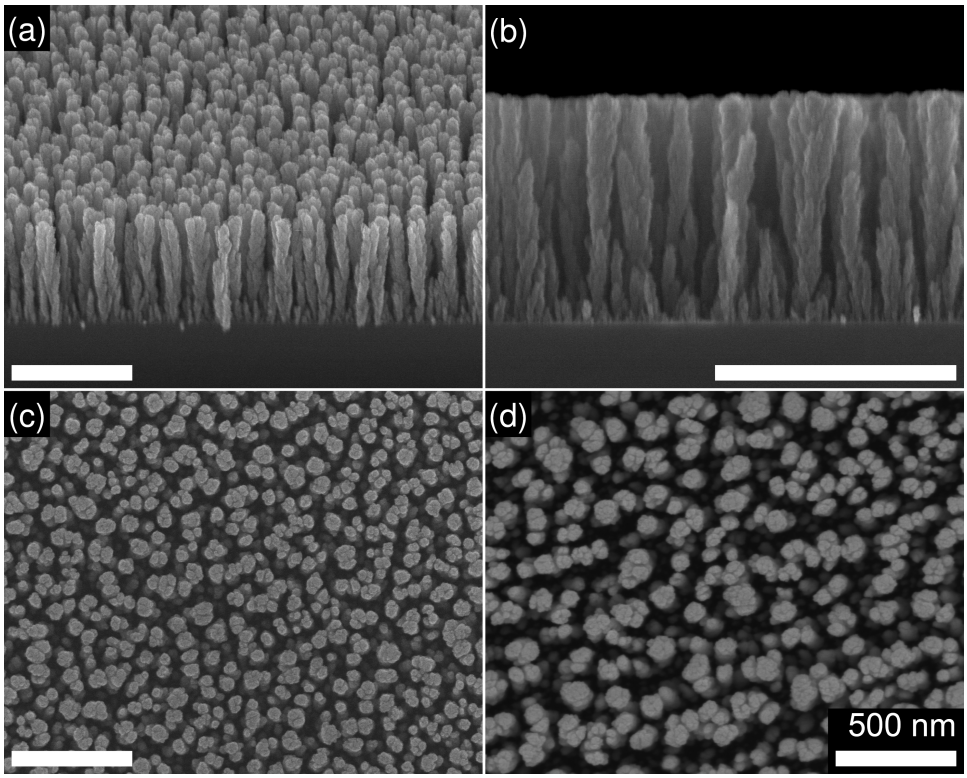

Figure 3.1. *Scanning electron microscopy images of as-deposited nanopillar niobium oxide films at (a) oblique, (b) cross-sectional, and (c), (d) plan views. Films shown in (a)–(c) are grown on a Si wafer and (d) on a polished glassy carbon disk. Images from [133] copyright © 2012 Elsevier.*

of the competitive process that takes place during GLAD growth, with the result that some posts do not extend throughout the entire film thickness. Surface roughness and adatom mobility have an impact on initial nucleation density. Plan view images of Nb-O films show a number density of $\sim$100 μm^{-2} when grown on Si substrates (Figure 3.1(c)) compared to $\sim$60 μm^{-2} when grown on glassy carbon disks (Figure 3.1(d)). The difference is attributed to the slight roughness and surface imperfections on the glassy carbon disk, leading to fewer and larger nucleation points.

The surface roughness of the glassy carbon disk can be reduced by polishing. Figure 3.2 shows Nb-O films deposited on differently polished glassy

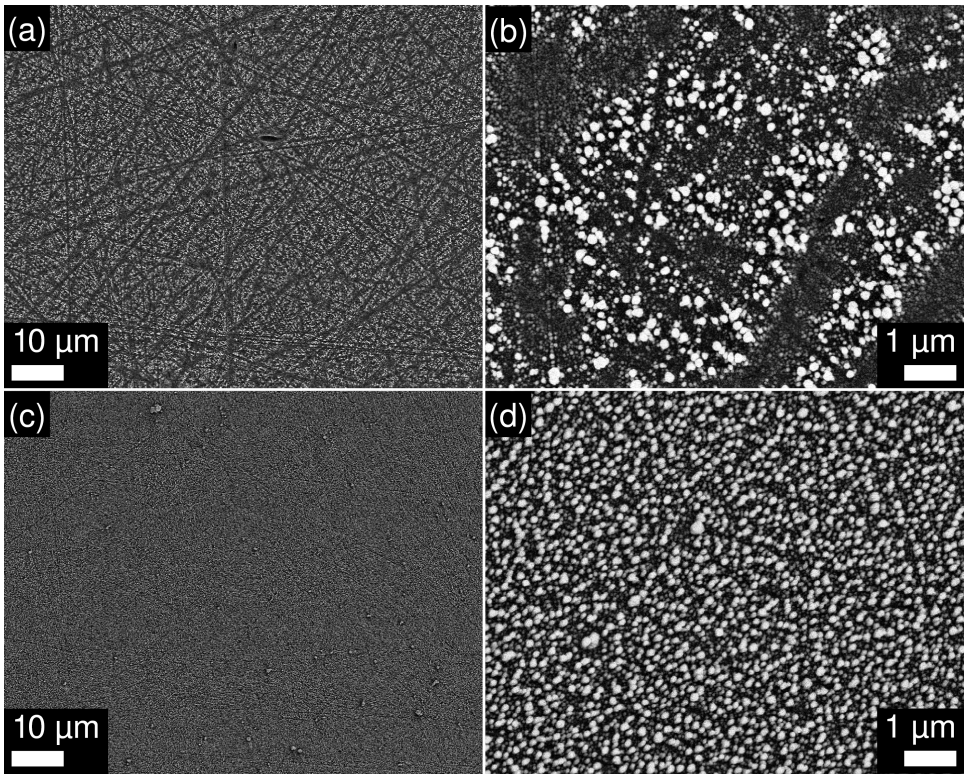

Figure 3.2. *Plan view scanning electron microscopy images of nanopillar niobium oxide films on glassy carbon disks after polishing with (a), (b) coarse polish, and (c), (d) fine polish.*

carbon disks. Coarse polishing of the glassy carbon disk (Figure 3.2(a)–(b)) leaves the surface with sufficient roughness to affect the GLAD nanopillar growth; trench-like markings a clearly induced by the large grain polishing. A subsequent finer polishing step (in the range of 0.05 µm particles) smooths the surface much more, resulting in a significantly more uniform nanopillar film (Figure 3.2(c)–(d).

High temperature annealing induced significant structural changes in the as-deposited films, as described in detail in Chapter 2. SEM images of the annealed films before and after Pt deposition are provided in Figure 3.3. Films annealed in Ar (Set 1, Figures 3.3(a)–(b) underwent the most

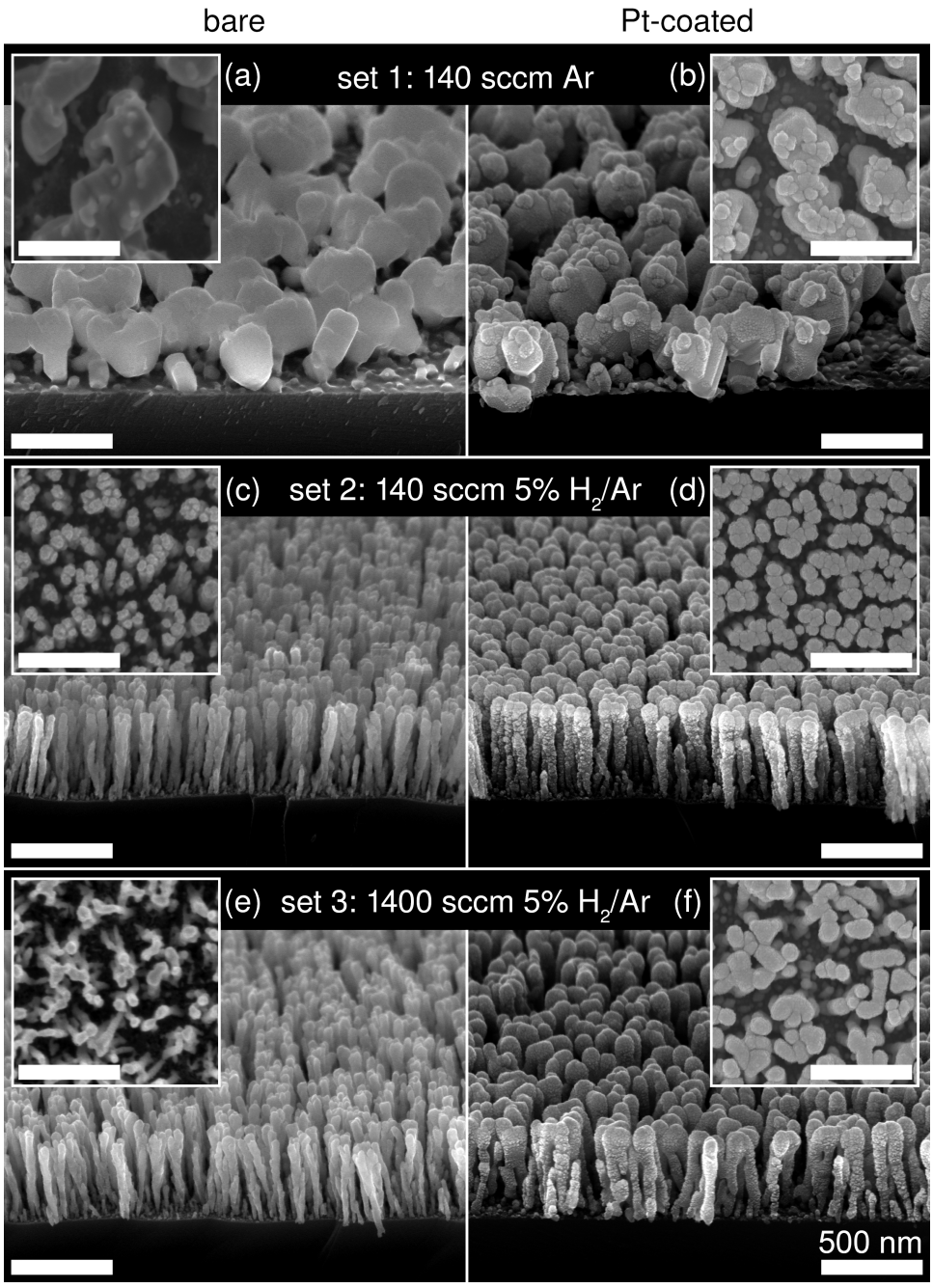

Figure 3.3. *Oblique scanning electron microscopy images of annealed nanopillar niobium oxide films grown on Si wafers (a), (c), (e) before and (b), (d), (f) after Pt sputter deposition (plan view images inset). Annealed in (a)–(b) Set 1: 140 sccm Ar, (c)–(d) Set 2: 140 sccm 5% H_2/Ar, (e)–(f) Set 3: 1400 sccm 5% H_2/Ar. Images from [133] copyright © 2012 Elsevier.*

significant morphology change. The nanopillars coalesced from <100 nm diameter posts into larger (≥200 nm) faceted crystals during this phase change. In an inert annealing environment, there is enough oxygen present to form the energetically favourable Nb_2O_5 phase. The lower melting point of this phase (1500 °C) [131] allows for the significant morphological change and coalescence observed at annealing temperatures of 1000 °C. Films annealed in a 5% H_2/Ar forming gas atmosphere (Set 2, Figures 3.3(c)–(d) and Set 3, Figures 3.3(e)–(f) exhibit significantly better morphology preservation through the annealing process. Annealing in the presence of H_2 reactively removes O from the film, leaving lower O-content films with higher melting temperatures (NbO_2: 1901 °C, NbO: 1937 °C) [131]. The increased forming gas flow rate (Set 3) leads to increased oxygen removal from the film. However, a small amount of wilting and slumping is present, attributed to a change in volume and density after significant oxygen removal. Overall, Set 1 features have significantly larger diameter and lower number density. Sets 2 and 3 have comparable diameter and number density to the as-deposited film, with slightly larger void sizes present in Set 3.

Film morphology affected the Pt distribution. The 0.1 mg/cm^2 Pt loading coated the coalesced crystals fairly uniformly, but tended to cluster near the top of the smaller, more numerous pillars in Sets 2 and 3. Some Pt was also present in smaller clusters along the length of each post (appearing as bright spots). High resolution images of the Pt-coated posts are provided as Figure 3.4. Continuous Pt coverage along the length of some posts to the substrate, and some direct substrate coverage, is visible in Set 1 (Figure 3.4(a)). Pt clustering at the top of the films dominates the images of Sets 2 (Figure 3.4(b)) and 3 (Figure 3.4(c)).

XRD patterns collected from the Pt coated films are provided as Figure 3.5. Prior to annealing, all films were amorphous and showed no diffrac-

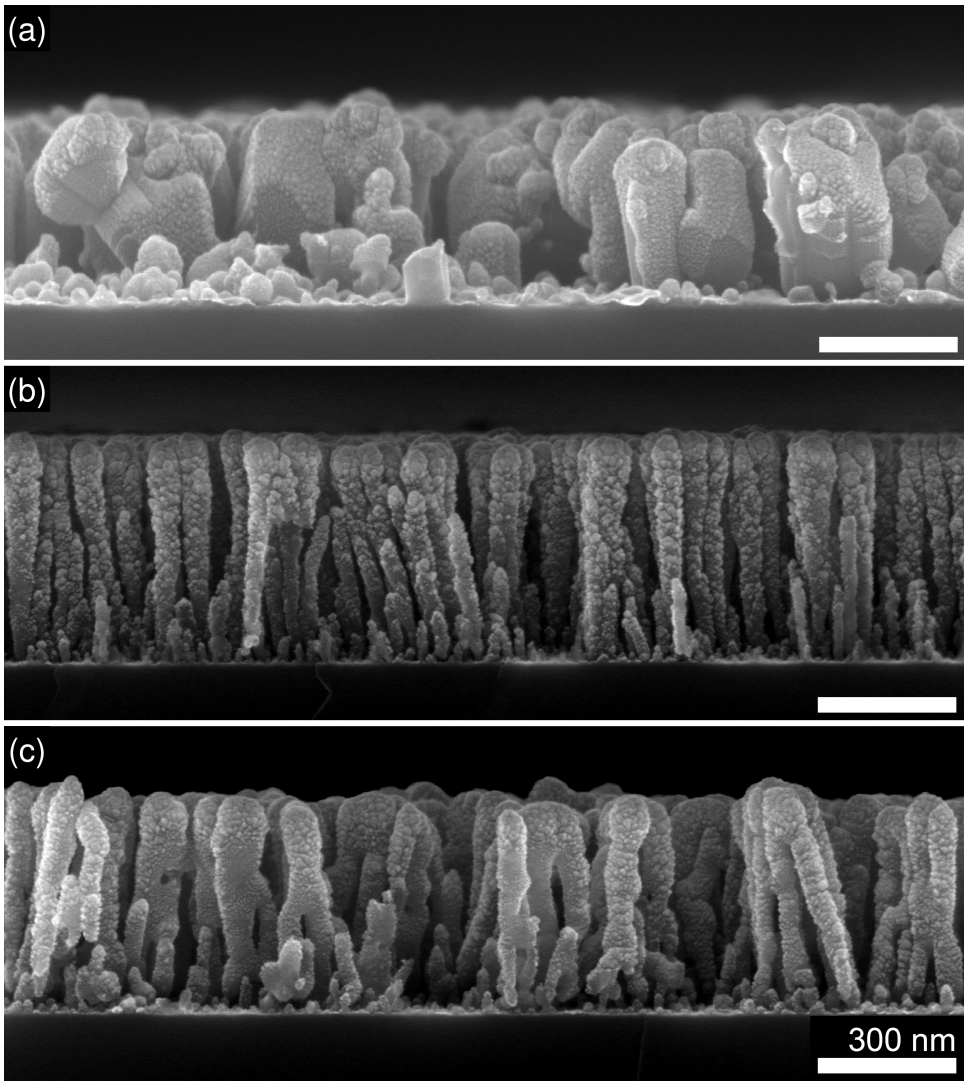

Figure 3.4. *High resolution cross-sectional scanning electron microscopy images of Pt-coated, nanopillar niobium oxide films on Si wafers annealed at 1000 °C in (a) Set 1: 140 sccm Ar, (b) Set 2: 140 sccm 5% H_2/Ar, (c) Set 3: 1400 sccm 5% H_2/Ar. Images from [133] copyright © 2012 Elsevier.*

Table 3.1. *Summary of electrocatalyst sample sets and corresponding crystalline phases identified by X-ray diffraction.*

Set	Anneal gas	Flow rate	Phase
1	Ar	140 sccm	Nb_2O_5
2	5% H_2/Ar	140 sccm	NbO_2
3	5% H_2/Ar	1400 sccm	NbO + NbO_2

tion peaks by XRD, as has been previously shown for planar and nanopillar electron beam deposited Nb-O thin films [25, 125] and discussed in Chapter 2. Films annealed in Ar atmosphere (Set 1, Figures 3.3(a)–(b)) are of Nb_2O_5 phase, as expected. Films annealed under 140 sccm forming gas (Set 2, middle XRD scan in Figure 3.5, shown in Figures 3.3(c)–(d)) have transformed into NbO_2; films annealed under 1400 sccm forming gas (Set 3, lowest scan in Figure 3.5, shown in Figures 3.3(e)–(f)) have been further reduced to a mixture of NbO_2 and NbO. These results are summarized in Table 3.1.

As previously discussed, higher forming gas flow rates result in increasing oxygen removal from the GLAD Nb-O films during annealing (Chapter 2). The XRD pattern for Set 3 includes some evidence of weak $NbSi_2$ peaks. These phases result from annealing the nanopillar niobium oxide films on Si wafers in a highly reducing atmosphere at 1000 °C, and are not present in the samples deposited on glassy carbon disks and used for electrochemical testing. XRD patterns are provided for the Si witness samples instead of the tested glassy carbon samples because of the much lower background intensity associated with the Si substrates, making phase identification much more clear. XRD patterns collected from films on glassy carbon disks before and after electrochemical testing are provided later in this chapter.

Pt grain size, approximated from the Pt (111) XRD peak width using

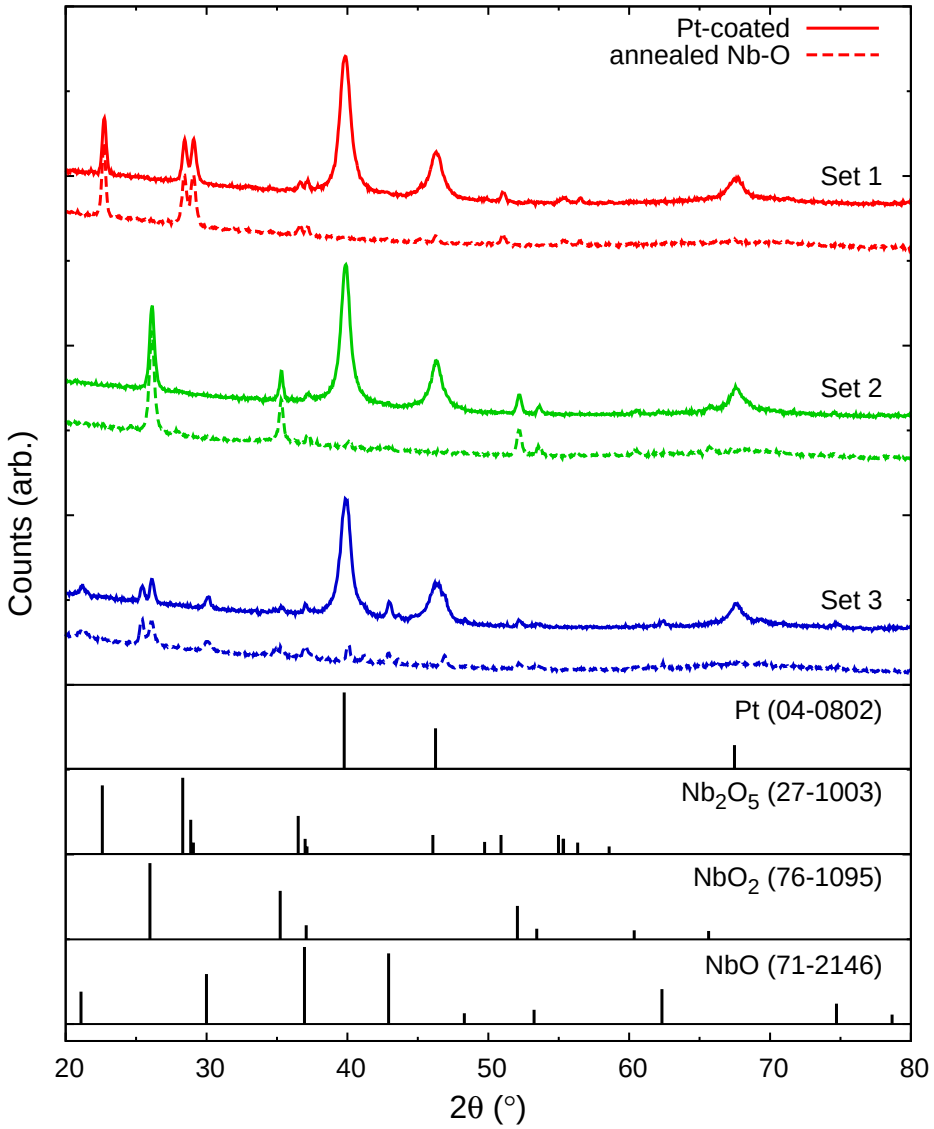

Figure 3.5. *X-ray diffraction patterns collected from Pt-coated, nanopillar niobium oxide films on Si wafers annealed at 1000 °C in Set 1: 140 sccm Ar (red), Set 2: 140 sccm 5% H_2/Ar (green), or Set 3: 1400 sccm 5% H_2/Ar (blue). The colour scheme (Set 1: red, Set 2: green, Set 3: blue) is consistent for all figures in this chapter. Reference Pt, Nb_2O_5, NbO_2, and NbO patterns (PDF 04-0802, 27-1003, 76-1095, and 71-2146, respectively) are included. Data from [133].*

Equation 3.1, is (15 $\pm$ 5) nm for all three sample sets. Pt coating increased the nanopillar width by 30–40 nm, suggesting the coating is approximately one grain thick, on average. It is important to note that the approximated Pt grains are almost an order of magnitude larger than the common 2–4 nm target, and at least double those reported on some 3M NSTF supports [139]. Smaller Pt particles are desirable for their higher surface area, however, better durability is seen with larger particles.

3.3.2 Electrochemical Performance and Stability

Pt distribution and underlying support morphology have a large impact on electrochemical performance. CVs collected from the three sample sets and a planar Pt reference are provided in Figure 3.6. All three Pt-coated Nb-O nanopillar support show higher current density magnitudes (i.e., higher activity) than the reference Pt sample. Fully developed CV features, i.e., those of H_{ads}/H_{des} and OH_{ads}/OH_{des} regions, were only obtained from the Nb-O samples after CV scans were performed to an upper cut off potential of 1200 mV vs. RHE or higher. CVs in Figure 3.6 were collected from samples cycled first to 1050 mV and then 1200 mV vs. RHE. It is interesting to note that all four CV features are most clearly defined for Sets 1 and 3, while Set 2 exhibits poorly defined features indicative of larger ohmic losses (substantially larger than that of the insulating Nb_2O_5 supports in Set 1). The baseline capacitance is lowest for Set 1 and similar for Sets 2 and 3.

The effect of higher upper potential during CV cycling is shown for a sample from Set 1 in Figure 3.7. As previously mentioned, fully developed CV features are present for CVs with an upper cut off potential of at least 1200 mV vs. RHE. Higher upper potential limits did not change the shape of the H_{ads}/H_{des} regions appreciably, although the amplitude of the O_{des} region increases with the upper potential limit up to 1400 mV vs. RHE.

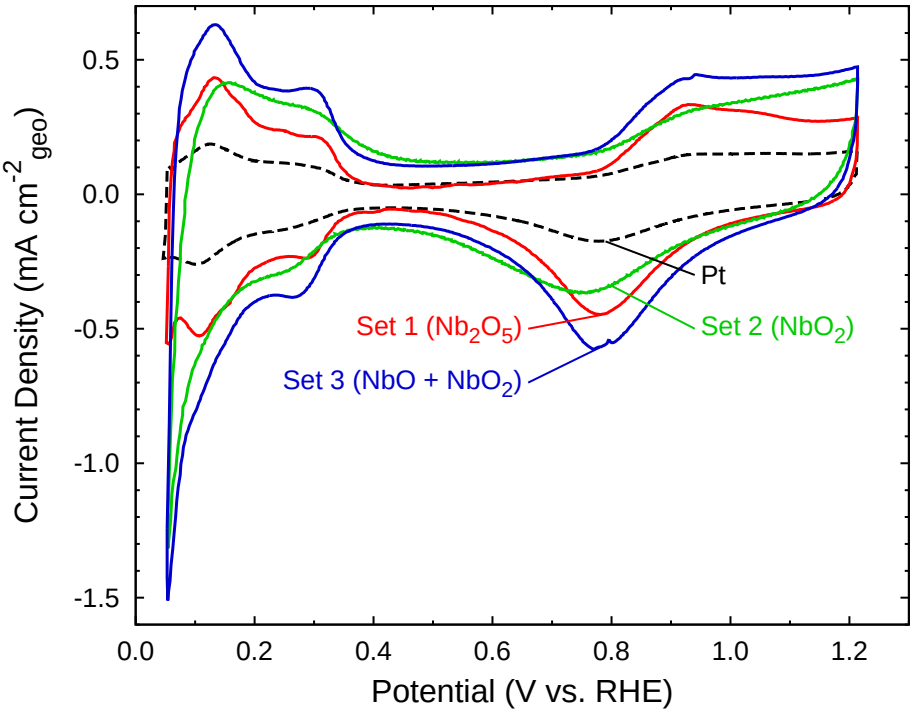

Figure 3.6. *Representative cyclic voltammograms of Pt-coated, annealed nanopillar niobium oxide support structures (Sets 1–3) and reference bulk Pt. All scans collected at 50 mV/s. Data from [133].*

Stability cycling of 3000 cycles at 1400 mV vs. RHE caused only a slight decline in the CV amplitude.

SEFs and whole-system resistances for the three sets (and a Pt reference) are provided in Figure 3.8. The Pt reference is measured to have a value of SEF ≈ 2, attributed to edge effects and inherent surface roughness. At room temperature, Nb_2O_5 is insulating and NbO_2 and NbO have bulk resistivity values of $\sim 10^4$ Ω cm and $\sim 10^{-4}$ Ω cm, respectively [116, 117, 140, 141][1]. Although NbO_2 is a much better conductor than Nb_2O_5, both values are many orders of magnitude more resistive than bulk Pt ($\sim 10^{-7}$ Ω cm), and

[1] A value of 15 S cm^{-1} (6.7×10^{-2} Ω cm) has been attributed to Ref. [141] in Refs. [74,142]. Via private communication with Sasaki, we determined they intended to cite Ref. [143].

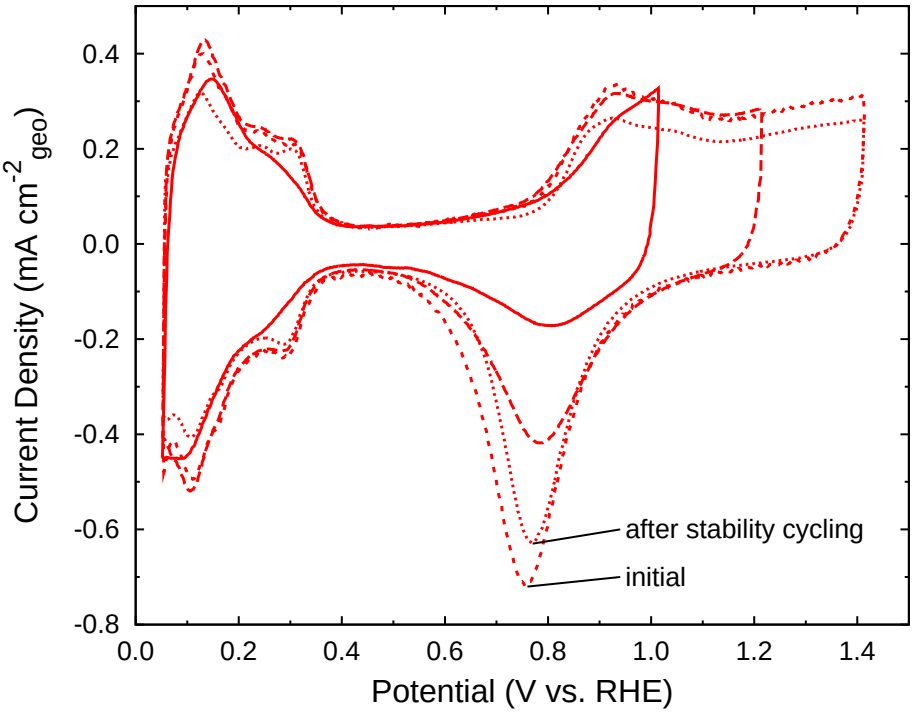

Figure 3.7. *Cyclic voltammograms collected from Pt-coated nanopillar supports (Set 1: Nb_2O_5) to different upper potential limits (1.0, 1.2, and 1.4 V vs. RHE). All scans collected at 50 mV/s and stability cycling consisted of 3000 scans to 1.4 V vs. RHE. Data from [133].*

significant losses can be expected. These results suggest that the Pt coating provides a conductive path around the Nb_2O_5 supports, but not for the NbO_2 or NbO + NbO_2 supports. This suggestion is supported by the side view images of support morphologies shown in Figure 3.4. Set 1 (Nb_2O_5) supports exhibit large spaces between features, with Pt directly contacting the glassy carbon disk. Set 2 (NbO_2) supports show that the majority of the Pt is located on the upper half of the post, with few or no conductive pathways visible through the Pt alone. Set 3 (NbO + NbO_2) supports have Pt located farther down the post resulting from the slightly larger void size.

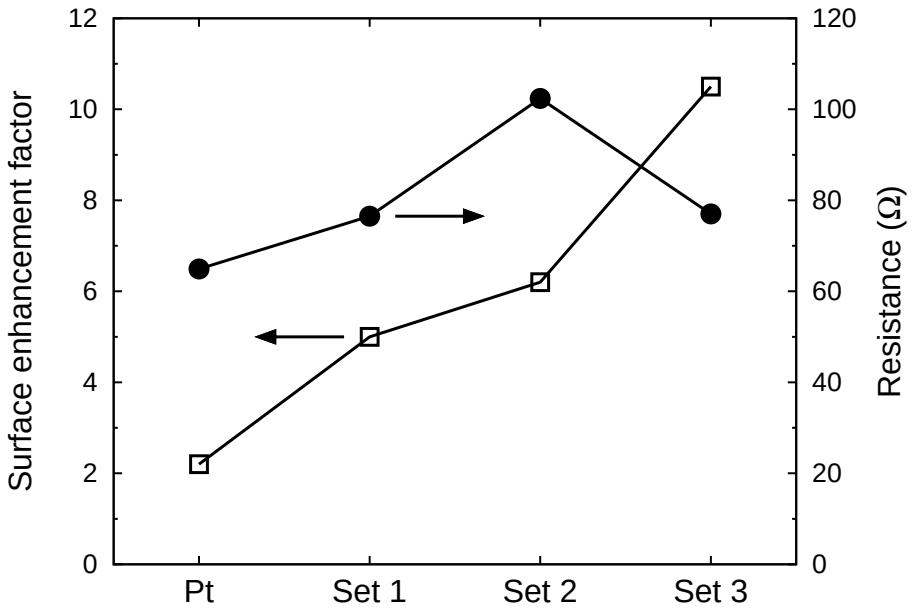

Figure 3.8. *Surface enhancement factor and the cell ohmic resistances of a bulk Pt reference and Pt-coated nanopillar niobium oxide sample sets. Data from [133].*

The combination of superior Pt conduction and higher support conductivity can account for the significant difference in performance between Set 3 and Set 2. Higher surface area primarily accounts for the improved activity of Set 3 compared to Set 1.

XRD patterns collected from glassy carbon disks before and after electrochemical testing are shown in Figure 3.9. No changes in Pt grain size, or the underlying support phase or crystallinity, were detected; however, the Nb-O and Pt peaks were weak compared to the glassy carbon background signal, making analysis difficult. SEM images of the same disks after electrochemical cycling (3000 cycles) (see Figure 3.10) also revealed little morphology change, providing further evidence that these Nb-O supported Pt catalysts show adequate stability to warrant further investigation. Note the

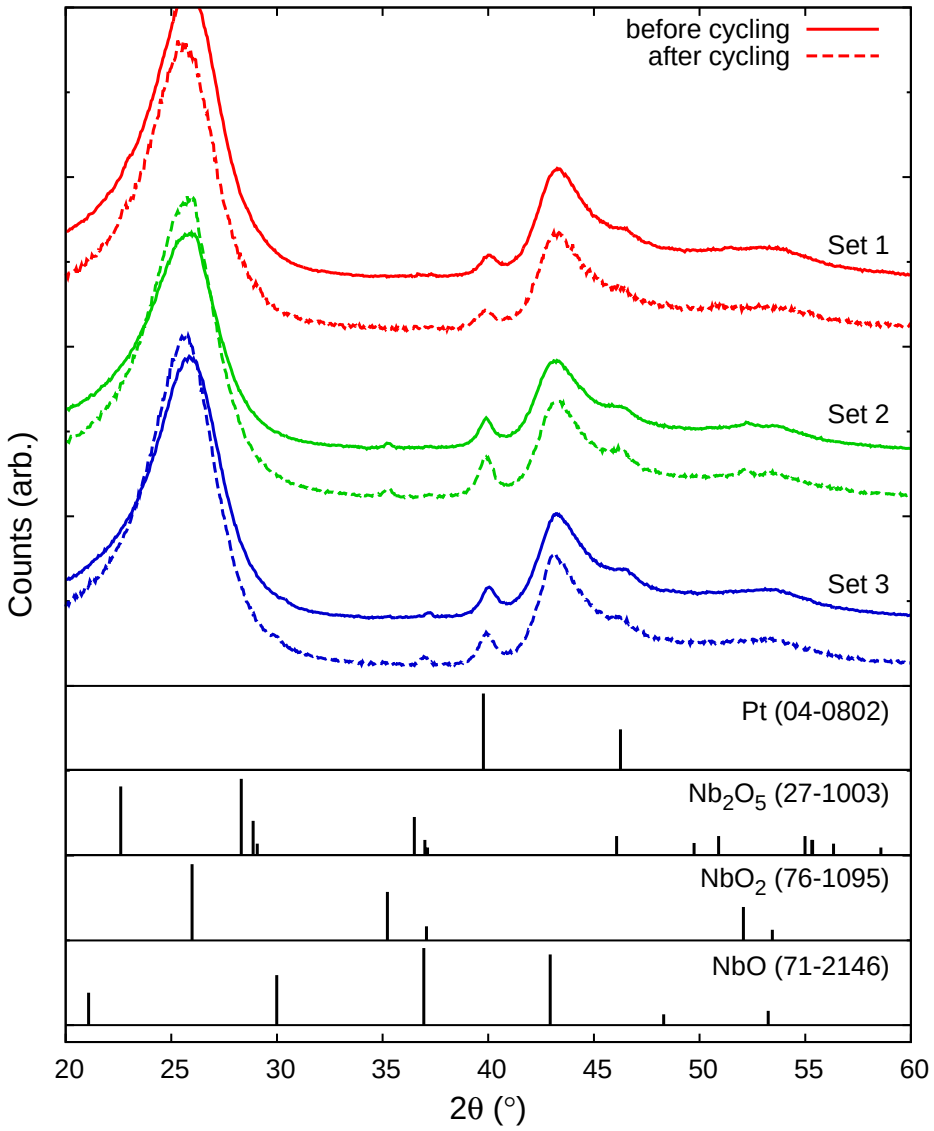

Figure 3.9. *X-ray diffraction patterns collected from Pt-coated, annealed nanopillar niobium oxide supports on glassy carbon disks before and after electrochemical cycling (over 3000 cycles). Reference Pt, Nb_2O_5, NbO_2, and NbO patterns (PDF 04-0802, 27-1003, 76-1095, and 71-2146, respectively) are included. Data from [133].*

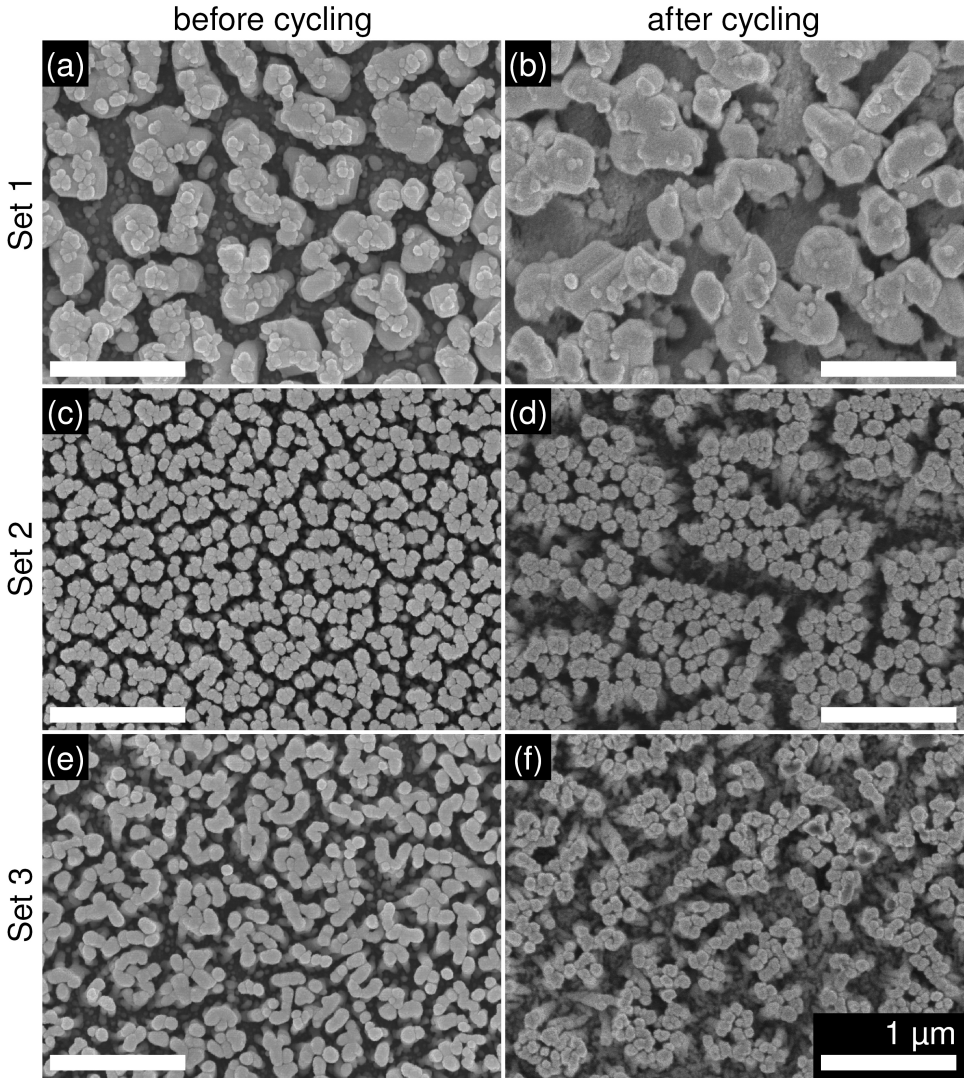

Figure 3.10. *Plan view scanning electron microscopy images of Pt-coated, annealed nanopillar niobium oxide supports on glassy carbon disks (a), (c), (e) before and (b), (d), (f) after electrochemical cycling (over 3000 cycles). Sets 2 and 3 exhibit clumping after testing, often seen in high aspect ratio nanostructures upon drying prior to imaging. Images from [133] copyright © 2012 Elsevier.*

clustering in images from Sets 2 and 3 (Figures 3.10(d) and (f)), likely due to the "nanocarpet" effect [144] which occurs when a high aspect ratio film is immersed in liquid and then allowed to dry in an uncontrolled manner. Similar clumping is observed for most combinations of GLAD materials and liquids, attributed to capillary forces.

The surface area of the NbO_2 supports is insufficient to compensate for the reduced performance relative to the Nb_2O_5 and NbO + NbO_2 supports. It is once again important to consider the nature of the Pt distribution when explaining these results. Pt loading on the Nb_2O_5 supports (Set 1) resulted in a fairly uniform coating, seemingly enough to provide adequate electrical conductivity. The SEF for Set 1 was $\sim$5, comparable to the geometric surface area enhancement. The NbO_2 supports in Set 2 had a slightly higher SEF ($\sim$6), but appear to have a much larger geometric surface area (see Figure 3.3). The geometric surface area of the NbO + NbO_2 supports (Set 3) appears to be similar to the NbO_2 supports, but with slightly larger voids between posts. The larger gaps between posts lead to better Pt incorporation, electrical conductivity similar to the Pt-coated Nb_2O_5 supports, and higher SEFs ($\sim$10). We speculate that the low Pt on NbO_2 mass activity can be explained by a thick (multiple grains, many tens of nm) layer of Pt concentrated on top of the NbO_2 supports as suggested by the side view images in Figure 3.4. This Pt morphology leads to poor electrochemical usage of the catalyst; activity could be improved by better dispersion of the Pt on the high surface area supports. Furthermore, alloying elements (e.g., Ni) could be used to further improve the mass activity of the catalysts [82]. The aligned macropores inherent to GLAD films enable a wide range of wet and dry Pt incorporation techniques (e.g., high pressure sputtering or electrochemical deposition). Metal oxide stability allows for post-deposition treatment which may provide a path to optimizing Pt distributions on a

given support material and morphology through subsequent annealing or catalyst activation steps.

3.4 Conclusions

GLAD was successfully combined with post-deposition annealing to fabricate porous Nb_2O_5, NbO_2, and NbO + NbO_2 catalyst supports. Pt deposited on the high surface area supports led to SEFs ranging from 5 to 10, depending on the support morphology. NbO_2 and NbO + NbO_2 supports mimic the morphology of 3M's NSTF and offer the potential for similar surface area enhancement and mass activities. Through-post conductivity in NbO + NbO_2 supports allows for an additional or alternative conductive path through the support material. Support material, morphology, and phase allow for additional experimental degrees of freedom. It should be noted that our structured Nb-O supports were able to withstand aggressive electrochemical testing (up to 1.4 V vs. RHE), high temperatures (1000 °C), and significant handling without damaging their high surface area morphology, which is encouraging for future exploration of metal oxides and the GLAD structuring technique.

The combination of high surface area (with accessible pores) and low ohmic resistance was shown to be a key property of high performance electrochemical supports. While the crystalline phase of a metal oxide can be chosen and its quality optimized, stoichiometric metal oxide phases are limited by their intrinsic properties. Doping has been used in metal oxides in a variety of applications, and doped metal oxides have been suggested as a route towards improving the electrical conductivity of catalyst supports. Chapter 4 builds toward doped metal oxide nanostructures, with a demonstration of Nb-doped TiO_2 nanopillars. On route to functionally doped nanostructures, composition control, phase characterization, and dopant

activation are of key importance to study.

4

Toward Doped Metal Oxide Nanopillar Films

A version of this chapter has been published:

R.T. Tucker, N.A. Beckers, M.D. Fleischauer, and M.J. Brett, "Electron beam deposited Nb-doped TiO_2 toward nanostructured transparent conductive thin films," Thin Solid Films **525**, *28–34 (2012) [145].*

4.1 Introduction

Transparent conducting oxides (TCOs) are widely employed as electrodes in optoelectronic devices, such as organic photovoltaic and electroluminescent devices, because of their high electrical conductivity and optical transmittance [91, 97, 146–148]. Tin-doped indium oxide (ITO) is the most widely used TCO because of its low resistivity ($\sim 10^{-4}$ Ω cm), high transmittance in the visible range (80–90%), and low-temperature deposition [97, 149, 150]. Due to the increasing demand for and cost of indium there is interest in finding indium-free TCOs with comparable optical and electrical properties [100, 150, 151]. Contending indium-free transparent conductors include alternative doped metal oxides, networks of carbon nanotubes or metal

nanowires, and graphene films [94]. Aluminum-doped zinc oxide, tantalum-doped titanium dioxide, and niobium-doped titanium dioxide (TNO) have shown potential as doped metal oxide TCOs [148]. TNO also demonstrates some properties not exhibited by ITO or other traditional TCOs, including a high activation ratio of Nb (greater than 80%), long plasma wavelength, high refractive index in the visible region, high anisotropic conductivity, and chemical stability under strongly reducing conditions [152]. These additional desirable properties make TNO potentially applicable to a broader range of applications than traditional TCOs.

TNO fabricated by pulsed laser or sputter deposition has demonstrated good conductivity and transparency on single crystal substrates ($SrTiO_3$ or $LaAlO_3$) [77, 151, 153–159] , and glass/quartz substrates [147, 150, 159–170]. The epitaxially grown films initially showed superior properties to polycrystalline films grown on glass substrates [159], but performance of non-epitaxial films has since become comparable. TNO thin films have also been prepared by sol-gel coating or nanoparticle dispersion methods [76, 81, 148, 171–175]. These mesoporous films have much higher resistivity than films deposited from physical vapour methods, attributed to grain boundary scattering and defects [81]. Table 4.1 displays resistivity and transmittance values of some of the best reported TNO films fabricated by each method.

Nanostructured transparent conductors are of significant interest for improving devices since nanomaterials can exhibit large surface-to-volume ratios and other unique properties [113]. Organic electroluminescent [11] and photovoltaic [13] devices have shown device improvements for nanostructured ITO. Therefore, the development of nanostructured ITO-free transparent conductors would be advantageous. Thus far, TNO nanoparticles and mesoporous nanoparticle-based films [81, 176–178], electrospun nanofibers [179], and nanotube films [180, 181] have been demonstrated. These

Table 4.1. *Recent reports of TNO films prepared by various methods and their properties. Methods include pulsed laser deposition (PLD), sputter deposition, sol-gel coating, nanoparticle dispersion (NP), and electron beam evaporation (e-beam). Lowest reported resistivity (ρ_{min}) and integrated visible transparency ($\%T_{vis}$) are included where available.*

Method	Substrate	ρ_{min} (Ω cm)	$\%T_{vis}$	Ref.
PLD	$SrTiO_3$	2.3×10^{-4}	94%[a]	[153]
PLD	$LaAlO_3$	3.99×10^{-4}	-	[155]
PLD	glass	6.7×10^{-4}	60%	[166]
sputter	$SrTiO_3$	3.33×10^{-4}	80%[a]	[151]
sputter	$LaAlO_3$	3.0×10^{-4}	-	[152]
sputter	quartz	2.4×10^{-4}	60–80%	[147]
sol-gel	glass	0.5	30–40%[b]	[175]
NP	glass	4	-	[81]
e-beam	quartz	1.2×10^{-2}	70%	this work

[a] Internal transmission (corrected for reflection and scattering).

[b] Value estimated from optical transmittance vs. λ plot.

techniques for nanostructuring TNO are limited in the range of structures they can produce. Controlled porosity thin films of a variety of morphologies can be produced using the glancing angle deposition (GLAD) technique [19,20]. Electron beam evaporation of material is preferred for GLAD due to the collimation of the vapour flux. Thus, evaporation of TNO must be developed in order to enable use of this technique.

Electron beam evaporation requires sublimating or melting of the source material. Evaporation of multi-component source material produced by physical mixing of host and donor materials (e.g., TiO_2 and Nb_2O_5 powder) is therefore subject to melting point and vapour pressure differences in the component materials. Large differences, such as the $\sim$300 °C melting point difference between TiO_2 and Nb_2O_5, could lead to preferential evaporation of one component and challenges with composition control. Melting point differences can be minimized with synthesis of single-phase source materials. Here we use a sol-gel process to synthesize Nb-Ti-O

source material which is pressed and then evaporated under high vacuum. This facile, solution-based process allows for precise composition control of multi-component materials. Furthermore, because the metal alkoxides are mixed on a molecular level before hydrolysis and condensation are initiated, the dopant is intimately distributed throughout the entirety of the resulting product. This method is significantly quicker and more cost-effective for producing varied and irregular compositions compared to other easily accessible methods, such as ordering custom sputtering targets.

Nb-Ti-O source materials of various nominal Nb compositions were synthesized via this sol-gel method and evaporated to make thin films. The composition of the sol-gel source material and electron beam evaporated thin films were explored and compared to a sputtered thin film. The effect of post-deposition annealing on evaporated TNO films was investigated and the transparent conducting properties are correlated with doping, substrate heating, and annealing parameters. The GLAD technique was also used to demonstrate nanostructuring of TNO for future application as an indium-free high surface area transparent conductor.

4.2 Experimental Methods

4.2.1 Sol-gel Pellet Synthesis

Titanium(IV) isopropoxide (95%), niobium(V) ethoxide (99.999%) and hydrochloric acid (36% in aqueous solution) were purchased from Alfa Aesar and were used without further purification. Millipore water was used throughout. $Nb_xTi_{1-x}O_2$ source materials were prepared through modification of the procedure given by Gojković et al. [182]. Briefly, using $x = 0.06$ as an example target composition ($Nb_{0.06}Ti_{0.94}O_2$), 36.7 ml of titanium(IV) isopropoxide, 1.99 ml of niobium(V) ethoxide and 0.9 ml concentrated hy-

drochloric acid were added to a beaker with stirring. 4.8 ml of Millipore water was then added. The beaker was covered with parafilm, which was pierced several times. After 1 h of stirring, the parafilm was removed from the beaker and the gel was allowed to age and dry (open to the atmosphere) overnight. Once the gel had dried, yielding a white powder, a mortar and pestle were used to grind the material to a fine powder. The powder was then calcined in air at 200 °C for 2 h, and pressed into pellets ($\sim$5 mm diameter, $\sim$5 mm length) using an arbor press and custom mould. The pellets were sintered in air at 400 °C for 1 h, giving a material that was suitable for deposition by electron beam evaporation under high vacuum conditions.

4.2.2 Thin Film Evaporation & Processing

Thin films were deposited from the TNO source material on ($1 \times 1 \times 1/16$) inch quartz substrates (Quartz Scientific) in a high vacuum chamber. The quartz substrates were cleaned prior to deposition by ultrasonication in isopropanol (Fisher Scientific, 99.9%) for 10 minutes and were dried using a stream of nitrogen. Substrate holder rotation allowed for rotation about both the substrate normal axis (φ) and the angle between source flux and substrate normal (α), as shown in Figure 1.2. Source material, either custom TNO sol-gel pellets or a weighed mixture of Nb_2O_5 (Alfa Aesar, 99.95%) and TiO_2 (Cerac, 99.9%) pellets, was evaporated by an electron beam at a distance of 42 cm from the substrate. "Spitting" was observed from the melt, especially in the case of the sol-gel pellets, when the electron beam power was ramped up too quickly during the initial melting stage. Typical conditioning times were on the order of 1 h. Planar films were deposited at a fixed angle of $\alpha = 30^\circ$ and rotation about the substrate normal (φ) once every 10 nm of film growth. Film growth was monitored by crystal thickness monitor and maintained at (4 ± 1) Å/s to a total thickness of 300 nm. For

heated depositions, an irradiative heating system using two halogen light bulbs (minimum 150 W each) enabled temperatures as high as 350 °C to be obtained on the surface of the substrate. Temperature was measured by a thermocouple held ∼1 cm above the sample holder chuck. Uncertainty in the substrate temperature was approximately 20 °C, due to inconsistency in thermocouple height, substrate–chuck thermal contact area, and local heating variation.

Thin films were also deposited by sputtering for comparison of composition analysis techniques. Quartz substrates prepared as above were used. TNO films were sputtered from a custom fabricated 2 inch diameter $Nb_{0.06}Ti_{0.94}O_2$ target with a copper backplate (Super Conductor Materials, Inc.) using a pulsed DC power supply in voltage regulation mode. Target voltage was maintained at 550 V until a total of 2.5 MJ was delivered to the target at an Ar pressure of 0.4 Pa, resulting in ∼250 nm film thickness.

Post-deposition anneals on the thin films were performed in a 3 inch outer diameter three zone tube furnace with flowing 5% H_2/balance Ar forming gas (Praxair) controlled by a rotameter (flow rate 300 to 500 sccm). The following annealing routine was used: (i) 30 minute purge of forming gas at room temperature, (ii) ramp to annealing temperature at 10 °C/min, (iii) hold at annealing temperature (annealing temperature 450 to 700 °C), (iv) passive cool to below 90 °C before gas flow was stopped and the substrates removed.

4.2.3 Characterization

Composition analysis of source material and thin film samples was performed by X-ray photoelectron spectroscopy (XPS) and energy dispersive X-ray spectroscopy (EDX). XPS was performed with a Kratos ULTRA spectrometer. Only data from surface scans is displayed here as it has been pre-

viously reported that depth profiling of TNO cannot be reliably performed because both Ti and Nb oxides can be reduced by Ar^+ etching [147]. All high-resolution spectra were calibrated against the C 1s line at 284.8 eV arising from adventitious C. XPS quantification was performed to determine concentrations of elemental species in each sample. Following background subtraction, atomic concentrations were determined from integrated peak areas using the relative sensitivity factors determined by Crist [183]. EDX was acquired on a Zeiss EVO MA 15 scanning electron microscope (SEM) equipped with a Peltier-cooled Bruker Quantax 200 Si drift detector (10 mm^2). The sample was tilted at 60° from the substrate normal to increase the volume of film interacting with the beam. Quantification was performed by the peak-to-background ZAF method with the instrument software [184]. Film morphology was characterized by SEM imaging with a Hitachi S-4800 instrument. SEM samples were mounted on aluminum stubs and imaged without further coating. Thin film and sol-gel source material crystallinity was characterized via X-ray diffraction (XRD) on a Bruker D8 diffractometer and Rigaku Ultimate IV diffractometer, both with Cu K_α sources.

Sheet resistance was measured using a standard 4-point probe setup. The film area was large enough by comparison to the probe separation distance to satisfy the condition of a unity correction factor. Optical transmission was measured using a Perkin–Elmer NIR–UV spectrophotometer from wavelengths of 200 to 2500 nm. Transmission spectra shown are absolute, and the substrate has not been subtracted. The Haacke figure of merit (ϕ_{TC}) was calculated for comparison to other TCOs. Equation (1.1) defines ϕ_{TC} for sheet resistance (R_s) and optical transmission (T) [93]. Optical transmission in the visible range is used (400 nm $< \lambda <$ 750 nm). Typical high quality transparent conductors have $1 \times 10^{-3}\ \Omega^{-1} < \phi_{TC} < 50 \times 10^{-3}\ \Omega^{-1}$ [93].

4.3 Results & Discussion

4.3.1 Pellet & Film Composition

A series of TNO electron beam evaporation source materials of nominal composition $Nb_xTi_{1-x}O_2$ (x = 0, 0.03, 0.06, 0.12, 0.24) was prepared by the sol-gel method by varying the molar ratio of niobium(V) ethoxide to titanium(IV) isopropoxide. Once the resulting powder was calcined, pressed into pellets and sintered, XRD patterns were obtained to confirm that there was good incorporation of the dopant throughout the samples. XRD patterns (shown in Figure 4.1) match well with the pattern for anatase TiO_2 for lower Nb compositions (x = 0, 0.06, 0.12), suggesting a substitutional replacement of Ti with Nb, as expected. The XRD pattern for the highest prepared Nb composition (x = 0.24) shows the pellets to be almost completely amorphous, with only a hint of the most intense anatase peak. Slight shifts in peak position to lower angle (Figure 4.1, inset) are consistent with an increase in the lattice constant as the Nb content increases. In addition, the intensity of the anatase peaks decreases with increasing Nb content, suggesting that the incorporation of Nb inhibits anatase grain growth. This has been previously observed and has been attributed to the larger Nb^{5+} radius putting stress on the TiO_2 lattice and hindering the growth of anatase crystallites [173]. Peaks of niobium oxide phases were not observed in the XRD patterns for any of the different compositions, further indicating good Nb incorporation.

High-resolution XPS spectra of TNO source material pellets (x = 0, 0.06, 0.12, 0.24) and thin films (x = 0.06) are shown in Figure 4.2(a)–(b), respectively. Binding energy (BE) values for the different oxidation states of Ti and Nb were determined using the average values reported for each respective oxide in the NIST XPS database [185]. For the high-resolution scan of the Ti 2p peaks shown in Figure 4.2(a), both peaks correspond with Ti^{4+}, which

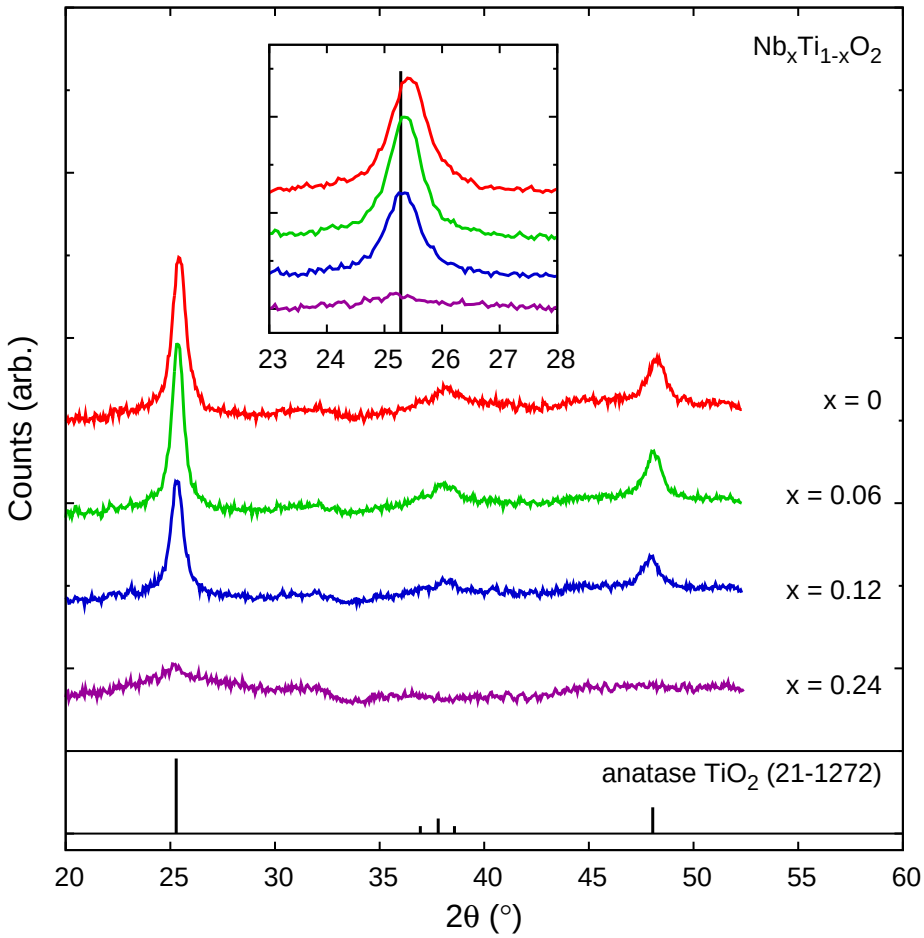

Figure 4.1. *X-ray diffraction patterns of $Nb_xTi_{1-x}O_2$ sol-gel source pellets (x = 0, 0.06, 0.12, 0.24). Inset magnifies shift in peaks near $2\theta \approx 25°$ and scans are offset vertically for clarity. Reference TiO_2 (anatase) pattern (PDF 21-1272) is included. Data from [145].*

correlates with the oxidation state of the metal alkoxide used to prepare the source material. For the Nb 3d peaks shown in Figure 4.2(a) there is an observable chemical shift in the BEs of the peaks when compared to the reference values, suggesting that the Nb present in the source material is likely a mix of Nb^{4+} and Nb^{5+} [186]. The amplitude of the Nb 3d peaks is appropriately increasing with increasing nominal Nb content (x).

The high-resolution XPS spectra of the thin films evaporated with and without substrate heating at $\sim$330 °C are similar, shown in Figure 4.2(b). Both exhibit more Nb^{5+} character than the pellets, with a subtle change in peak shape present between the unheated and 330 °C samples. The Ti^{4+} peaks appear the same. Overall, XPS indicates that substrate heating during deposition does not have a strong effect on the composition of evaporated TNO films.

The XPS and EDX measurements allowed for calculation of relative atomic compositions of Nb and Ti in prepared samples. For ease of comparison, the ratio of Nb atomic percentage to combined Nb and Ti atomic percentage is reported as (Nb/(Nb+Ti) or $x/(x+y)$ from $Nb_xTi_yO_2$). The values calculated both for the pellets and thin films from EDX and XPS data are provided in Table 4.2. Nominal values refer to the molar ratios of metal alkoxides used to prepare the source materials. In all cases, the ratios calculated from XPS data report equal or greater Nb concentration than those calculated from EDX data. The relative Nb content measured for the sol-gel source pellets agree reasonably well with the nominal values, with the values from EDX lower than nominal and the values from XPS slightly higher than nominal. The Nb content nearly doubles with each nominal composition step, as expected.

Measured Nb/(Nb+Ti) thin film composition is farther from agreement with the nominal values, but still maintains the same trend with increasing

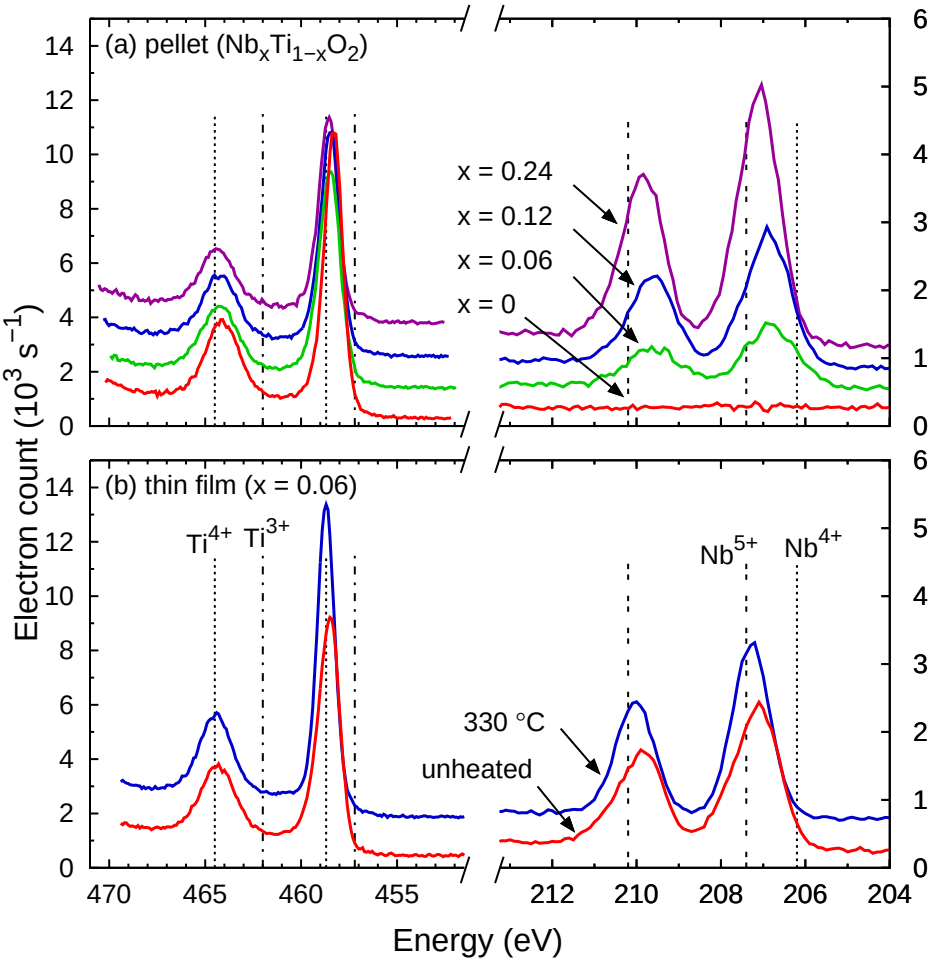

Figure 4.2. *X-ray photoelectron spectra near Ti 2p and Nb 3d peaks of (a) sol-gel prepared source pellets of nominal composition $Nb_xTi_{1-x}O_2$ (x = 0, 0.06, 0.12, 0.24) and (b) evaporated thin films (x = 0.06) deposited without (unheated) and with substrate heating (330 °C). Binding energy references for Ti^{3+}, Ti^{4+}, Nb^{4+}, and Nb^{5+} are included. Spectra are offset vertically for clarity. Data from [145].*

Table 4.2. *Relative composition of Nb to Ti ($x/(x+y)$ in $Nb_xTi_yO_2$) for sol-gel pellets and thin films calculated from EDX and XPS. All films are evaporated from pellets with substrate temperature of (330 ± 20) °C unless otherwise noted.*

	Measured $x/(x+y)$				
Nominal	Pellet		Thin Film		
$x/(x+y)$	EDX	XPS	EDX	XPS	Notes
0	0.00	-	0.01	-	
0.06	0.05	0.08	0.13	0.15	
			0.15	0.15	[a]
			-	0.20	[b]
			0.07	0.09	[c]
0.12	0.09	0.15	0.22	0.29	
0.24	0.18	0.26	0.37	0.42	

[a] Evaporated $Nb_xTi_yO_2$ pellets and unheated substrate.
[b] Evaporated Nb_2O_5–TiO_2 mixture.
[c] Sputtered from $Nb_{0.06}Ti_{0.94}O_2$ target.

nominal Nb content. Again, the values reported from XPS data are higher than those reported from EDX data. In all cases, the measured Nb content is higher than the nominal Nb content, and increases with increasing nominal Nb content. The relative Nb content in the unheated sample (x = 0.06) is in good agreement with that of the sample of the same nominal composition deposited at ∼330 °C for both EDX and XPS measurements, indicating that substrate heating does not affect measured Nb concentration.

A sputtered thin film (x = 0.06) and an evaporated Nb_2O_5–TiO_2 mixture film (x = 0.06) were also included in Table 4.2 for comparison to sol-gel evaporated thin film EDX and XPS measurements. The sputtered film was expected to have very comparable stoichiometry to the sputter target ($Nb_{0.06}Ti_{0.94}O_2$). However, the sputtered film still measured rich in Nb, with XPS again reporting higher Nb content than EDX. The relative sensitivity values used in the XPS quantification procedure are likely the source of this discrepancy, as even XPS-calculated compositions of stoichiometric oxides

are often unreliable for absolute element-to-element composition comparisons [183]. Regardless, the Nb/(Nb+Ti) ratio is still valid for comparison across the different sample sets. The mix sample, prepared by evaporating an appropriate mixture of Nb_2O_5 and TiO_2, has the highest measured Nb content for the $x = 0.06$ composition with Nb/(Nb+Ti) = 0.20.

The difference between the sputtered and evaporated film compositions measured by both EDX and XPS can be readily explained. The phase diagram of the Nb_2O_5–TiO_2 system shows Nb content to decrease the melting temperature (T_m) of the TiO_2 mixture, from ∼1800 °C at 0% to ∼1650 °C at 10% to ∼1500 °C at 50% Nb_2O_5 [187]. Vapourization studies of Nb_2O_5–TiO_2 by electron beam evaporation show preferential evaporation of Nb compounds [188]. From the data in Ref. [188], a mixture of "50 mol % TiO_2–50 mol % Nb_2O_3 [sic]" has a relative Nb/(Nb+Ti) content of ∼0.67 in the solid form, but can be calculated to have Nb/(Nb+Ti) ∼0.80 in the evaporated products. This preferential evaporation of Nb compounds appears to be exaggerated for electron beam evaporation compared to thermal evaporation. The initial justification for using "single phase" sol-gel pellets instead of a "two phase" Nb_2O_5–TiO_2 powder mixture is still valid. During the solid-to-liquid transition, the Nb_2O_5 compounds in the two phase mixture would begin melting before the TiO_2. The single phase mixture would melt at one temperature, effectively delaying the onset of preferential Nb evaporation. Once in liquid form, Nb compounds in both cases ultimately dominate the evaporated species, clearly limiting precise composition control in electron beam evaporated TNO films. Deposition rate control and other methods may offer routes to mitigate composition variations.

XRD was performed to complement the composition characterization with crystallinity studies of the TNO thin films. XRD patterns are shown in Figure 4.3 for films of composition $x = 0.06$ deposited without substrate

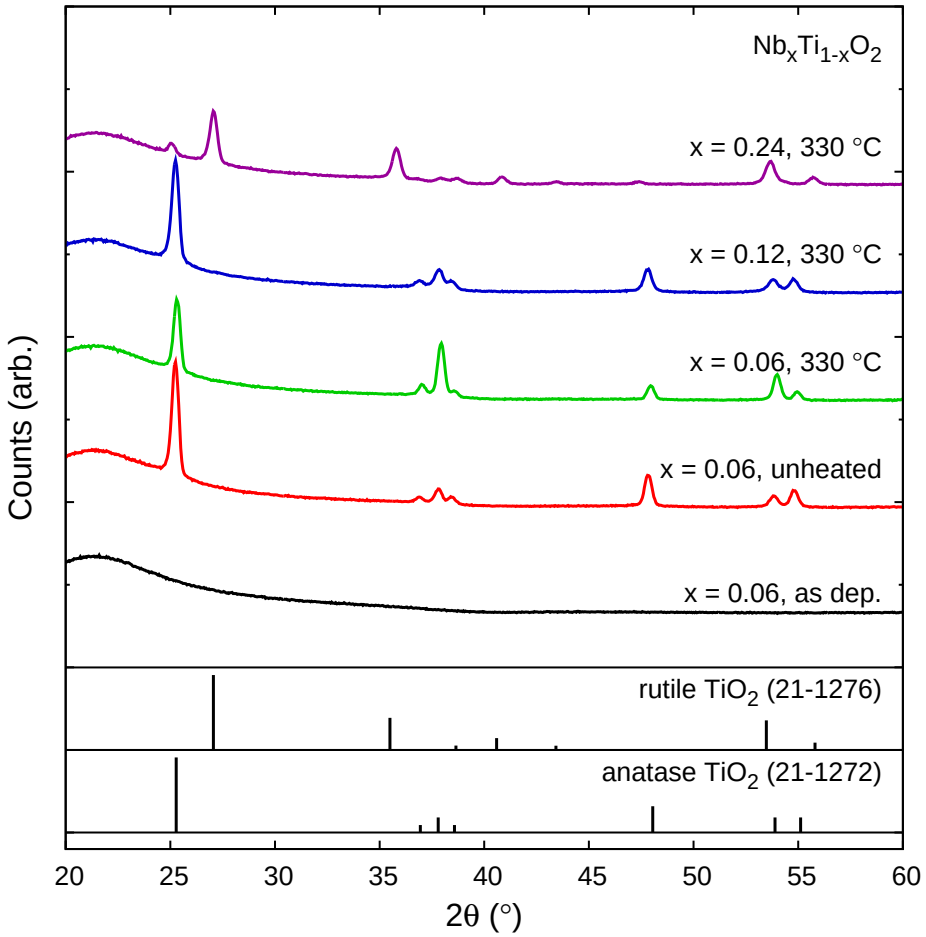

Figure 4.3. *X-ray diffraction patterns of electron beam evaporated thin films of nominal composition $Nb_xTi_{1-x}O_2$ (x = 0.06, 0.12, 0.24) deposited at noted temperature. All films annealed at 500 °C in 300 sccm 5% H_2/Ar, excluding "x = 0.06, as dep.". Reference TiO_2 (anatase and rutile) patterns (PDF 21-1272 and 21-1276, respectively) are included. Data from [145].*

heating both as deposited and after annealing, as well as for films of compositions x = 0.06, 0.12, 0.24 deposited at ∼330 °C after annealing. As deposited films, whether deposited with or without substrate heating, were amorphous and showed no diffraction peaks. The annealing conditions for films in Figure 4.3 (excluding "as deposited") were 1 h at 500 °C with 300 sccm 5% H_2/Ar forming gas. After annealing at temperatures ranging from 450–500 °C (not all shown), the TNO thin film XRD peaks for $x \leq 0.12$ matched well with the anatase TiO_2 pattern. For higher Nb content (x = 0.24), the TNO film peaks matched the rutile TiO_2 pattern mixed with small anatase peaks. Other reports have noted rutile phase formation in TNO films at temperatures as low as 400 °C [160] and increasing rutile formation with increased Nb content [174, 186].

The morphology of the TNO films, as seen in Figure 4.4, was observed to be typical of planar polycrystalline thin films. Small grains – on the order of 10s of nm – can be seen in the cross-section of the film which are consistent with the polycrystalline nature determined by XRD.

4.3.2 Thin Film Transparent Conductor Properties

The electron beam deposited TNO films were characterized for transparency, conductivity, and combined transparent conductor merit. As the nominal $Nb_xTi_{1-x}O_2$ stoichiometry is known to be inexact from composition characterization, films will be referred to as $Nb_xTi_yO_2$ in the remainder of this report, with reference to nominal x values. In-plane resistivity measurements were obtained for several annealed $Nb_xTi_yO_2$ (nominal x = 0.06, y = 0.94) thin films deposited with and without irradiative substrate heating up to ∼330 °C (Figure 4.5). Overall, the resistivity of the thin films decreases as the deposition temperature increases. Further increases in substrate temperature during deposition may lead to even lower resistivity values, how-

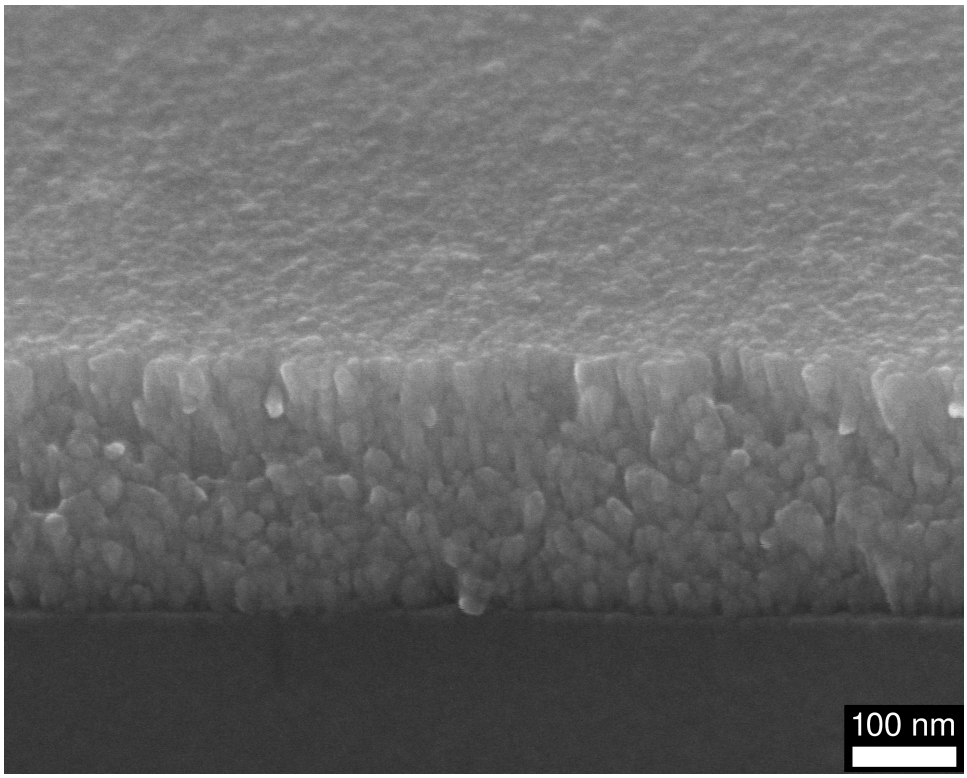

Figure 4.4. *Oblique view scanning electron microscopy image of TNO film deposited at 275 °C near normal incidence (α = 30°). Image from [145] copyright © 2012 Elsevier.*

ever, there is likely an optimum temperature where minimum resistivity is achieved. It has been suggested that this temperature is less than 400 °C for sputtered films [151], but there is no indication that this will hold true for electron beam evaporated films. The post-deposition annealing of the TNO films is critical for the conductivity of TNO as it has been previously shown that the conductivity of TNO is dependent on the oxygen stoichiometry of the material, and only oxygen-deficient TNO possesses conductive properties [155, 163, 165]. When no substrate heating during deposition was applied, the most conductive films were those that were annealed at higher temperatures and with a higher flow rate of forming gas. As the

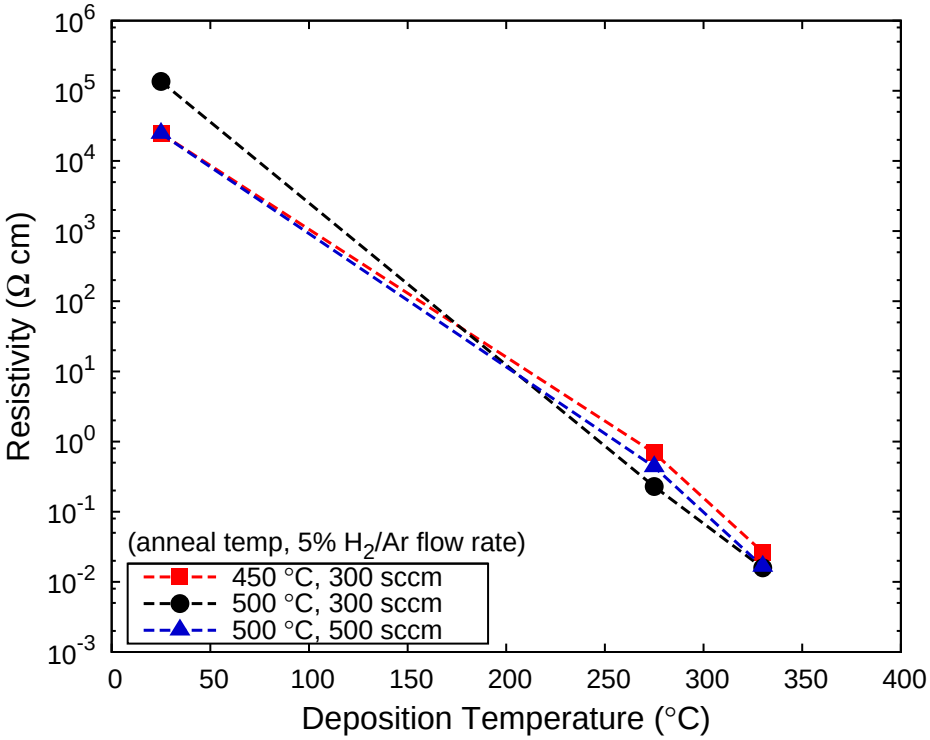

Figure 4.5. *Resistivity of $Nb_xTi_yO_2$ (nominal $x = 0.06$, $y = 0.94$) thin films as heated to different temperatures during deposition for different post-deposition annealing temperatures and 5% H_2 forming gas flow rates. Data from [145].*

substrate deposition temperature was increased, the trend with regards to annealing temperature and flow rate begins to invert with the most conductive films being those annealed under milder temperatures and forming gas flow rates. Ultimately, the highest deposition temperature (∼330 °C) yielded the most conductive sample of this composition ($x = 0.06$) with a resistivity of 1.6×10^{-2} Ω cm.

In addition to examining the conductivity of the samples as a function of composition, the optical transparency of the TNO thin films was measured. Figure 4.6 shows the transmission of representative films ($x = 0.06$, ∼330 °C deposition temperature) both as deposited and after various post-deposition

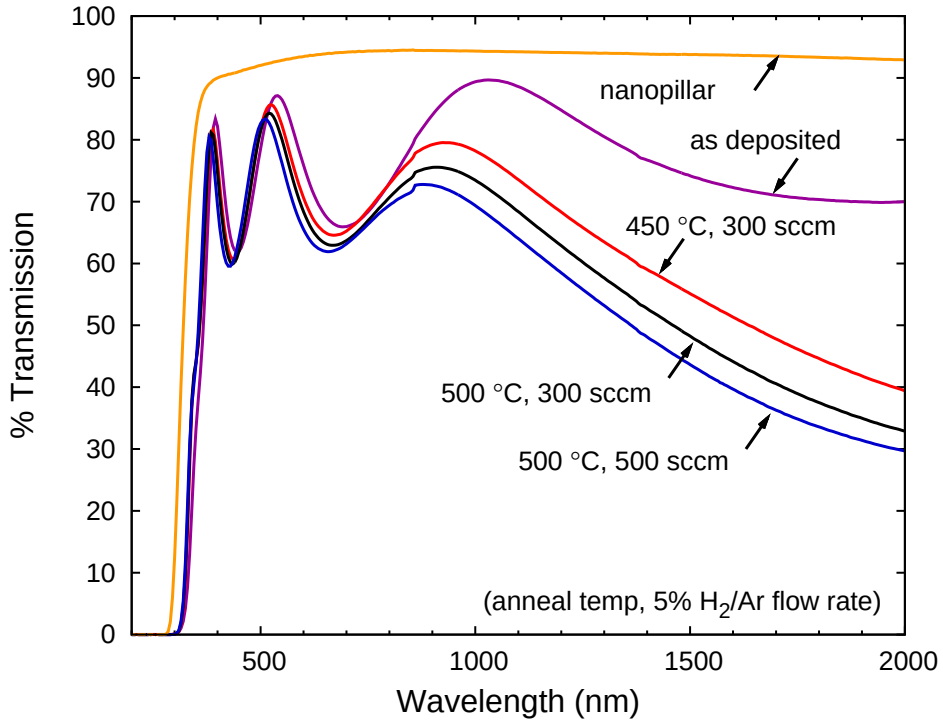

Figure 4.6. *Optical transmission of $Nb_xTi_yO_2$ (nominal $x = 0.06$, $y = 0.94$) thin films evaporated at a substrate temperature of 330 °C, as deposited and after annealing at various temperatures and 5% H_2/Ar flow rates. Data shown is from 300 nm planar films in all cases except "nanopillar", which is a 200 nm nanopillar film deposited at $\alpha = 85°$. Data from [145].*

annealing conditions. The transmission scans show typical fringes as well as decreasing transparency with either increasing temperature or increasing forming gas flow rate. While the transparency in the visible region is changing only slightly for the different annealing conditions, transmission at infrared wavelengths is much more affected by temperature and forming gas flow rate. This reduced transmission is consistent with increased free electrons and the improved conductivity noted for these annealing conditions.

The effect of Nb content on transparent conducting properties was inves-

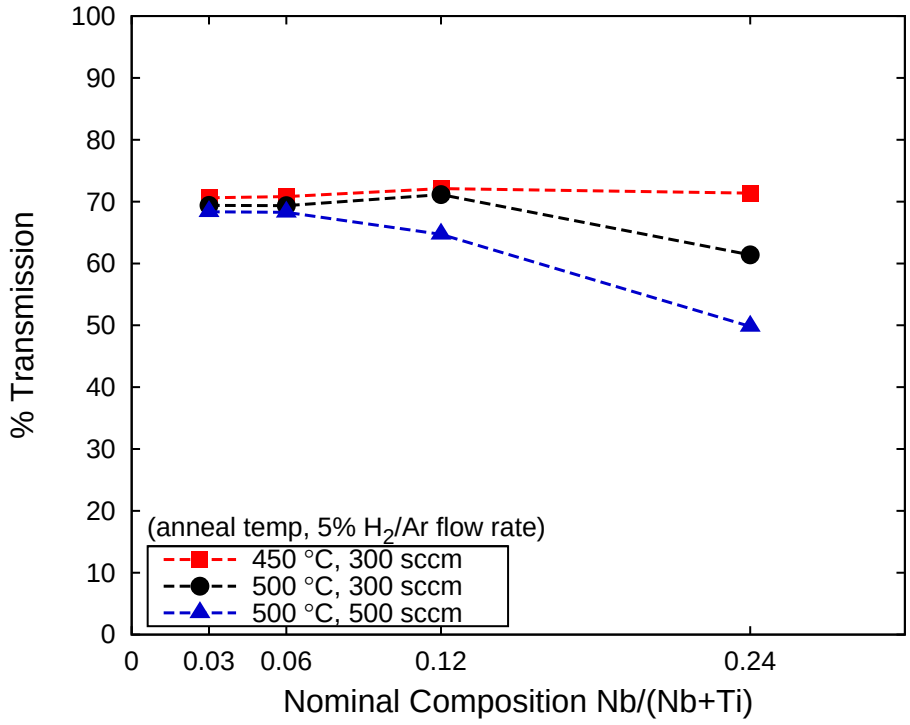

Figure 4.7. *Optical transparency of $Nb_xTi_yO_2$ thin films of different nominal compositions for various post-deposition annealing conditions. Transmission is averaged in the wavelength range 400 nm $< \lambda <$ 750 nm. Data from [145].*

tigated and the results are summarized in the following. Films of different nominal $Nb_xTi_yO_2$ compositions (x = 0, 0.03, 0.06, 0.12, 0.24; $y = 1 - x$) were deposited with substrate heating at ~330 °C and annealed under different temperatures and forming gas flow rates. The films with composition x = 0 were insulating for all anneal conditions shown and thus the TCO properties are not shown in the figures. The integrated transmission over the visible light window in terms of Nb composition is shown in Figure 4.7. With a low ratio of Nb/(Nb+Ti), the post-deposition annealing conditions had little effect on the optical transmission with all of the samples transmitting approximately 70% of light in the visible region (as shown in Figure 4.6).

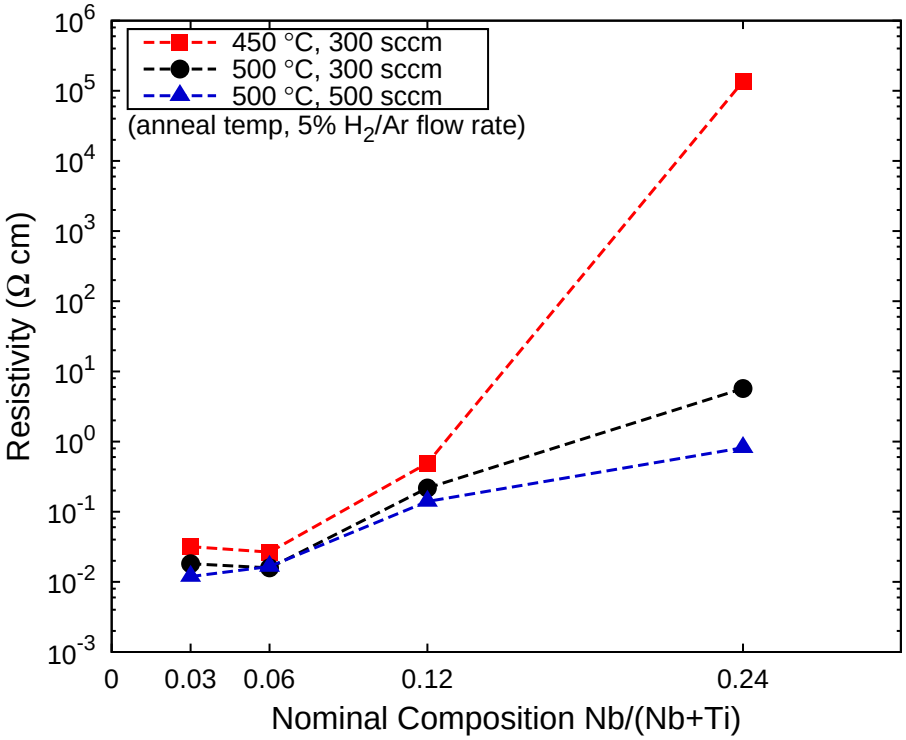

Figure 4.8. *Resistivity of $Nb_xTi_yO_2$ thin films of different nominal compositions for various post-deposition annealing conditions. Data from [145].*

However, as the ratio of Nb to Ti was increased, the annealing conditions have a larger effect on the transparency of visible light with samples annealed under milder conditions having higher transmission values.

The effect on the resistivity as the composition of the TNO thin films was varied is shown in Figure 4.8. The lower Nb compositions resulted in less resistive samples, with the $x = 0.03$ and $x = 0.06$ samples plateauing near the same values in the low 10^{-2} Ω cm range. For all compositions, anneals at 450 °C yielded the more resistive samples, with this effect amplified at the higher compositions ($x = 0.24$). At the lower doping amounts, the post-deposition annealing conditions had less effect on the resistivity of the samples. The lowest resistivity attained was 1.2×10^{-2} Ω cm for a film of

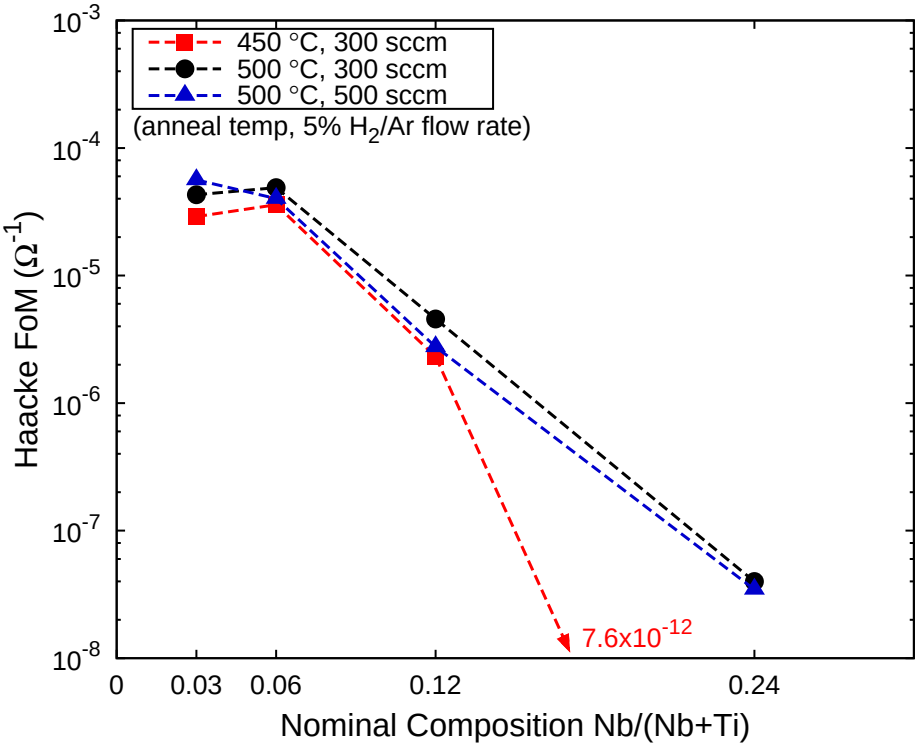

Figure 4.9. *Haacke figure of merit for $Nb_xTi_{1-x}O_2$ thin films of different nominal compositions for various post-deposition annealing conditions. The point at Nb/(Nb+Ti) = 0.24 for anneal conditions "450 °C, 300 sccm" is outside of the lower axis limit. Data from [145].*

nominal composition $x = 0.03$ deposited at ~330 °C and annealed for 1 h at 500 °C with 500 sccm 5% H_2/Ar flow. While a true minimum resistivity was not located for these samples, it is important to recall that the $x = 0$ sample (TiO_2) was extremely resistive. Thus the optimal Nb doping level for high conductivity is likely near the range of $0.03 < x < 0.06$.

The corresponding Haacke figure was calculated for the TNO thin films and are provided in Figure 4.9. The desirable range of good TCOs is $1 \times 10^{-3}\ \Omega^{-1} < \phi_{TC} < 50 \times 10^{-3}\ \Omega^{-1}$. As the ratio of Nb to Ti decreases there was an increase in the Haacke figure of merit, primarily driven by

the increasing conductivity. Similar to the transparency and conductivity, annealing conditions have an impact on the overall performance as a TCO. However, in some cases the transparency is sacrificed for conductivity (or vice versa), leading to a comparable ϕ_{TC}. Regardless, the TCO figure of merit for electron beam deposited TNO had a best value of $\phi_{TC} = 5.6 \times 10^{-5}\ \Omega^{-1}$, which is still two orders of magnitude short of high performance transparent conductors.

The TCO performance of electron beam deposited TNO films reported here is primarily limited by low conductivity at this point, as the transparency of most films is near 70%. Conductivity may be further improved though increased composition control through the film, increased deposition temperatures, optimized film thickness, and optimized annealing conditions. These early results are promising and possible improvements may be addressed in future work.

4.3.3 Nanostructured Thin Films

As previously mentioned, one motivation for developing electron beam evaporation of doped materials is to allow for nanostructuring based on collimated vapour shadowing (i.e., GLAD). The 300 nm films used throughout this study were deposited with the vapour flux near normal incidence to the substrate, leading to planar films as shown in Figure 4.4. TNO films were also deposited at glancing deposition angles both with and without substrate heating. Figure 4.10 shows an image of a GLAD nanopillar film deposited at an angle of $\alpha = 85^{\circ}$ between the vapour flux and substrate normal, at a substrate temperature of 275 °C. The nanopillar sample exhibits very high optical transmission, as shown in Figure 4.6, resulting from the lower overall mass, effective refractive index, and specular reflection of the porous film. This is a demonstration of nanostructured TNO films via

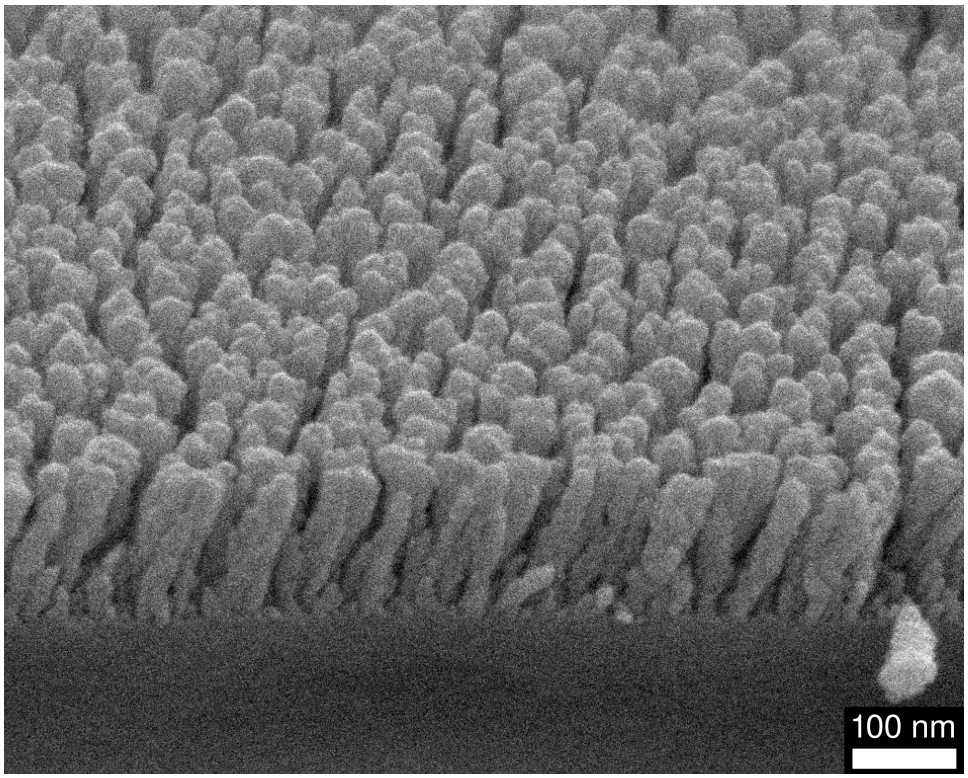

Figure 4.10. *Oblique view scanning electron microscopy image of a nanopillar TNO film deposited at 275 °C at a deposition angle of $\alpha = 85°$. Image from [145] copyright © 2012 Elsevier.*

GLAD. More complex structures, including zig-zags, helices, and combinations thereof, are readily possible with this technique. Electrical conduction in the nanopillar TNO films is orthogonal to the substrate, and thus conductivity measurement will require "through-post" methods such as those used recently to measure the conductivity of GLAD ITO nanopillars [189].

It is known that increased adatom diffusion at higher substrate temperatures decreases the shadowing effects that GLAD nanostructuring is based upon [20], however, favourable nanostructuring behavior has been demonstrated here in the temperature range of interest. Post-deposition annealing can also lead to morphology degradation of GLAD films at sufficiently high

temperatures as shown in Chapter 2. The annealing regime (∼500 °C) is below $0.4T_m$ for most TNO compositions of interest, and thus post-deposition heating in this range is expected to have minimal effect on GLAD TNO morphology. Fabrication of functional nanostructures via GLAD is possible, and further optimization of functional properties and morphology preservation is the next step toward the inclusion of nanostructured TNO as a transparent electrode in energy conversion devices.

4.4 Conclusion

A sol-gel method was used to prepare TNO source materials suitable for electron beam evaporation under high vacuum. Evaporated TNO thin film composition was found to be Nb rich compared to the source material, but scaled appropriately with the Nb content of the source material. Through examination of substrate heating during deposition and the Nb/(Nb+Ti) ratio, it was found that elevated substrate temperatures gave the lowest resistivity thin films with a measured value of 1.2×10^{-2} Ω cm at substrate temperature ∼330 °C for nominal $x = 0.03$. When the Haacke figure of merit was calculated for thin films of various Nb/(Nb+Ti) ratios deposited with substrate heating, decreasing performance was observed with increasing Nb content. Thin films of nominal $x = 0.03$ and 0.06 exhibited the highest measured ϕ_{TC} after annealing. TNO films were nanostructured using the GLAD technique, and offer a route toward highly controllable nanostructures in ITO-free transparent conductors.

While significant development is still required to realize high quality Nb-doped TiO_2 nanopillars, transparent conductive nanostructures can be fabricated in other material systems. ITO-free transparent conductors will become increasingly desirable if the price of In continues to increase with widespread usage. In the meantime, however, ITO offers an excellent plat-

form to explore the potential application of nanostructured electrodes. The following two chapters will focus on the development of ITO nanostructures, specifically control over unique morphologies. Chapter 5 introduces the method (vapour-liquid-solid glancing angle deposition – VLS-GLAD) used for growing branched ITO nanowires, and shows a demonstration of morphologies possible with the technique. Implications of VLS-GLAD will then be further unraveled in Chapter 6 with a model and demonstration of highly controlled branch diameter rippling.

5

Vapour-Liquid-Solid Glancing Angle Deposition of Indium Tin Oxide Branched Nanowires

A version of this chapter has been published:

A.L. Beaudry, R.T. Tucker, J.M. LaForge, M.T. Taschuk, and M.J. Brett, "Indium tin oxide nanowhisker morphology control by vapour-liquid-solid glancing angle deposition," Nanotechnology **23**, *105608 (2012) [190].*

R.T. Tucker, A.L. Beaudry, J.M. LaForge, M.T. Taschuk, and M.J. Brett, "Branched Nanowires and Method of Fabrication," United States Patent Application #14/092,720 (2013) [191].

5.1 Introduction

Indium tin oxide (ITO) is a transparent conductive oxide [192] which is commonly used in organic light-emitting devices [193,194], flat-panel displays and touchscreens [97], and organic solar devices [195,196]. The organic photovoltaic (OPV) community has shown interest in nanostructured ITO films for high surface area electrodes [13,101,105,109,197,198]. OPVs are often limited either by light absorption or charge extraction. High surface area

electrodes decouple these two limiting factors by allowing for increased absorption while maintaining short charge extraction distances. Conductive pathways throughout the active layer allow the active layer thickness to be increased beyond the exciton diffusion length, motivating the development of nanostructured electrodes [13, 195, 198].

Nanostructured electrodes with increased surface areas have been fabricated using anodic aluminium oxide templates [108, 197], organic vapour phase deposition [195, 198] and vapour-liquid-solid (VLS) growth of high aspect ratio nanowhiskers [101, 105, 109]. VLS is a crystal growth technique that results in high surface area nanostructures that grow primarily in one dimension [26, 28]. ITO nanowhisker films can be grown with a self-catalyzed VLS growth mode accessible at elevated substrate temperatures [199–201]. Beyond applications as high surface area electrodes, ITO nanowhiskers are applicable as gas sensors [202], protein molecule sensors [203] and UV light sources [204].

During physical vapour deposition of ITO, self-catalytic indium-tin alloy liquid droplets form on the substrate's surface if the substrate is heated above the alloy's eutectic point [40]. The liquid droplet collects impinging vapour atoms as it has a high sticking coefficient (the ratio of atoms adsorbed to the total number of atoms incident on the surface) with respect to the substrate [26, 28, 205]. Nucleation occurs preferentially at the droplet-substrate interface, restricting the nanowhisker's lateral growth [26, 28]. This results primarily in crystal growth in one dimension, with the primary axis (trunk) normal to the liquid-solid interface.

ITO nanowhiskers exhibit distinctive growth of branches orthogonal to the axial growth direction of the nanowhisker [40, 200, 206], reflecting the cubic bixbyite crystal structure of indium oxide [142, 207]. The branching mechanism produces high surface area nanowhiskers, which may improve

electrical access to OPV active device layers. ITO nanowhisker growth has been reported with a large range of substrates, flux rates, vapour incidence angles and deposition techniques [40, 108, 199–201, 206, 208–222]. However, a systematic study of the effect of highly oblique vapour incidence angle in combination with varied deposition parameters has not been completed.

Glancing angle deposition (GLAD) is introduced in detail in Section 1.2.1. By combining GLAD's control over the vapour flux with a heated substrate to induce VLS growth of ITO, we are able to precisely control ITO nanowhisker morphology in a hybrid crystal growth technique named VLS-GLAD. This useful combination was first demonstrated by Alagoz and Karabacak, who recently used VLS-GLAD to produce Ge nanocolumns [223]. Figure 5.1 depicts the VLS-GLAD parameter space relative to conventional GLAD, VLS and planar deposition. The VLS-GLAD region resides at elevated temperatures and high deposition angles (α). This chapter explores a systematic characterization of the effects of flux rate, angle of vapour incidence relative to substrate normal (α), pitch (nominal film thickness deposited per substrate rotation), and substrate temperature on ITO nanowhisker morphology. The density of preferential nucleation sites, and subsequently trunk density, is determined by the extent of geometric shadowing (controlled by α) caused by catalytic liquid In-Sn alloy droplets during nucleation. In addition, unique ITO nanowhisker morphology is obtainable via manipulating deposition angle, pitch and flux rate during growth. We examine the effects of deposition parameters on the nanowhisker morphological and transparent conductor properties expected to optimize OPV performance when used as an electrode, including trunk diameter, branch diameter, and trunk density (defined in Figure 5.2).

This chapter represents the initial exploration of the VLS-GLAD concept. More in-depth reports of VLS-GLAD include United States Patent Applica-

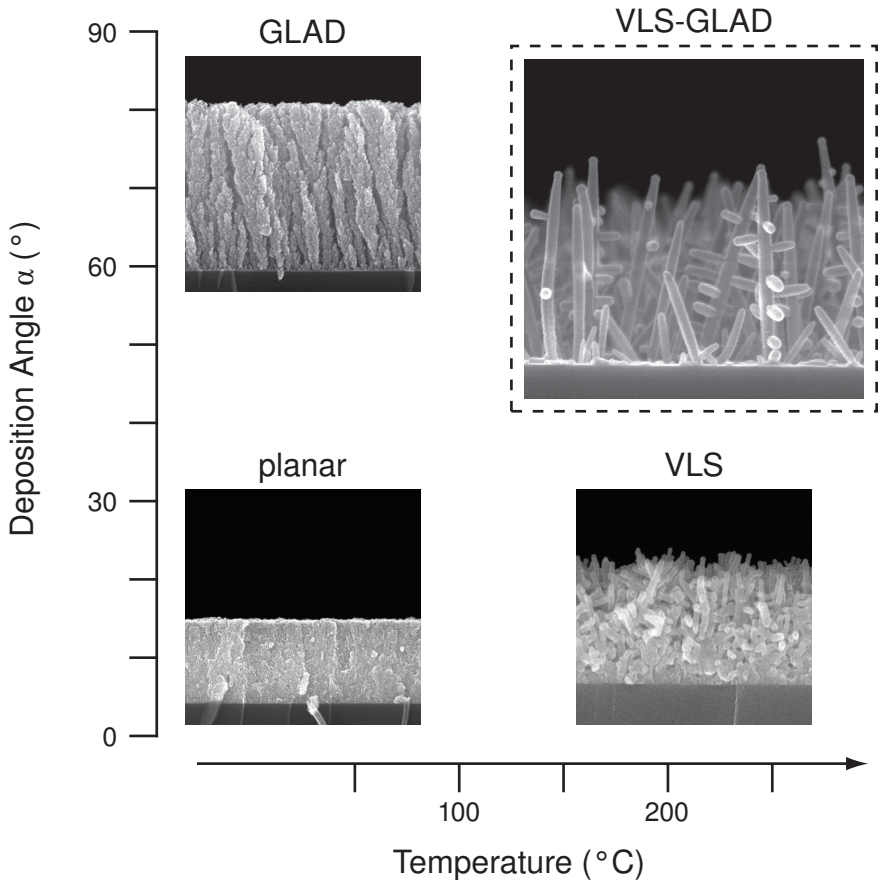

Figure 5.1. *Qualitative parameter space for planar, glancing angle deposition (GLAD) and vapour-liquid-solid (VLS) grown ITO films and nanowire networks. Combining high substrate temperature and high deposition angles produces unique morphologies in a process called VLS-GLAD. Images from [190] copyright © 2012 IOP Publishing.*

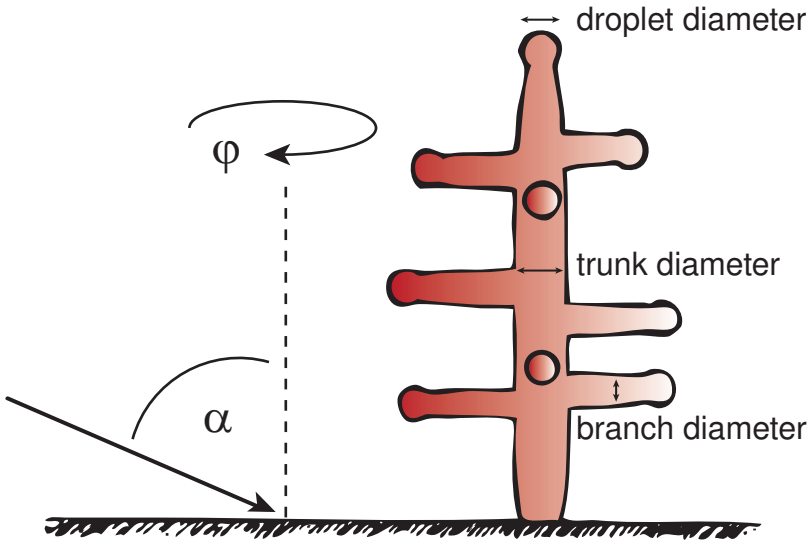

Figure 5.2. *Schematic definition of deposition angle (α) and the angle of rotation about substrate normal (φ) as used in VLS-GLAD. Typical branched nanowires are characterized as having a trunk, droplet, and numerous branches. Images from [190] copyright © 2012 IOP Publishing.*

tion #14/092,720 [191], several scientific reports [190, 224–227], and the PhD thesis of Allan Beaudry.

5.2 Experimental Methods

5.2.1 Film Fabrication

ITO nanowhisker films were deposited using a high vacuum (base pressure below 0.1 mPa) electron beam evaporation system (Kurt J Lesker, AXXIS) with a custom substrate motion controller capable of precisely controlling α (angle of vapour incidence) and φ (angle of substrate rotation around substrate normal) as shown in Figure 5.2. Substrate temperature was controlled by two halogen lamps illuminating substrates on a Cu chuck. Temperature was monitored by a cold-junction corrected (ASTM E2730-10 standard) [228]

thermocouple held approximately 1 cm above the substrate holder. The measured thermocouple temperature was found to be in agreement with the observed melting points of In and Sn pieces placed on Si substrates for calibration. This position exposed the thermocouple to the same vapour flux and radiative loading as the substrate, but still allowed for substrate rotation. The distance between the source and substrate was 42 cm. The ITO source composed of pure 3–12 mm pieces of In_2O_3:SnO_2 (91:9% mol; 99.99% purity; Cerac, Inc.). No process gas was added during deposition. The films were grown on *p*-type Si (100) wafers (University Wafer), quartz (Quartz Scientific), B270 glass (Howard Glass Co.), and commercial ITO on borofloat glass (Delta Technologies, Ltd). The films were deposited across a range of deposition angles (30° to 90°), pitch values (1 nm nominal to 1000 nm nominal), flux rates (0.05 nm/s nominal to 2 nm/s nominal) and substrate temperatures (80 to 240 °C). We estimate the effective source diameter to be approximately 1 cm. This large source area permits deposition even at a nominal deposition angle of 90°, as the source is not fully occluded by the substrate holder.

A two-stage annealing process, used in previous work in our group [13], was performed on the nanowhisker films deposited on quartz substrates to improve the properties as a transparent conductor. The first-stage anneal was initiated with a ramp rate of 10 °C/min from room temperature to 500 °C in atmosphere then held for 90 min. The samples were removed after passively cooling to 90 °C. Sample transmissivity increased after this first stage, but conductivity was typically decreased. The second-stage anneal was performed in a 3 inch outer diameter three-zone tube furnace. Forming gas consisting of 5% H_2/balance Ar was flowed over the samples at a rate of 100 sccm during anneal. The samples were ramped linearly to 375 °C in 90 min, held at 375 °C for 60 min and then allowed to passively cool to

below 90 °C before removal. In-plane resistance was typically decreased after the second anneal stage with little change to the transmissivity.

5.2.2 Film Characterization

A scanning electron microscope (SEM, Hitachi S-4800) was used to image the films (15 kV accelerating voltage). Films deposited on Si substrates were imaged without further coating, whereas films deposited on quartz, B270 glass, or commercial ITO on borofloat glass were coated with approximately 10 nm Cr to reduce charging. Trunk diameter, droplet diameter, branch diameter, trunk density, and nearest-neighbour distance were measured by analysing cross-sectional and plan view SEM images of uncoated ITO nanowhiskers on Si substrates. Length and diameter values were averaged over five measurements using ImageJ image analysis software [229]. Nearest-neighbour distance was estimated as the mean of a Gaussian distribution fit to the distances between all unique trunk pairs for each image. X-ray diffraction (XRD, Bruker D8 Discover) patterns were taken on the films deposited on Si substrates using Cu K_α radiation, a 0.5 mm collimator and a Bruker HiStar area detector at a distance of 15 cm. Transmission electron microscopy (TEM) was used to image selected ITO nanowhiskers, and to further analyse the crystal structure (JEOL 2200 FS and Hitachi H9500). Transmission spectra of the films on quartz substrates were taken for the range $185 < \lambda < 3300$ nm using a spectrophotometer (Perkin–Elmer NIR–UV). Film sheet resistance (quartz substrate) was measured using a 4-point probe. Transmission and sheet resistance measurements were conducted before and after each annealing stage. Film performance as a transparent conductor was determined by Haacke's figure of merit (ϕ_{TC}) as defined in Equation 1.1, where R_s is sheet resistance and T_{vis} is optical transparency (averaged over 400 nm $< \lambda <$ 780 nm) [93]. Typical device grade planar

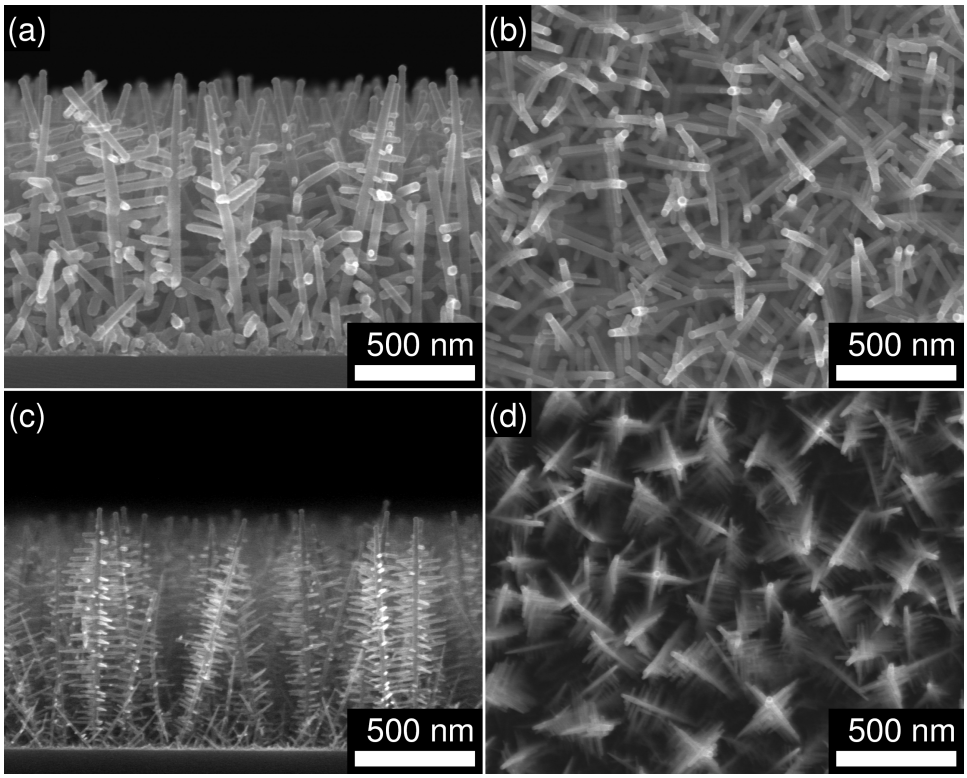

Figure 5.3. *Scanning electron microscopy images of branched ITO nanowire networks deposited by VLS-GLAD with T = 240 °C, R = 0.2 nm/s, pitch = 10 nm nominal and different deposition angles of (a), (b) α = 50° and (c), (d) α = 85°. Images from [190] copyright © 2012 IOP Publishing.*

ITO films have $2 \times 10^{-3}\ \Omega^{-1} < \phi_{TC} < 22 \times 10^{-3}\ \Omega^{-1}$.

5.3 Results & Discussion

5.3.1 Nanowhisker Morphology

Cross-sectional and top-down SEM images of VLS-GLAD ITO nanowhisker films deposited with an increasing deposition angle (α) are shown in Figure 5.3. At elevated α, larger droplets may starve smaller droplets of flux via an increase in geometric shadowing, leading to a decreased subset of droplets

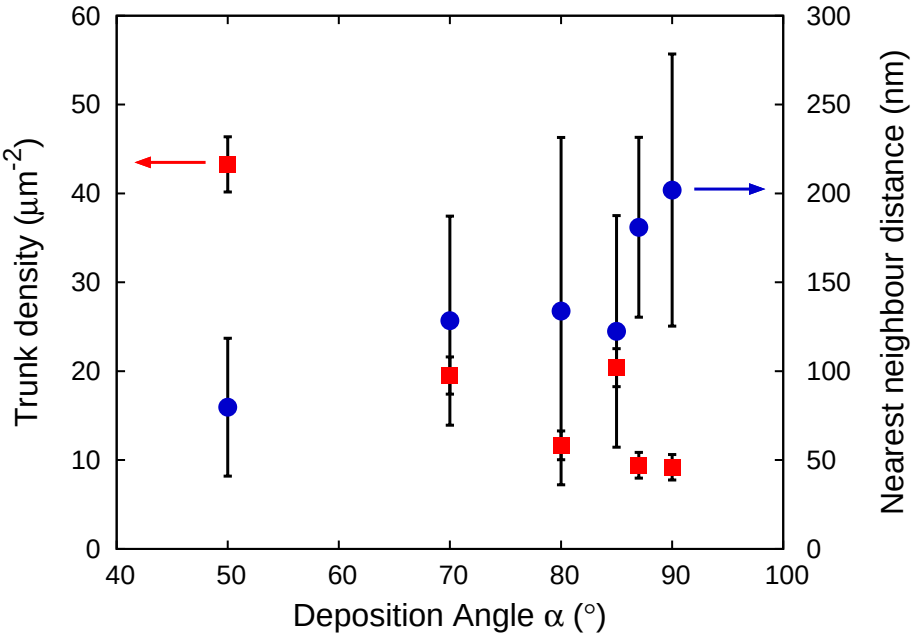

Figure 5.4. *Measured trunk density per unit area and nearest-neighbour distance for branched ITO nanowire networks across a range of deposition angles. Error bars indicate standard deviation (nearest-neighbour distance) or propagated counting error (trunk density). Data from [190].*

producing trunks. Increasing deposition angle results in the growth of fewer nanowhiskers over the same substrate area, consistent with the competitive growth model used to describe the reduced number density of features in GLAD films [20]. This effect is quantified in Figure 5.4 via measurements of trunk number density and nearest neighbour distance, where number density clearly decreases with increasing deposition angle.

The relationship between deposition angle and number of branches and trunk diameter are quantified in Figure 5.5. Interestingly, the trunk diameter also appears to be a function of α, with a sharp decrease in trunk diameter at deposition angles greater than $\alpha = 70^{\circ}$. The number of branches per unit

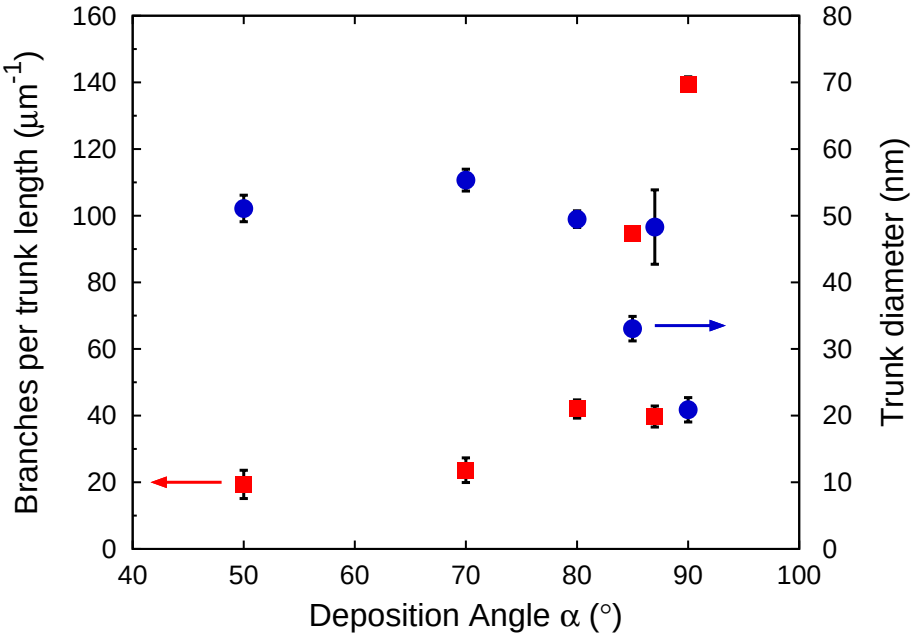

Figure 5.5. *Average branches per unit trunk length and trunk diameter measured for branched ITO nanowire networks for varying deposition angle. Error bars indicate standard deviation (trunk diameter) or propagated counting error (branches per trunk length). Data from [190].*

trunk length increases rapidly with increasing deposition angle. Branch formation seems dependent on the amount of flux incident on the side of the trunk, which is controlled by geometric shadowing from nearby whiskers. With increasing deposition angle, the combination of decreasing trunk diameter and increasing trunk-to-trunk spacing results in decreasing shadowing from neighbouring whiskers. These dominant geometric effects appear to increase flux incident on trunk sides and thus increase branching.

Nominal flux rate has a strong impact on film morphology, as seen in Figure 5.6. For films deposited at large deposition angles, increasing flux rate results in a reduction in the number of branches and an increase in

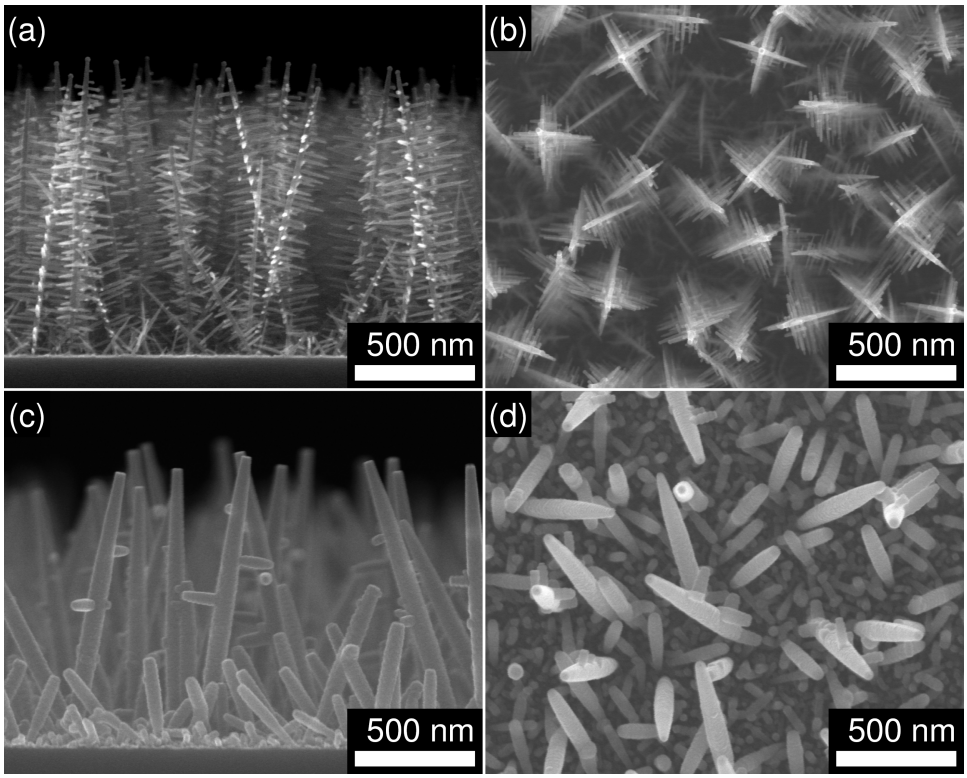

Figure 5.6. *Scanning electron microscopy images of branched ITO nanowire networks deposited by VLS-GLAD with T = 240 °C, α = 85°, pitch = 10 nm nominal different deposition rates of (a), (b) 0.05 nm/s and (c), (d) 2 nm/s. Images from [190] copyright © 2012 IOP Publishing.*

both trunk and branch diameter. Measurements for these parameters are shown in Figure 5.7. Typical VLS growth is described as having two transitions: vapour-to-liquid and liquid-to-solid [28]. Increasing the flux rate will proportionally increase the rate of material crossing the vapour-to-liquid interface. The liquid droplet size will hence increase until the rate of liquid-to-solid transition (related to the area of this interface) has increased as well. The increase in size of the liquid droplets thereby increases trunk diameter. The decrease in branching with increasing rate also appears to be related to geometrical shadowing. As trunk diameter increases with flux rate and

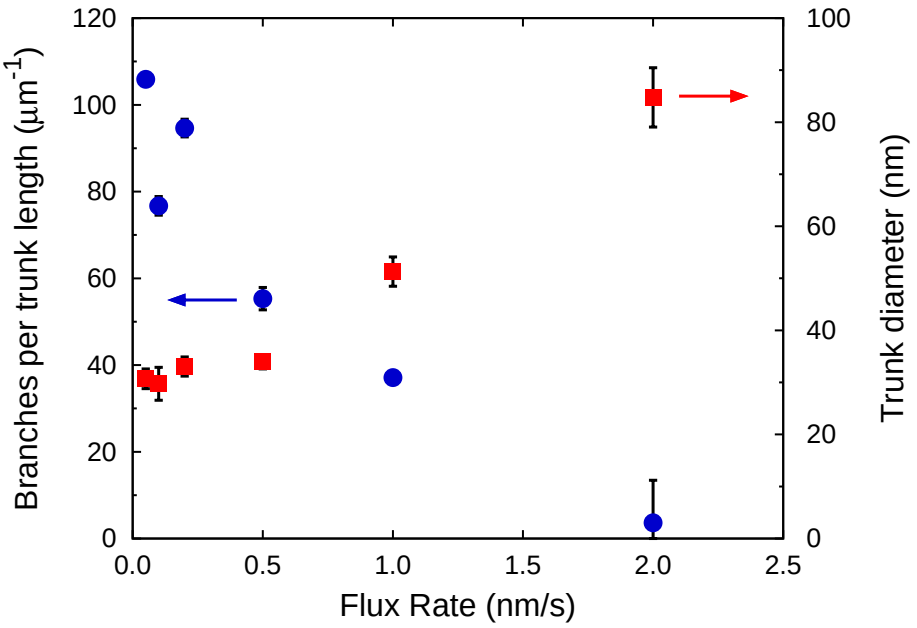

Figure 5.7. *Average number of branches per unit trunk length and trunk diameter measured for branched ITO nanowires grown at α = 85° and varying flux rate. Error bars indicate standard deviation (trunk diameter) or propagated counting error (branches per trunk length). Data from [190].*

trunk-to-trunk spacing remains relatively constant, the trunk sides are increasingly shadowed from incoming flux. This decrease in flux incident on the trunk sides leads to branching decreasing to nearly zero in the largest flux rate case.

For all VLS-GLAD films grown across a large range of temperatures, flux rates, deposition angles and rotation rates, the branch diameter seems to be limited to a portion of trunk diameter. This upper bound is located at a fraction of $1/\sqrt{2}$ of the trunk diameter, representing the side length of the inscribed square in the trunk's circular cross section (Figure 5.8). The observed geometrical restriction to branch diameter suggests the branches

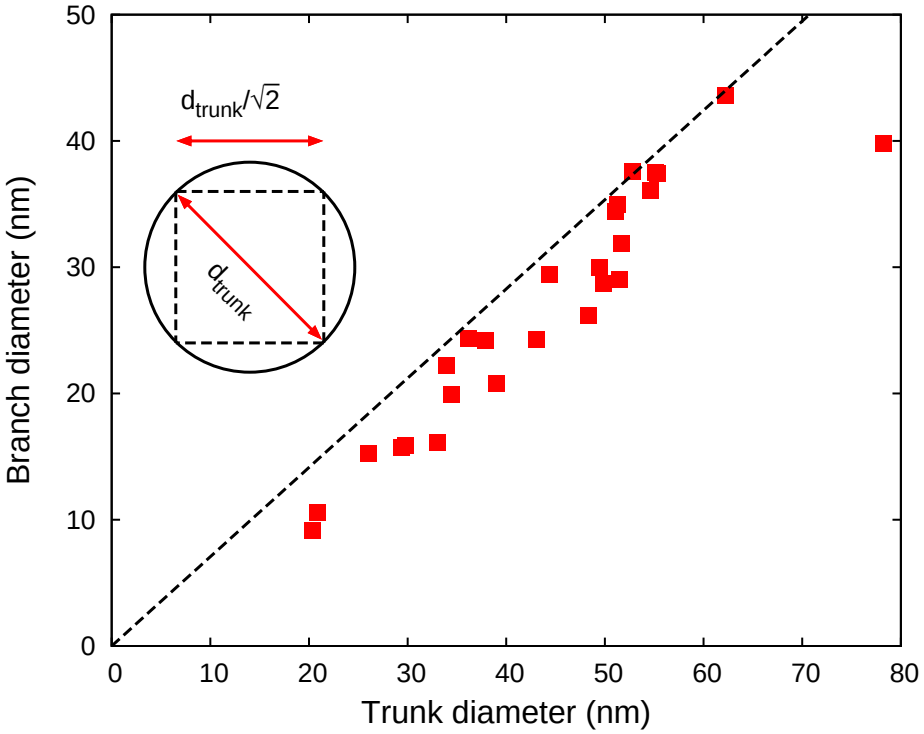

Figure 5.8. *Measured branch diameter as compared to trunk diameter for branched ITO nanowire networks. The dotted line represents the side length of the inscribed square of the trunk's circular cross section, as illustrated in the inset. Data from [190].*

are a continuation of the cubic crystal lattice of the trunk. Therefore, by controlling the initial droplet diameter via the VLS-GLAD mechanism, trunk and branch diameters can be tailored. The control over trunk and branch diameters, as well as the number of branches, is a coupled effect between flux rate and incident angle of vapour flux (α).

Further studies of the effect of temperature on nanowhisker morphology will be necessary in future work. It was observed that pronounced whisker growth becomes increasingly pronounced at temperatures between 130 °C and 165 °C, for deposition angles of 50° and 85°. At a reduced temperature

of 165 °C, VLS growth is noted for lower flux rates. However, at higher flux rates the nanowhiskers begin to appear misshapen or curled. Seemingly without sufficient temperature, the rate of crystallization at the liquid-solid interface cannot increase to match higher flux rates, at which point ballistic growth dominates over kinetic growth.

Pitch (nominal film thickness deposited per substrate rotation) did not appear to have a significant effect on nanowhisker morphology. However, as pitch approaches infinity (no rotation), preferential branch formation in the direction of incident vapour flux was observed as catalytic liquid droplets form favourably on the edge of the nanowhisker facing the vapour flux, resulting in branching towards the incident vapour flux.

5.3.2 Crystal Structure

Crystal structure of the films was analysed with x-ray diffraction. Diffraction patterns for as-deposited samples on Si substrates were taken for all deposition conditions studied. A selection of the diffraction patterns chosen to represent the entire set of data is shown in Figure 5.9. Note that the diffraction peaks in samples "$\alpha = 85°$, T = 100 °C, 0.2 nm/s, 10 nm" and "$\alpha = 50°$, 240 °C, 0.2 nm/s, 10 nm" were textured. Peak positions were measured using EVA (Bruker 15.0.0.0) and used to calculate the Smith and Snyder figure of merit (F_N) [230] for the diffraction patterns for ITO (01-089-4597), In_2O_3 (01-072-0683), SnO (01-072-2324), SnO_2 (01-078-1063), SnO_2 (01-088-0287), Sn (03-065-0297), Sn (03-065-0298) and In (03-065-1172). For the 41 out of 45 samples examined, ITO (01-089-4597) had the largest F_N. The samples with low F_N for ITO exhibit a few discernible ($\leq$3) low-intensity diffraction peaks. Overall these results are consistent with the nanowhisker films composed of crystalline ITO, as expected. Of the patterns that matched ITO, the (222) and (400) peaks were present in nearly all cases, which is consistent

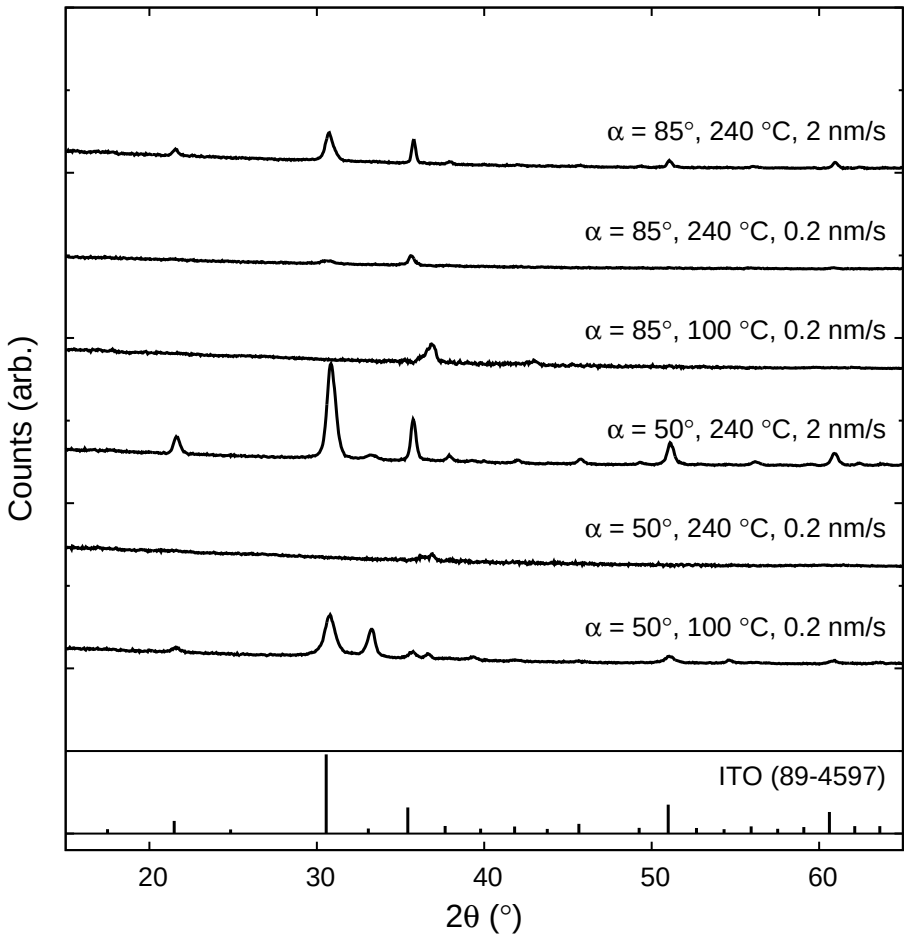

Figure 5.9. *X-ray diffraction patterns of selected samples deposited on Si substrates at a pitch of 10 nm, with variation in deposition angle, substrate temperature, and nominal deposition rate. Reference ITO pattern (PDF 89-4597) is included. Data from [190].*

with previously reported ⟨400⟩ [109,215,216,231] and ⟨222⟩ [40,206] growth directions, along with lattice matched branches occurring orthogonal to the trunk.

The diffraction data was analysed for trends between the deposition conditions and the crystal properties of the films. This included the crystallite size, Smith and Snyder figure of merit, strongest peaks present and per cent crystallinity as measured by a ratio between the integrated intensity of the raw line profile and background substrate profile. We did not observe any conclusive trends in these metrics with the deposition conditions including analysis of deposition angle, pitch, nominal flux rate, flux impingement rate on the substrate and temperature. Any apparent trends in Figure 5.9 do not hold across the entire set of samples. In contrast, smooth trends were observed between morphology and deposition conditions as shown in Figures 5.4, 5.5, and 5.7. This suggests that film crystallinity and morphology are determined by independent processes.

Transmission electron microscopy (TEM) was performed to further analyse crystal structure. Figure 5.10(a) shows a TEM image of a representative ITO nanowhisker. Selected-area electron diffraction (SAED) (Figure 5.10(a) inset) confirmed that the ITO nanowhiskers were single crystals. Figure 5.10(b) shows a high-resolution TEM (HRTEM) image of a branch-trunk interface. Aligned crystal lattice planes were observed, with the planes continuing from the trunk into the branch. This supports the geometrical data in Figure 5.8, further suggesting that the branches grow as part of the same crystal lattice as the trunk.

5.3.3 Optical & Electrical Properties

Transmission spectra and sheet resistance were measured and used to calculate Haacke's figure of merit (ϕ_{TC}) (Equation 1.1) for all of the films pre-

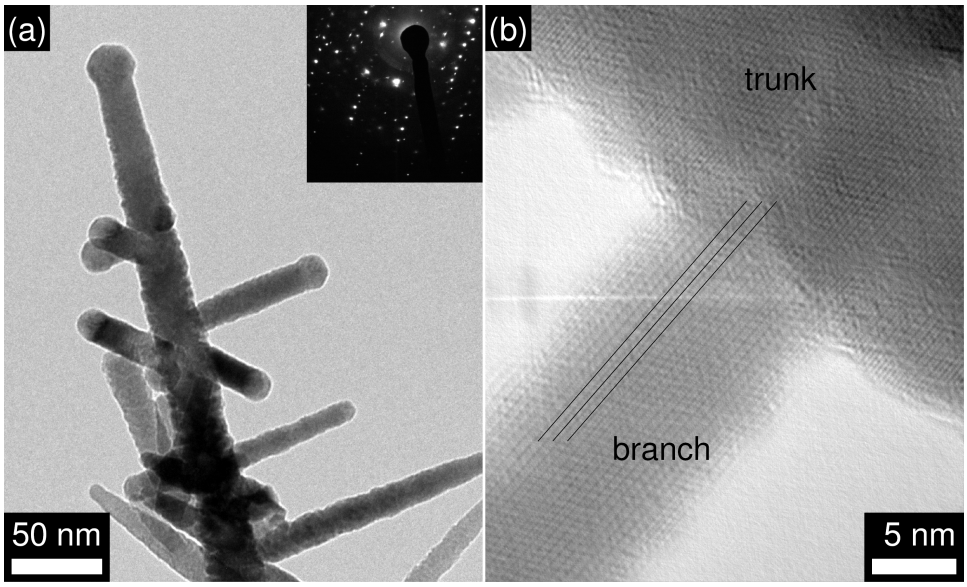

Figure 5.10. *Transmission electron microscopy images of (a) branched ITO nanowire (SAED data inset), and (b) high-resolution image at a trunk–branch interface. Nanowire film deposited via VLS-GLAD with α = 85°, T = 240 °C, R = 0.1 nm/s and pitch = 10 nm nominal. Images from [190] copyright © 2012 IOP Publishing.*

sented to determine their feasibility as a transparent electrode. The first anneal increased the transmission of the films and the second anneal decreased the sheet resistance of the films, collectively improving their Haacke's figure of merit by 1–2 orders of magnitude. The Haacke figure of merit of the films decreases with increasing α (Figure 5.11), as the films move from highly connected networks to separated structures. The best ϕ_{TC} was observed for a hybrid structure (described in the next section) with a base network layer deposited at α = 30°. The film has a sheet resistance of 81.2 $\Omega/\square$ and an average transmission of 90.8%, which results in a ϕ_{TC} of $4.7 \times 10^{-3}\ \Omega^{-1}$.

Having demonstrated the high performance of VLS-GLAD ITO films, we explored the flexibility of our system for different transparent conductor applications. We were able to determine the advantages of various morphologies of nanowhiskers for such applications, and design hybrid nanos-

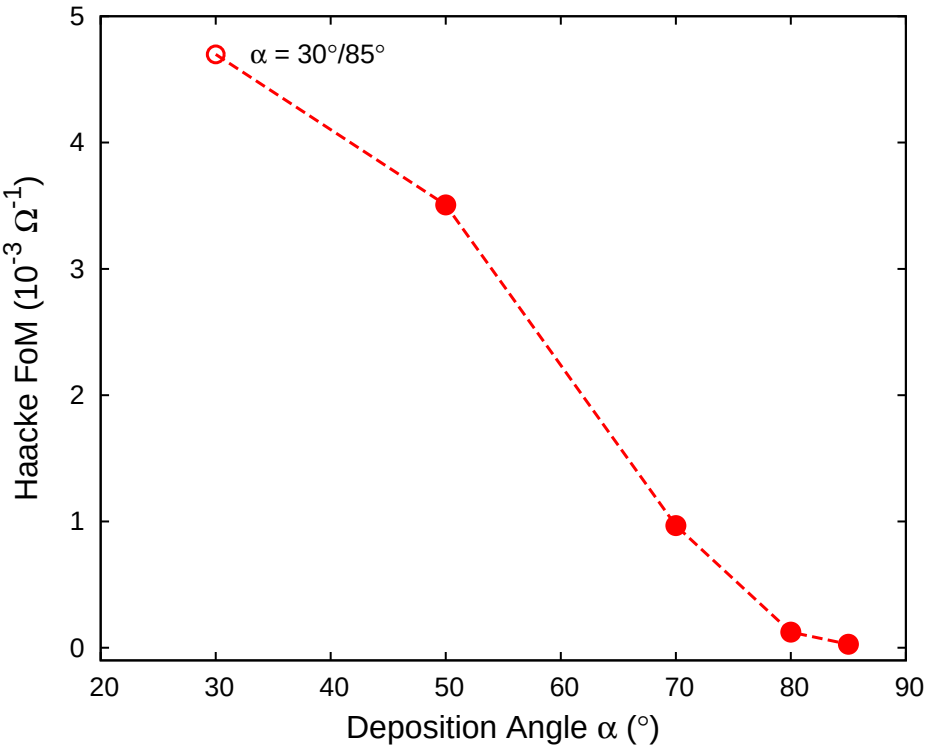

Figure 5.11. *Haacke transparent conductor figure of merit for VLS-GLAD nanowire networks after a two-stage anneal for a range of deposition angles. The deposition angle modulated film from Figure 5.12(e)–(f), "α = 30°/85°", is included to the show the highest figure of merit attained. Data from [190].*

tructures using VLS-GLAD to fabricate ideal three-dimensional transparent conductive films. Films deposited at large deposition angles have a large interfacial area and good electrical access into an active layer. However, use of this morphology depends on using a conductive substrate to provide a common electrode at the base. Dense, interconnected films deposited at small deposition angles have a high ϕ_{TC}, but do provide good electrical access to the active layer. A combination of these morphology's advantages is attainable by VLS-GLAD modulation during growth, described in section 5.3.4.

5.3.4 Hybrid Morphology Nanostructures

Modulating the flux rate and deposition angle during growth via VLS-GLAD allows for the precise fabrication of unusual hybrid nanowhisker structures. These hybrid morphology architectures will provide improved control over the optical and electrical properties of the films. Examples of flux rate modulation and deposition angle modulation are shown in Figure 5.12. Modulation of the flux rate (Figures 5.12(a)-(d)) can be used to adjust the trunk diameter and branch density during growth. In Figure 5.12(a) the trunk diameter responds to the flux rate by contracting from (54 ± 4) nm to (23 ± 1) nm as the flux rate is modulated from 1 to 0.05 nm/s. Similarly, in Figure 5.12(c) the trunk diameter responds to the flux rate by contracting from (53 ± 6) nm to (27 ± 2) nm and then expanding back to (56 ± 3) nm as the flux rate is modulated from 1 to 0.05 nm/s and back to 1 nm/s. The branch diameter and density also respond to the modulation of flux rate. Branching density increases with decreasing flux rate, resulting in a morphology resembling a lobstick tree in Figure 5.12(a), and a trunk with branches only near the centre of the trunk in Figure 5.12(c). In Figures 5.12(e)–(f) the effect of modulating the deposition angle can be seen, where a highly interconnected network of nanowhiskers grown at $\alpha = 30^\circ$ is transformed back into a nanowhisker forest morphology at $\alpha = 85^\circ$. The control provided by VLS-GLAD allows morphologies and functional properties to be hybridized, providing the possibility to optimize the nanowhisker properties for a variety of applications.

The film in Figure 5.12(e) is a good candidate for OPV electrodes as the interconnected base of the film serves as a common electrode and the nanowhisker forest serves to penetrate the device active layer. The nanowire network had the best measured transparent conducting properties of the films shown here, a vast improvement over a film of nanowhiskers deposited at

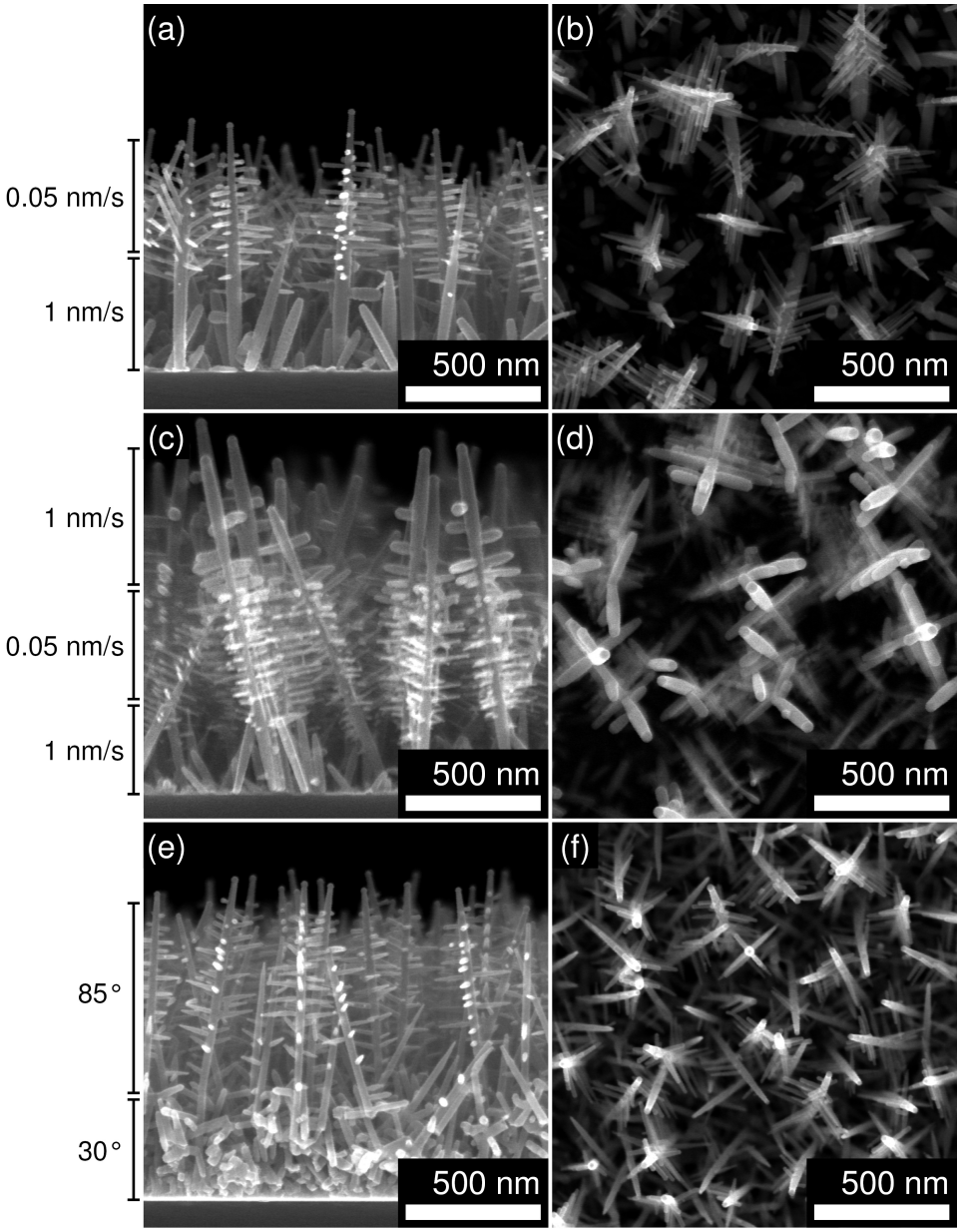

Figure 5.12. *Cross-sectional and plan view scanning electron microscopy images of branched ITO nanowire networks grown by VLS-GLAD with (a), (b) high deposition angle (85°) and flux rate switching from 1 to 0.05 nm/s; (c), (d) high deposition angle (85°) and flux rate switching between 1 nm/s, 0.05 nm/s, and 1 nm/s; and (e), (f) deposition angle switching from $\alpha = 30°$ to $\alpha = 85°$ during deposition. Images from [190] copyright © 2012 IOP Publishing.*

high α (85°), which are open-circuits without an underlying conductive layer. Therefore, real-time VLS-GLAD modulation provides the ability to tailor nanowhisker films for OPV applications. Optimizing the nanowhisker morphologies for three-dimensional transparent conductor applications using VLS-GLAD modulation will be thoroughly investigated in future research.

5.4 Conclusions

Control over self-catalyzed VLS grown ITO nanowhisker morphology has been demonstrated using GLAD. The effects of deposition angle, flux rate, substrate temperature and pitch on ITO nanowhisker morphology have been studied and quantified. VLS-GLAD modulated films allow for the combination of various nanowhisker morphologies, including networks of protruding high surface area ITO nanowhiskers connected via continuous underlayers of ITO, ideal for three-dimensional transparent conductor applications. Advanced control over nanowhisker structure provided by VLS-GLAD should allow for optimization of morphological, optical and electrical properties. The VLS-GLAD technique allows the effects of various deposition parameters to be decoupled, which should improve our fundamental understanding of nanostructured film architectures.

In addition to simple morphology control, several unique morphological features have been observed and appear to be specific to the VLS-GLAD growth method. One of these observed features is periodic diameter oscillation – or "rippling" – observed on branches and which is studied in depth in the following chapter.

6

Flux Engineering for Rippled Nanowire Branches

A version of this chapter has been published:

R.T. Tucker, A.L. Beaudry, J.M. LaForge, M.T. Taschuk, and M.J. Brett, "A little ribbing: Flux starvation engineering for rippled indium tin oxide nanotree branches," Applied Physics Letters **101**, *193101 (2012) [224]. The original manuscript was entitled "Ribbed for your pleasure: VLS-GLAD controlled rippled branch morphology on ITO nanowhiskers".*

6.1 Introduction

This chapter builds on the development of the VLS-GLAD process, which is presented in detail in Chapter 5. The branch diameter oscillations presented herein are caused by a mechanism unique to VLS-GLAD and can be explained and exploited.

The vapour-liquid-solid (VLS) mechanism, whereby growth proceeds by precipitation from a liquid catalyst that concentrates the surrounding vapour, has been used to grow crystalline whiskers [26]. Branched nanowires (or nanotrees) can be formed by placing catalytic droplets on the sides

of nanowires during growth via a stochastic or engineered process, enabling bottom-up fabrication of complex three-dimensional architectures [232,233]. Control over intra-wire morphology has also been investigated, with several groups reporting variations in nanowire diameters [234–245]. Givargizov and others suggest an unstable model of self-oscillations based on droplet contact angle and surface roughness driven by droplet supersaturation [234–236,244]. Most of these reports attribute rippled (or bamboo) nanowire structures to this self-oscillatory growth mode [235–238,243,244]. However, others have demonstrated discontinuous diameter changes through annealing-driven catalyst migration [242], switching between different crystal cross-sections during growth [245], and segmented nanowire morphologies controlled by carrier gas pulsing [239].

Recently, a geometrical modification of VLS growth through glancing angle deposition (GLAD) was developed [190,223,246]. For the self-catalyzed indium tin oxide (ITO) system [40,200,201,247] this technique (VLS-GLAD) provides a higher degree of control over nanowhisker diameter, spacing, and branching behavior, as demonstrated in Chapter 5. Two key features distinguish VLS-GLAD: (i) a collimated (low divergence) flux which breaks flux symmetry at the growth surface, enabling geometrical shadowing effects to mediate the nanowhisker growth and (ii) three-dimensional substrate motion to control the direction of impinging flux during growth. Continuous rotation about substrate normal modulates the incident flux on the branches as they pass through the trunk's shadow. In response, the branch diameter oscillates during growth producing a rippled surface. Unlike the self-oscillatory mechanism, surface ripples produced by flux shadowing are controllable through engineering of substrate motion during growth. Here, we present our observations of branch surface rippling, derive a model linking branch growth physics to experimentally accessible variables in the

VLS-GLAD technique, and verify the explanation by inducing aperiodic ripples into growing branches. As changes in incident flux drive change in the diameter, this model captures diameter control modulated by both motion-controlled shadowing and flux rate. The VLS-GLAD technique provides an opportunity to study VLS growth kinetics, and produces nanostructures that have been previously unachievable.

6.2 Experimental Methods

The VLS-GLAD ITO nanowhisker growth process is fully described in Chapter 5. Briefly, samples were grown in a high vacuum system ($<$0.1 mPa) with dynamic control of the angle between vapour flux source and substrate normal (α) and rotation about substrate normal (φ) (see Figure 6.1). Branched nanowire networks were grown on *p*-type Si (100) substrates (University Wafer) heated by two 150 W halogen lamps held 10 cm above the substrate. Temperature (T) was measured by a thermocouple held $\sim$1 cm above the substrate. ITO (91:9% mol In_2O_3:SnO_2, 99.99% purity) source material was sublimated by an electron beam, creating a highly collimated flux at the substrate surface held 42 cm away. The flux rate was measured by a quartz crystal monitor (QCM). Films were imaged by scanning electron microscopy (SEM, Hitachi S-4800).

6.3 Growth Model

From mass conservation, droplet diameter is controlled by the vapour flux capture rate and the liquid–solid crystallization rate. Vapour flux capture rate is a function of evaporation conditions, adatom diffusivity, and most importantly for the work presented here, the local shadowing environment a growing nanowire experiences. Unlike typical isobaric VLS-growth systems,

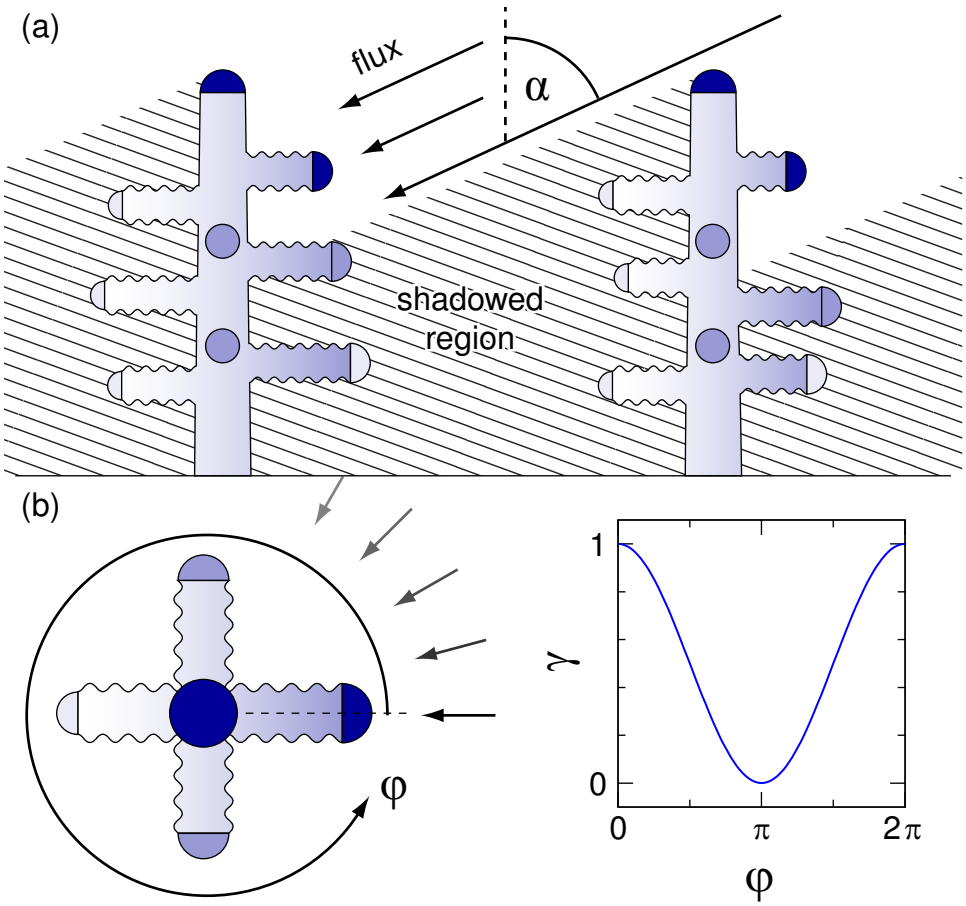

Figure 6.1. *Schematic representation of VLS-GLAD rippling mechanism with (a) cross-sectional view showing glancing angle α and flux shadowing region. Darker droplets are receiving incoming flux and lighter droplets are occluded; (b) plan view shows rotation of substrate by the angle φ, and flux modulation γ at droplet from shadowing by the attached trunk. Images from [224] copyright © 2012 American Institute of Physics.*

the collimated vapour approach used here allows for dynamic control over local vapour pressure. For a growing nanowire array, high deposition angles (α) produce shadows between adjacent nanowires, as shown in Figure 6.1(a). When deposition flux is occluded by upstream nanowire trunks or branches, the liquid Sn-In(-O) droplet is starved of growth material. Vapour under-

supply can lead to droplet decay and subsequently, branch tapering [248]. In some cases, the liquid–solid crystallization process can continue until the droplet is exhausted, resulting in a blunt-ended nanowire [247].

For a constantly rotating substrate, the incoming flux absorbed by a branch droplet oscillates between minimum and maximum values which depend on the local nanowire environment. A droplet on the side of an isolated nanowire will experience periodic shadowing, resulting in periodic growing and shrinking of the droplet. The growing branch's diameter follows droplet diameter, as long as the droplet does not become completely depleted. Figure 6.1(b) shows this rotational effect on flux arriving at a droplet and its periodic nature in an ideal case. The correct conditions produce periodic ripples along the branch growth direction. However, the GLAD process is tunable, and can produce complex shadowing environments, providing a route to enhancing control of VLS growth.

The schematic in Figure 6.2 shows the parameters used in a model relating volume change to both flux rate and rotation rate. Using MATLAB, a single droplet of hemispherical shape was simulated in a finite time domain for varying incoming flux volume. A single branch was assumed to crystallize from the droplet with a length, $L(t)$, at any instant in time, t.

For simplicity, only single branch growth was considered. One type of particle was used, with properties calculated for an average atom in a cubic 91% In_2O_3–9% SnO_2 lattice: mass density $\varrho = 7.18\ \mathrm{g/cm^3}$, molar mass $M = 55.0\ \mathrm{g/mol}$, and monolayer thickness $d = 0.233\ \mathrm{nm}$. All vapour phase atoms within a certain projected area, A, were assumed to condense into the liquid droplet (we expect a high probability of adatom diffusion to the liquid droplet within a certain distance [249]). The rate of incoming volume

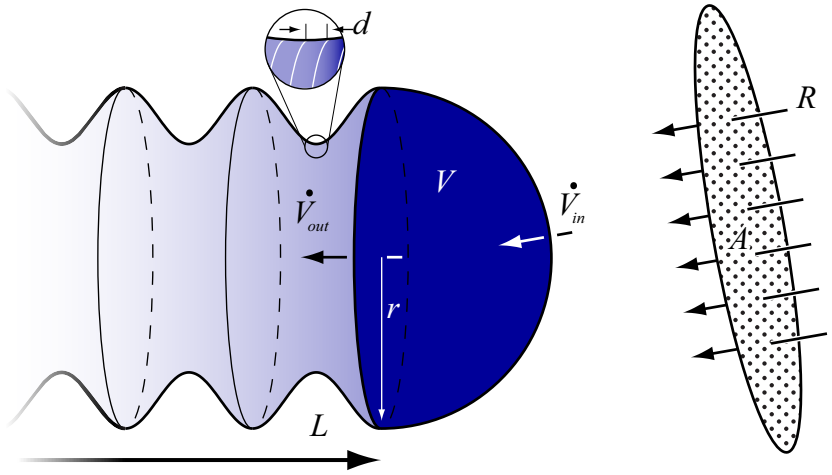

Figure 6.2. *Schematic representation of parameters used in VLS-GLAD branch profile model, including droplet radius (r) and volume (V), branch length (L) and monolayer thickness (d), flux rate (R) and capture area (A), and incoming/outgoing volume rates ($\dot{V}_{\text{in}}/\dot{V}_{\text{out}}$). Images from [224] copyright © 2012 American Institute of Physics.*

to the droplet $\dot{V}_{\text{in}}$ was calculated

$$\dot{V}_{\text{in}}(t) = RA\gamma(t), \tag{6.1}$$

where R is the material flux rate as measured at the QCM in nm/s and γ parameterizes the flux modulation due to rotation-induced shadowing or flux shuttering ($0 \leq \gamma \leq 1$). For continuous rotation,

$$\gamma(t) = \frac{\sin(2\pi t/\tau_{\text{rot}}) + 1}{2}, \tag{6.2}$$

where τ_{rot} is the rotation period in seconds. As neighbouring trunks increase in height, a branch will eventually become completely occluded from the flux. This effect is incorporated as an envelope on $\dot{V}_{\text{in}}$. For this work, we approximate the envelope as an exponential of the form $1 - e^{a(t-t_{\text{max}})}$, where

a is a constant and t_{max} is the time for a certain branch to grow. Detailed studies will be required to elucidate the envelope's functional form.

We assume the branch crystallizes in a layer-by-layer, or birth and spread growth mode [28, 250], with each layer having a circular cross-section of the same radius r as the droplet and monolayer thickness of d. We further assume nucleation time dominates layer crystallization time, such that liquid–solid crystallization time (τ_{LS}) is independent of droplet size and constant for growth of an entire branch. In reality, the growth rate is likely dependent on droplet diameter [251, 252], however, this assumption is tolerable for small changes in droplet diameter. The rate of outgoing volume from the droplet is then

$$\dot{V}_{out}(t) = \frac{d\pi r(t)^2}{\tau_{LS}}, \tag{6.3}$$

where r is the instantaneous radius of the both the droplet and the branch at the liquid–solid crystallization interface. For growth of a branch of length $L_{max} = L(t_{max})$ in time t_{max},

$$\tau_{LS} = \frac{t_{max} d}{L_{max}}. \tag{6.4}$$

Note that this is not valid at extremely slow rotation rates where the droplet becomes extinct. At each time step t_i of length Δt, the instantaneous droplet volume and droplet radius were then calculated

$$V(t_i) = V(t_{i-1}) + \dot{V}_{in}(t_i)\Delta t - \dot{V}_{out}(t_i)\Delta t, \tag{6.5}$$

$$r(t_i) = \sqrt[3]{\frac{3V(t_i)}{2\pi}}. \tag{6.6}$$

As mentioned, branch growth is assumed to occur layer-by-layer, with

the droplet radius directly dictating the branch radius. The radius of branch growth at t_i is then $r(t_i)$, and the corresponding length of grown branch at this instant in time is

$$L(t_i) = L(t_{i-1}) + \frac{d\Delta t}{\tau_{LS}}. \tag{6.7}$$

Therefore, for each time step from $t = t_1$ to $t = t_{\max}$, Equations 6.3 and 6.5–6.7 are calculated, giving rise to a time-dependence of $\dot{V}_{\text{out}}(t)$, $V(t)$, $r(t)$, and $L(t)$.

6.4 Results & Discussion

6.4.1 Periodic Rippling

Representative branched ITO nanowires grown by VLS-GLAD and exhibiting branch ripples are shown in Figure 6.3. The diameter oscillations are observed only on the branches of the nanowires and appear to be quite consistent in amplitude and period along both the height of the trunk and the length of the branch.

Measurements of the distance between diameter oscillations are shown in Figure 6.4. The period of the measured oscillation is consistent between the different measured branches on the same nanowire trunk, with a slight decreasing trend along the length of the branch. This decreasing rippling period is indicative that the layer crystallization time is not truly constant as assumed by the model; however, this assumption significantly simplifies the physics.

6.4.2 Basic Model Results

The simple time domain model can be used to calculate the axial profile of branches grown from arbitrary flux patterns. A constant flux rate is the

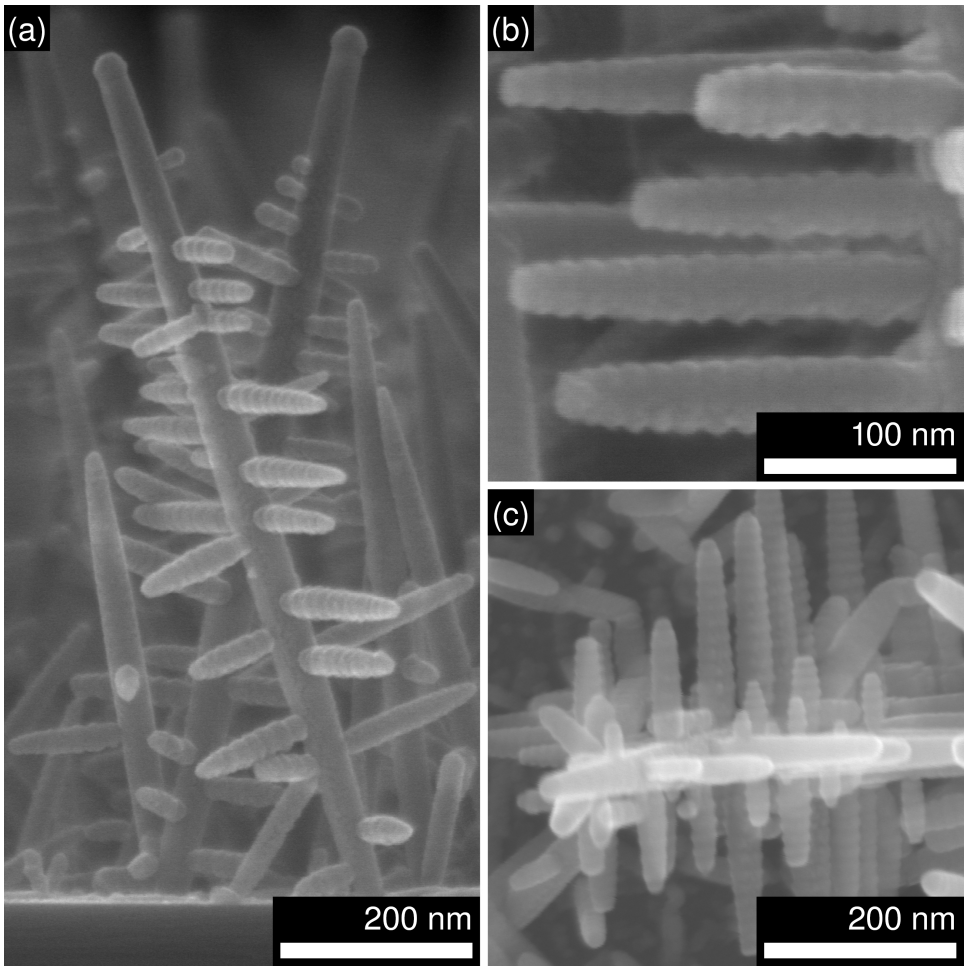

Figure 6.3. *Scanning electron microscopy images of VLS-GLAD branched ITO nanowires with rippled branch features deposited at (a) $\alpha = 87°$, $T = 240$ °C, $R = 2$ Å/s, $\tau_{rot} = 50$ s; (b) magnified cross-section and (c) plan view of $\alpha = 85°$, $T = 240$ °C, $R = 10$ Å/s, $\tau_{rot} = 10$ s. Images from [224] copyright © 2012 American Institute of Physics.*

simplest possible case ($\gamma(t) = 1$) and offers several tests that the model is performing with the expected behavior.

Figure 6.5 presents several modeled branch profiles grown with fixed flux rate model parameters of $A = (70 \times 10^{-9}$ nm$)^2$, t_{max} = 100 s, and τ_{LS} = 0.1 s. The model repeats one of the core relations observed for VLS-GLAD

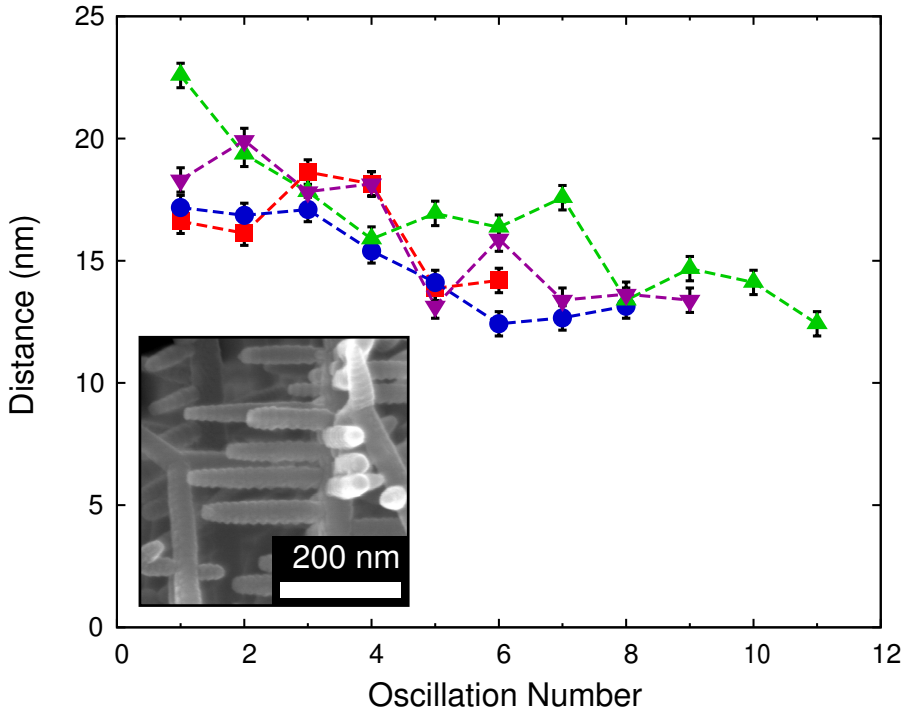

Figure 6.4. *Measured distance between rippling periods for four different branches of a VLS-GLAD ITO nanotree. Inset shows scanning electron microscopy image of measured branches.*

in Chapter 5, namely the increase of nanowire diameter with increasing flux rate. Branch radius saturates to a size dependent on the flux rate, regardless of the initial droplet size if the growth time is long enough. For an initial droplet radius of r_0 = 20 nm, the branch either decreases in radius during growth at a low rate (R = 0.1 nm/s) or increases in radius during growth at a higher rate (R = 2 nm/s) as shown in Figure 6.5(a). Conversely, branches modeled at the same flux rate (R = 0.5 nm/s) at different initial radius conditions (Figure 6.5(b)) saturate to the same branch radius.

As mentioned in Section 6.3, an exponential envelope was incorporated into the incoming volume rate function in order to account for the end of

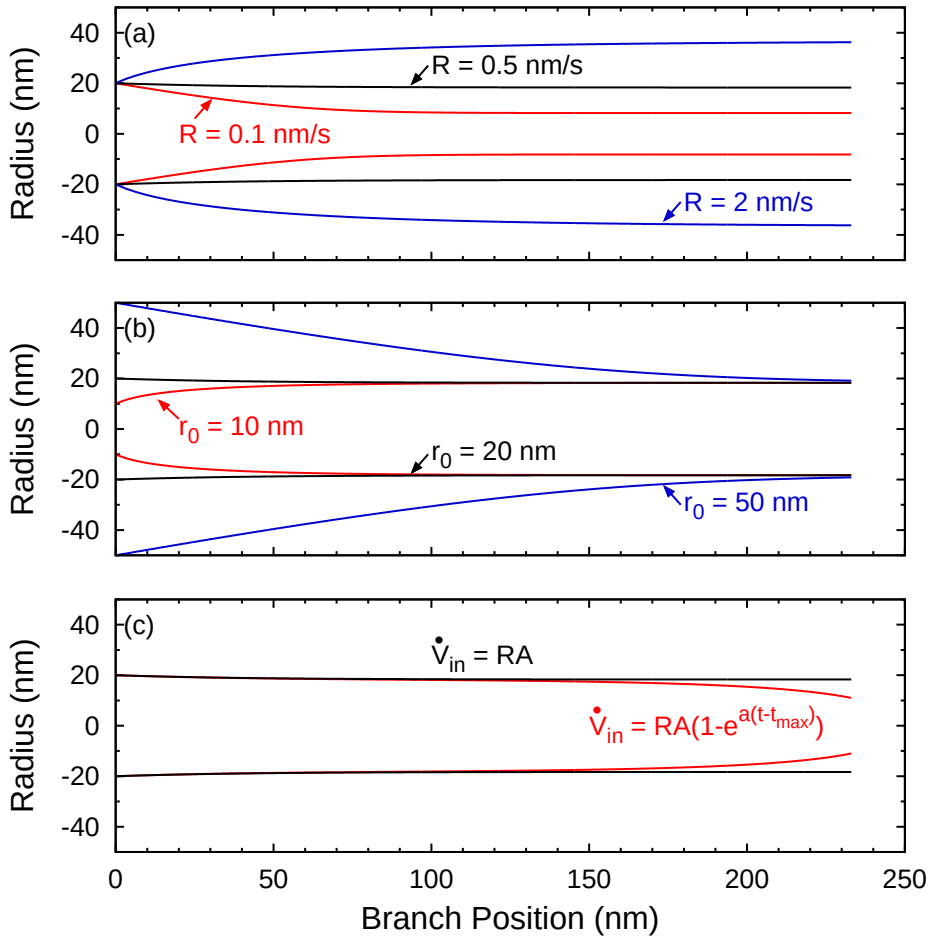

Figure 6.5. *Branch profiles calculated from the time-domain model with constant flux rate for $A = (70 \times 10^{-9}\ nm)^2$, $t_{max} = 100$ s, $\tau_{LS} = 0.1$ s, and (a) fixed initial droplet radius of $r_0 = 20$ nm and $R = 0.1$, 0.5, or 2 nm/s; (b) fixed flux rate of $R = 0.5$ nm/s and $r_0 = 10$, 20, or 50 nm; (c) $R = 0.5$ nm/s, $r_0 = 20$ nm, and the input volume function with or without an exponentially decaying envelope.*

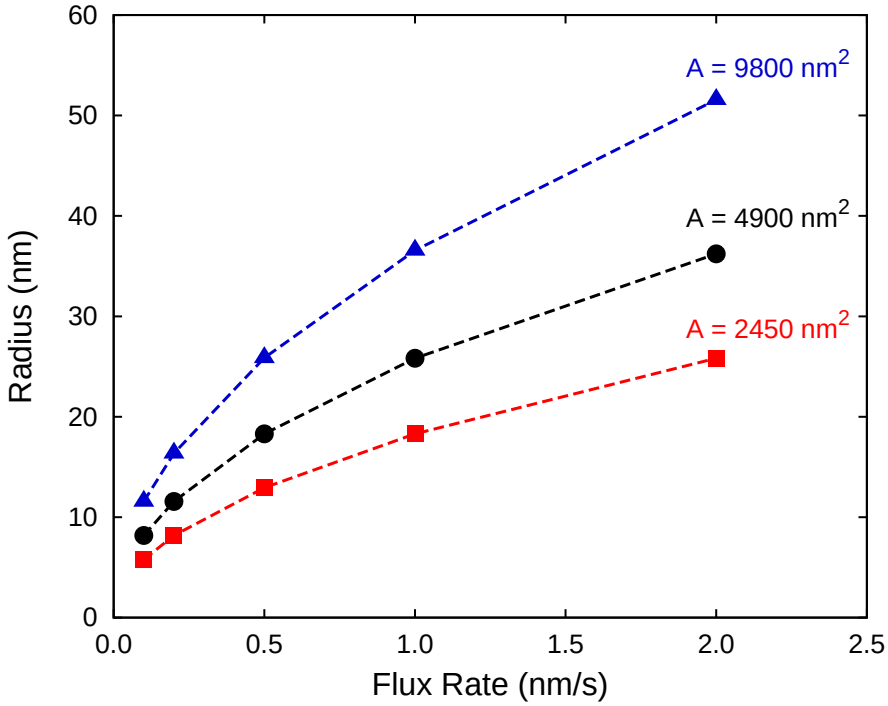

Figure 6.6. *Steady-state branch radius extracted from modeled branch profiles for different flux rates (R) and flux capture areas (A).*

branch growth by complete flux shadowing from neighbouring structures. Figure 6.5(c) shows the modeled branch radius profile at $R = 0.5$ nm/s and $r_0 = 20$ nm both without the envelope function, and with an envelope function of $a = 0.05$. As was hypothesized, the exponential decay of the incoming flux function leads to tapering at the end of the branch, which is consistent with observed branch features. The morphology of any droplet still present at the end of growth, and growth after flux has stopped, is not accounted for with this treatment.

Flux rate-specific branch radius can be extracted from the model as the radius at L_{max} in cases where the growth had reached steady-state conditions. Steady-state branch radius as dependent on flux rate (R) for different flux capture areas (A) is shown in Figure 6.6. Consistent with the trunk di-

ameter data presented in Figure 5.7, the steady-state branch radius increases with flux rate. Furthermore, the radius is equally dependent on the flux capture area in the model. This supports the suggestion that VLS growth is limited at the crystallization step, and that the rate-difference between incident vapour and crystallizing material is responsible for the droplet size and thus nanowire diameter. Furthermore, the flux capture area presents an issue for comparing the model to real-world examples, as the flux capture area for a certain branch is dependent on deposition angle, surface diffusion, re-evaporation, and local shadowing. Since A cannot be easily known for the observed branches, it will be used as a fitting parameter for the modeled branch profiles.

6.4.3 Periodic Rippling Model

Substrate rotation can be included in the model as a periodic oscillation of the incoming volume function. Figure 6.7 shows the model results of a simple periodic rotation (τ_{rot} = 10 s) with an exponential envelope for R = 1 nm/s and t_{max} = 100 s. The oscillating input volume rate is trailed by smaller changes in the outgoing volume rate from the droplet (Figure 6.7(a)). The oscillating droplet radius is transferred to the branch at each instant in growth time, leading to spatial oscillation along the branch's length (Figure 6.7(b)).

To explore the conditions for which these rippling effects can be observed, the same simulation was run with rotation speeds near the high and low end of possible rotation rates. Figure 6.8 shows a simulation of the same parameters, but with $\tau_{\text{rot}} = 1$ s or $\tau_{\text{rot}} = 100$ s. In the case of $\tau_{\text{rot}} = 1$ s, the rippling effect is still present, however, the amplitude of the very closely-spaced ripple features is so small that they are effectively lost. For the case of one order of magnitude increase in rotation time, the length of the rippling

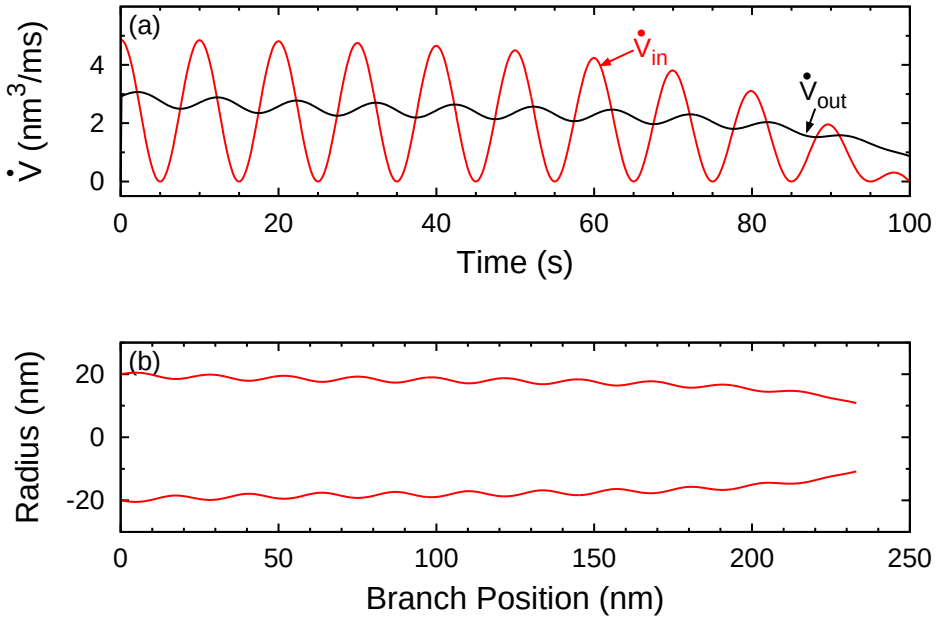

Figure 6.7. *Simulated periodic rippling behavior from constant rotation of flux with R = 1 nm/s and τ_{rot} = 10 s; (a) volume rate in ($\dot{V}_{in}$) and out ($\dot{V}_{out}$) of the droplet; (b) calculated branch radius profile.*

events is on the order of the branch length. The rippling is also effectively lost as a result of the slower rotation times. Diameter oscillations are only observed when the changes in input volume rate occur for long enough for the droplet to lose or gain sufficient material to cause notable changes in growth diameter.

An example case of a branch from Figure 6.3 is used to demonstrate the fit of the model to observed nanowire rippling behavior. A magnified region of the branch is shown in Figure 6.9(a). This particular branch belongs to a film grown with $R = 1$ nm/s and $\tau_{rot} = 10$ s, and is measured to have $L_{max} = 225$ nm with 13 oscillations. Edge detection image processing was used to aid in the quantification of the rippled branch profile with ImageJ software [229], as shown in Figure 6.9(b). Data extracted (also using ImageJ)

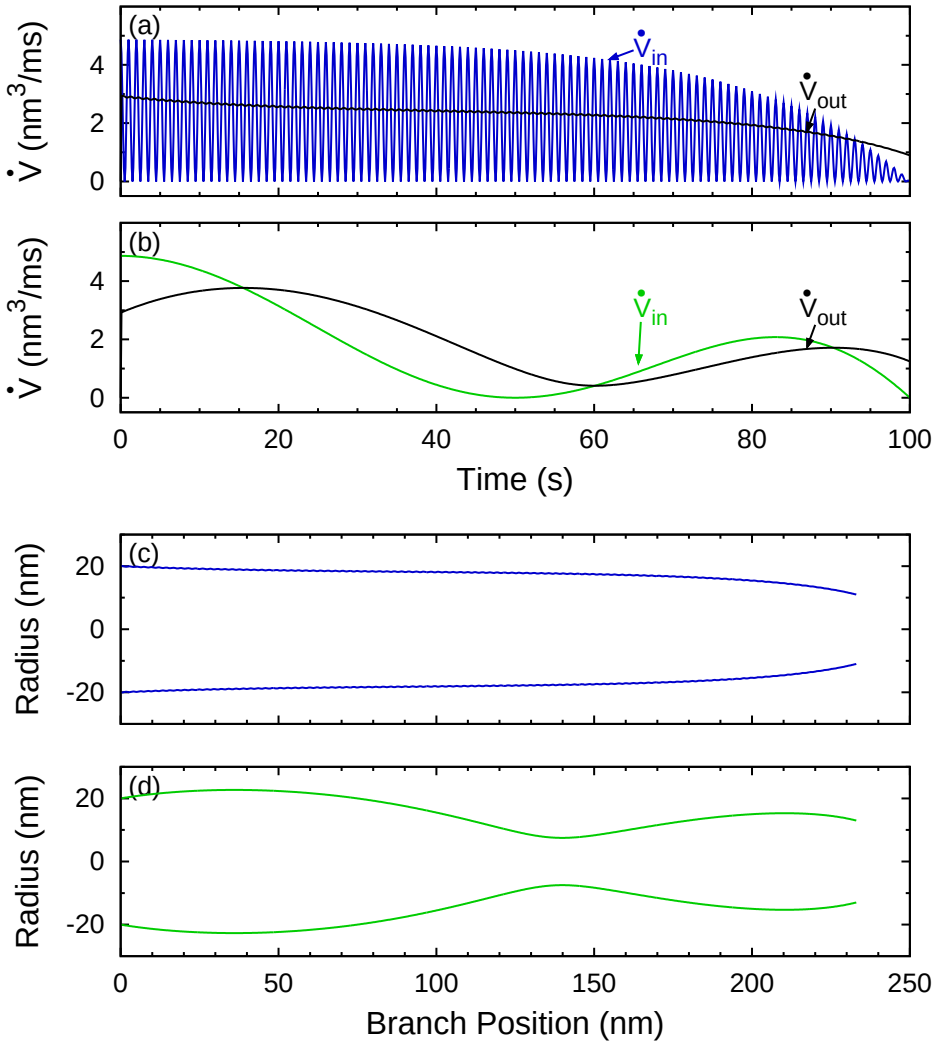

Figure 6.8. *Simulated periodic rippling (a),(b) volume rates and (c),(d) calculated branch radius profiles for R = 1 nm/s and (a),(c) τ_{rot} = 1 s and (b),(d) τ_{rot} = 100 s.*

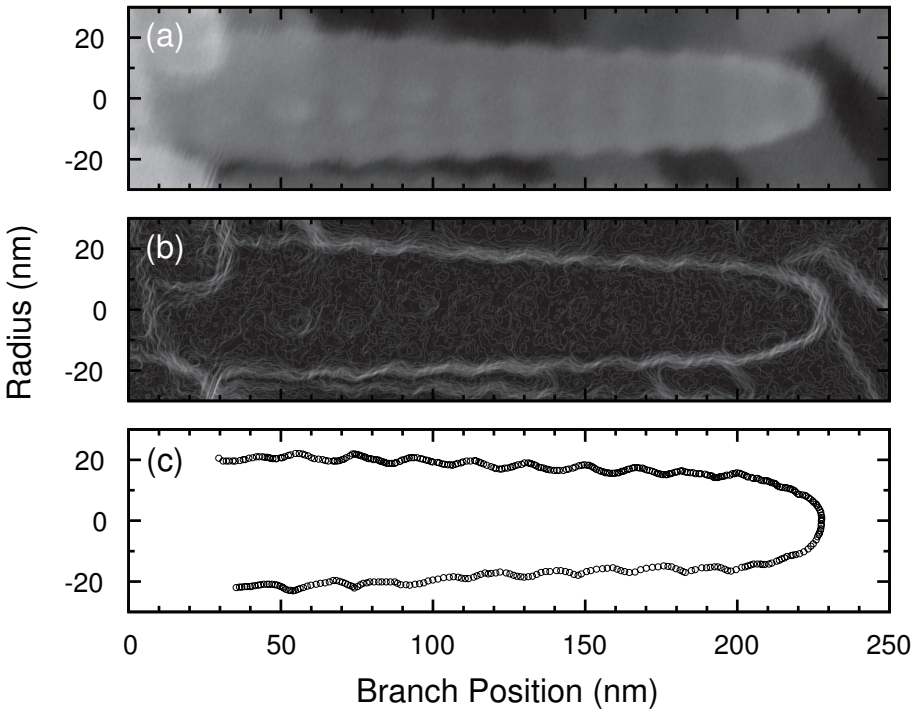

Figure 6.9. *Quantification of rippled ITO nanowire branch by (a) scanning electron microscopy, (b) edge detection, and (c) data extraction. Images from [224] copyright © 2012 American Institute of Physics.*

from image is shown in Figure 6.9(c). Based on the number of nodes and rotation speed, we calculate $t_{\max} = 125$ s, with $\tau_{\mathrm{LS}} = 0.13$ s.

The simulated rippling profile of the example branch from Figure 6.9 compared to the extracted data is shown in Figure 6.10(a). The modeled behavior matches very well with the measured data for constant rotation with $R = 1$ nm/s and $\tau_{\mathrm{rot}} = 10$ s. To obtain this match, the envelope parameter (a) and capture area (A) were varied across a finite range. A good match is achieved for parameters of $a = 0.025$ and $A = 4900\,\mathrm{nm}^2$ (equivalent to a circle with $\sim$39.5 nm radius) in this case. The corresponding time-dependent droplet behavior is shown in Figure 6.10(b)-(d). As was seen in

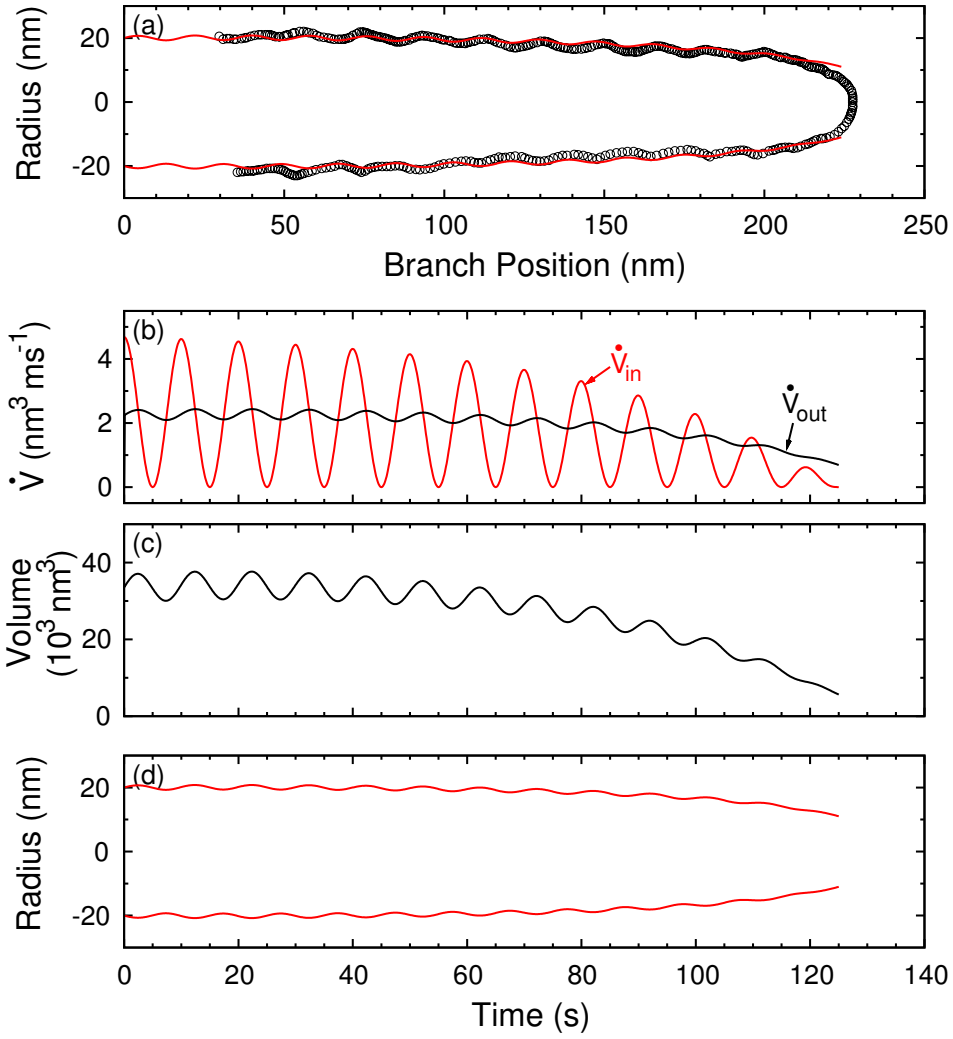

Figure 6.10. *Matched simulated and measured rippled nanowire branch data for R = 1 nm/s and τ_{rot} = 10 s, (a) simulated branch profile for best match parameters compared to extracted data; (b) input volume rate ($\dot{V}_{in}$) to droplet and volume rate out ($\dot{V}_{out}$) of the droplet as calculated in each time-step; (c) droplet volume (V) and (d) droplet radius changing in time. Data from [224].*

the test cases of Figure 6.7, the modeled output volume rate ($\dot{V}_{out}$) follows behind the increase and decrease of the input volume rate ($\dot{V}_{in}$), caused by the increased crystallization volume at larger droplet radii (Figure 6.10(b)). The overall volume oscillation in the droplet is a large fraction of the total droplet volume (Figure 6.10(c)) in order to account for the amplitude of the diameter oscillations (Figure 6.10(d)).

6.4.4 Complex Rippling

To further validate the hypothesis that rippling is a result of flux starvation, more complex structures were grown by two different methods of controlling the incoming flux to the liquid droplet. This was achieved by controlling the local shadowing function (e.g., changing the rotation rate) and by attenuating the vapour flux directly (e.g., rate control or shuttering). The model indicates that both methods should have a similar effect. We have previously shown in Chapter 5 that rate modulation dynamically controls ITO nanowhisker diameter; here we have demonstrated the effect of shuttered flux and the local shadowing environment. ITO nanowhiskers grown with shuttered flux are shown in Figure 6.11.

We use the flux shutter profile shown in Figure 6.11(a), with constant rotation, to produce the ITO nanowhisker shown in Figure 6.11(b). The branch's features follow the shuttering events, controlling ripple amplitude and frequency. Figure 6.11(c) is a magnified image of a characteristic branch. Figures 6.11(d) and 6.11(e) show the approximate shuttering ($\gamma_{shutter}$) and rotational shadowing ($\gamma_{rotation}$) functions, respectively, that match to the window in time when the branch was growing. The total flux modulation function (γ, Figure 6.11(f)) contributing to the growth of the magnified branch results from the combination of the shuttering and rotational shadowing functions.

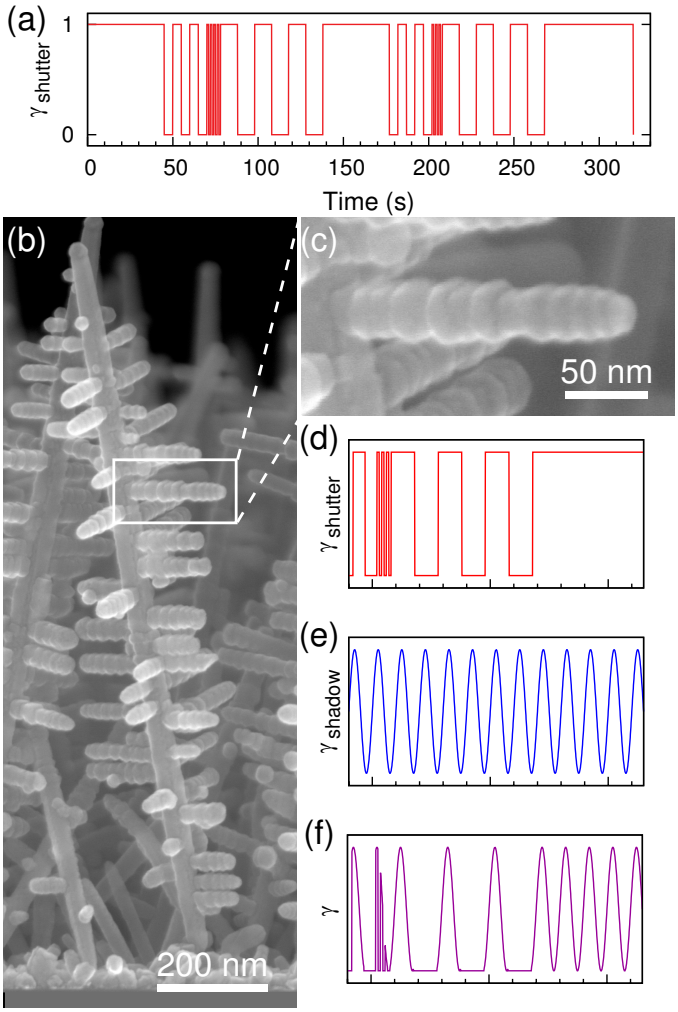

Figure 6.11. *Complex ITO nanowire branch growth by VLS-GLAD with shutter-modulated flux according to the pattern shown in (a), where "1" is shutter open and "0" is shutter closed; (b) SEM image of resulting branched nanowire with unique branching morphology; (c) magnified key branch region, with (d), (e), and (f) displaying the flux modulation due to shuttering, due to rotation-induced shadowing, and the combined shutter-rotation effect on the flux profile, respectively, for the magnified branch. Images from [224] copyright © 2012 American Institute of Physics.*

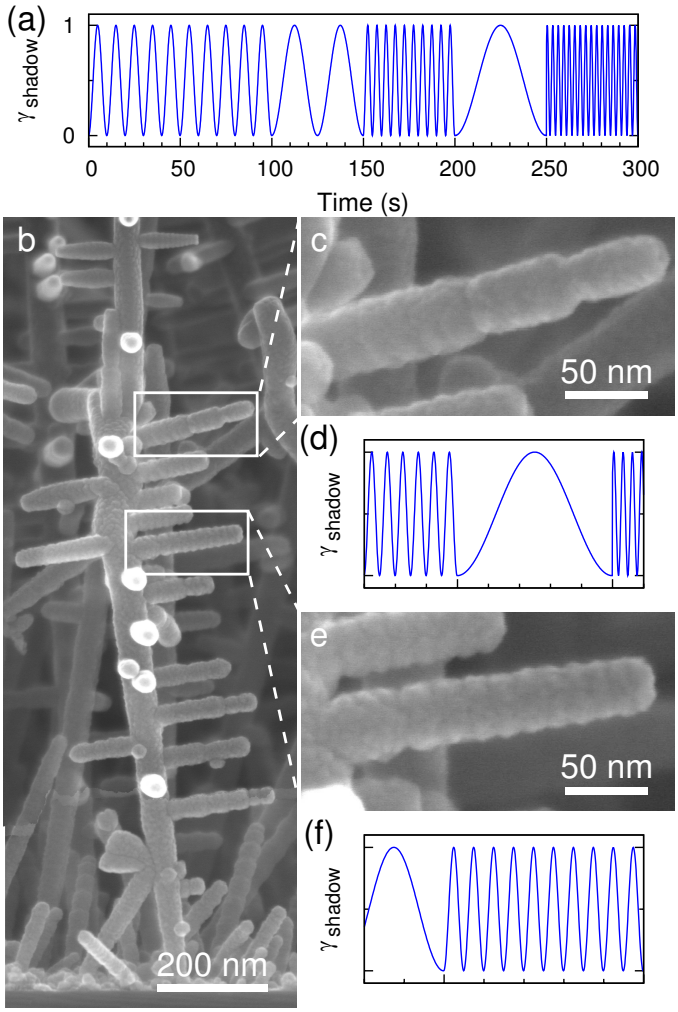

Figure 6.12. *Complex ITO nanowire branch growth by VLS-GLAD with varying rotation rates according to the following program (rotations @ τ_{rot}): 10 @ 10 s, 2 @ 25 s, 10 @ 5 s, 1 @ 50 s, ∼17 @ 3 s, as shown in (a) as the flux attenuation due to rotational shadowing ("1" is flux, "0" is shadowed); (b) SEM image of resulting branched nanowire morphology, and magnified branches (c), (e) along with the approximate sections of rotational shadowing from (a) that contributed to each branch morphology (d), (f), respectively). Images from [224] copyright © 2012 American Institute of Physics.*

Similar controllable diameter modulation effects are shown for variations in rotation rate in Figure 6.12. The flux attenuation profile resulting from local rotation-induced shadowing effects is shown in Figure 6.12(a) from the following rotation scheme: 10 rotations @ $\tau_{rot} = 10$ s, 2 rotations @ $\tau_{rot} = 25$ s, 10 rotations @ $\tau_{rot} = 5$ s, 1 rotation @ $\tau_{rot} = 50$ s, $\sim$17 rotations @ $\tau_{rot} = 3$ s. Figures 6.12(c) and 6.12(e) show magnified images of distinct branches where the effect of rotation-induced flux shadowing can be clearly seen. Figures 6.12(d) and 6.12(f) show different segments in time where the rotational shadowing function (γ_{rotation}) can be matched to each of the magnified branch regions.

In both the shuttering and variable rotation cases, we demonstrate control over the rippling features according to the flux profile. Faster rotation rates result in smaller ripple spacing, and shuttered flux can result in long nodes between ripples. Both the variable rotation and shuttering methods demonstrate (through local shadowing and macroscopically modulated vapour pressure, respectively) direct control over supersaturation in the branch droplets.

6.5 Conclusions

We have demonstrated that flux starvation in VLS-GLAD enables controlled branch diameter modulation during ITO nanotree growth, consistent with a simple volume in/out model. Flux starvation can be induced through shadowing or by adjusting the flux rate directly, both general features of VLS-GLAD. The nanostructures made possible by the VLS-GLAD technique should be available to any material system compatible with branched VLS growth.

Droplet diameter is coupled to nanowire properties such as composition [30, 253], phase [254], and crystallographic growth direction [255, 256].

Thus, modulation of growth diameter with VLS-GLAD may provide a mechanism to modulate these properties during growth as well. Ultimately, surface rippling may prove to be a valuable technique to enhance active surface area, create high energy surface defects, or induce phase changes in the material during growth. This technique also allows for the placement of "time stamps" during growth which may allow for improved investigation of time-related growth kinetics.

This chapter marks the end of the experimental portion of the thesis. The next and final chapter will review the entirety of the work and offer some concluding remarks.

7

Conclusions

The main conclusions from each experimental chapter of the thesis are presented here, followed by recommendations for future work.

7.1 Chapter Summaries

Chapters 2 & 3. The nanostructured niobium oxide films and platinum catalyst supports developed in Chapters 2 & 3 demonstrate the advantage of high surface areas for surface-mediated reactions. The methods used in Chapter 2 show that the combination of GLAD and high temperature annealing in a reactive gas environment can be used to reliably form specific material phases in nanopillar morphology thin films. In this case, amorphous niobium oxide films were reduced in H_2/N_2 or H_2/Ar to oxynitrides or lower oxygen content phases; however, the effects of annealing gas and film porosity should be transferable to other nanopillar metal oxide systems.

The nanopillar-supported platinum electrocatalysts in Chapter 3 are among early demonstrations of the potential for metal oxide nanopillar array supports in the literature. Our study highlights the importance of material composition and phase, in addition to nanoscale structure, on the overall

activity of a composite electrocatalyst. Electrically conductive pathways from the catalyst surface, through either the support only or the combined catalyst–support structure, led to fewer resistive losses and superior overall catalyst activity. The high surface area nanostructured morphology was only seen to enhance performance when combined with a more conductive phase of support.

Chapter 4. Steps toward nanostructuring mixed-material or doped metal oxide thin films via GLAD were explored with the study of electron beam evaporated niobium-doped titanium dioxide thin films in Chapter 4. Composition control was achieved through the use of amorphous sol-gel synthesized Nb-Ti-O pellets as evaporation material, which reduced preferential evaporation effects commonly associated with mixed-material evaporation. After annealing to activate the niobium dopants, the transparent conductive properties were shown to be related to the niobium content in the film. Furthermore, nanopillar films were deposited via GLAD using the same sol-gel pellet method as a demonstration of nanostructured mixed-composition materials.

Chapters 5 & 6. The opportunity for kinetic growth systems for the fabrication of nanostructures was advanced in Chapters 5 & 6. Specifically, the impact of vapour flux directionality and geometry on the self-catalyzed vapour-liquid-solid growth system of indium tin oxide was thoroughly explored with the newly developed VLS-GLAD technique. Flux geometry was shown to significantly affect the average size, shape, and spacing of randomly seeded arrays of branched nanowires. At high deposition angles, deposition rate was used to further control morphology such that hybrid morphology types could be stacked along the height of a growing nanowire.

In Chapter 6, the unique “branch rippling” effect that was observed in

branched ITO nanowires grown by VLS-GLAD was studied in detail. A simple mass balance, time-domain model was constructed which supported the proposed flux starvation mechanism for the formation of the branch diameter oscillations. The model was capable of repeating several aspects of VLS-GLAD growth and good fits against experimental data were observed. Flux starvation was then exploited to encode specific ripple patterns into ITO nanowire branches by programming modulations into the incident vapour flux. This method offers unprecedented control over diameter along the length of a nanowire branch.

7.2 Recommendations

Significant work still exists before nanostructured electrodes are widely adopted into energy conversion device architectures.

For the fuel cell catalyst supports developed in this work, future experiments should focus on alternative support materials, catalyst distribution, and durability testing. The electrical conductivity of NbO_2 has been overstated in many reports and its high stability remains largely untested. Similar techniques as utilized here should be used to explore other materials, such as tungsten carbide or doped titanium dioxide, as nanopillar electrocatalyst supports. The platinum catalyst layers used in Chapter 3 could be largely improved, as unoptimized sputtering was used. A more conformal catalyst coating is desirable, so techniques such as high pressure sputtering, atomic layer deposition, or electrochemical deposition should be invoked on nanopillar catalysts for potential performance gains. Alternative synthesis routes (e.g., chemical, lithographic, or kinetic) for fabrication of the nanopillar supports should also be considered in tandem, as they may prove to be more attractive for manufacturing once high quality materials have been defined and demonstrated. Stability and durability continue to

be of high importance, and more detailed studies of nanopillar electrocatalyst longevity are necessary before they can be seriously considered for commercial application.

Carrier concentration modification though doping continues to be desirable for nanostructured materials. While doping in planar and nanopillar thin films was shown to be possible through single-source multi-component evaporation and subsequent annealing, this method appears to be largely limited in the precision of composition control that can be achieved. Other methods for fabricating doped high aspect ratio nanostructures should be considered, such as co-evaporation, ion bombardment, or chemical synthesis. The electrical properties of doped nanostructures should also be further investigated by through-post conductivity measurement of individual structures and ensembles.

The VLS-GLAD technique has demonstrated a significant degree of morphology control in this work, and further publications have already shown the method's inherent nature to promote evolutionary alignment and directed branching morphologies. Further studies have also used simulations to support the proposed evolutionary growth mechanism and epitaxially-matched substrates to align structures and study branch control. The vast majority of VLS-GLAD work has focused on the indium tin oxide system, and future studies should attempt to demonstrate the versatility of VLS-GLAD in other materials (e.g., gold-catalyzed germanium or silicon). Many VLS material systems (e.g., III–Vs) tend to be grown through reaction of precursor gases, making many of the principles of VLS-GLAD non-applicable. In such cases, geometrically placed catalyst material could be used for directional branch growth. Geometrically directed flux has shown a number of desirable features for shaping nanostructures, and derivative processes of VLS-GLAD may prove to be highly useful for designing rational branched

nanowire networks for future applications.

7.3 Final Comments

The field of advanced nanotechnology-based materials is continually gaining the interest of both researchers and manufacturers as scientific progress demonstrates the opportunities for such materials. Incremental and breakthrough research will continue to push the boundaries of possibility for man-made materials. The collective impact of the methods developed and understanding gained though the work presented in this thesis offer a step toward widely available nanomaterials-based energy conversion devices.

References

[1] N. A. Owen, O. R. Inderwildi, and D. A. King. "The status of conventional world oil reserves – Hype or cause for concern?" *Energy Policy* **38**, 4743–4749 (2010).

[2] "BP Statistical Review of World Energy". Technical report (2013).

[3] J. K. Hyun, S. Zhang, and L. J. Lauhon. "Nanowire Heterostructures". *Annual Review of Materials Research* **43**, 451–479 (2013).

[4] G. Zheng, F. Patolsky, Y. Cui, W. U. Wang, and C. M. Lieber. "Multiplexed electrical detection of cancer markers with nanowire sensor arrays". *Nature Biotechnology* **23**, 1294–1301 (2005).

[5] X. Chen, C. K. Y. Wong, C. A. Yuan, and G. Zhang. "Nanowire-based gas sensors". *Sensors and Actuators B: Chemical* **177**, 178–195 (2013).

[6] N. A. Beckers, M. T. Taschuk, and M. J. Brett. "Selective room temperature nanostructured thin film alcohol sensor as a virtual sensor array". *Sensors and Actuators B: Chemical* **176**, 1096–1102 (2013).

[7] N. Chen, S. Chen, C. Ouyang, Y. Yu, T. Liu, Y. Li, H. Liu, and L. Yuliang. "Electronic logic gates from three-segment nanowires featuring two p–n heterojunctions". *NPG Asia Materials* **5**, e59 (2013).

[8] D. B. Suyatin, L. Wallman, J. Thelin, C. N. Prinz, H. Jörntell, L. Samuelson, L. Montelius, and J. Schouenborg. "Nanowire-based electrode for acute in vivo neural recordings in the brain". *PLOS One* **8**, e56673 (2013).

[9] H. E. Jeong, I. Kim, P. Karam, H.-J. Choi, and P. Yang. "Bacterial recognition of silicon nanowire arrays". *Nano Letters* **13**, 2864–2869 (2013).

[10] F. Mumm, K. M. Beckwith, S. Bonde, K. L. Martinez, and P. Sikorski. "A transparent nanowire-based cell impalement device suitable for detailed cell-nanowire interaction studies." *Small* **9**, 263–272 (2013).

[11] A. Kumar, R. Srivastava, M. N. Kamalasanan, and D. Mehta. "Enhancement of light extraction efficiency of organic light emitting diodes using nanostructured indium tin oxide". *Optics Letters* **37**, 575–577 (2012).

[12] E. C. Garnett, M. L. Brongersma, Y. Cui, and M. D. McGehee. "Nanowire Solar Cells". *Annual Review of Materials Research* **41**, 269–295 (2011).

[13] D. A. Rider, R. T. Tucker, B. J. Worfolk, K. M. Krause, A. Lalany, M. J. Brett, J. M. Buriak, and K. D. Harris. "Indium tin oxide nanopillar electrodes in polymer/fullerene solar cells". *Nanotechnology* **22**, 085706 (2011).

[14] R. Kapadia, Z. Fan, K. Takei, and A. Javey. "Nanopillar photovoltaics: Materials, processes, and devices". *Nano Energy* **1**, 132–144 (2012).

[15] M. K. Debe, A. K. Schmoeckel, G. D. Vernstrom, and R. Atanasoski. "High voltage stability of nanostructured thin film catalysts for PEM fuel cells". *Journal of Power Sources* **161**, 1002–1011 (2006).

[16] H. M. Chen, C. K. Chen, R.-S. Liu, L. Zhang, J. Zhang, and D. P. Wilkinson. "Nano-architecture and material designs for water splitting photoelectrodes". *Chemical Society Reviews* **41**, 5654–5671 (2012).

[17] C. Liu, J. Tang, H. M. Chen, B. Liu, and P. Yang. "A fully integrated nanosystem of semiconductor nanowires for direct solar water splitting". *Nano Letters* **13**, 2989–2992 (2013).

[18] K. Robbie and M. J. Brett. "Sculptured thin films and glancing angle deposition: Growth mechanics and applications". *Journal of Vacuum Science & Technology A: Vacuum, Surfaces, and Films* **15**, 1460–1465 (1997).

[19] M. M. Hawkeye and M. J. Brett. "Glancing angle deposition: Fabrication, properties, and applications of micro- and nanostructured thin films". *Journal of Vacuum Science & Technology A: Vacuum, Surfaces, and Films* **25**, 1317–1335 (2007).

[20] M. T. Taschuk, M. M. Hawkeye, and M. J. Brett. "Glancing Angle Deposition". In "Handbook of Deposition Technologies for Films and Coatings", , edited by P. M. Martin, chapter 13, pp. 621–678. William Andrew Publishing, Boston, 3rd edition (2010).

[21] K. M. Krause, M. T. Taschuk, K. D. Harris, D. A. Rider, N. G. Wakefield, J. C. Sit, J. M. Buriak, M. Thommes, and M. J. Brett. "Surface area characterization of obliquely deposited metal oxide nanostructured thin films". *Langmuir* **26**, 4368–4376 (2010).

[22] K. M. Krause, M. Thommes, and M. J. Brett. "Pore analysis of obliquely deposited nanostructures by krypton gas adsorption at 87 K". *Microporous and Mesoporous Materials* **143**, 166–173 (2011).

[23] K. M. Krause, D. W. Vick, M. Malac, and M. J. Brett. "Taking a Little off the Top: Nanorod Array Morphology and Growth Studied by Focused Ion Beam Tomography". *Langmuir* **26**, 17558–17567 (2010).

[24] J. K. Kwan and J. C. Sit. "The use of ion-milling to control clustering of nanostructured, columnar thin films." *Nanotechnology* **21**, 295301 (2010).

[25] R. T. Tucker, M. D. Fleischauer, R. M. Shewchuk, A. E. Schoeller, and M. J. Brett. "Phase formation and morphology control of niobium oxide nanopillars". *Materials Science and Engineering: B* **176**, 626–632 (2011).

[26] R. S. Wagner and W. C. Ellis. "Vapor-liquid-solid mechanism of single crystal growth". *Applied Physics Letters* **4**, 89–90 (1964).

[27] E. I. Givargizov. "Fundamental aspects of VLS growth". *Journal of Crystal Growth* **31**, 20–30 (1975).

[28] B. A. Wacaser, K. A. Dick, J. Johansson, M. T. Borgström, K. Deppert, and L. Samuelson. "Preferential Interface Nucleation: An Expansion of the VLS Growth Mechanism for Nanowires". *Advanced Materials* **21**, 153–165 (2009).

[29] T. I. Kamins, X. Li, and R. S. Williams. "Growth and structure of chemically vapor deposited Ge nanowires on Si substrates". *Nano Letters* **4**, 503–506 (2004).

[30] X. Zhang, K.-K. Lew, P. Nimmatoori, J. M. Redwing, and E. C. Dickey. "Diameter-dependent composition of vapor-liquid-solid grown $Si_{1-x}Ge_x$ nanowires". *Nano Letters* **7**, 3241–3245 (2007).

[31] K. A. Dick. "A review of nanowire growth promoted by alloys and non-alloying elements with emphasis on Au-assisted III–V nanowires". *Progress in Crystal Growth and Characterization of Materials* **54**, 138–173 (2008).

[32] S. Assali, I. Zardo, S. Plissard, D. Kriegner, M. A. Verheijen, G. Bauer, A. Meijerink, A. Belabbes, F. Bechstedt, J. E. M. Haverkort, and E. P. A. M. Bakkers. "Direct band gap wurtzite gallium phosphide nanowires". *Nano Letters* **13**, 1559–1563 (2013).

[33] J. Wang, S. Plissard, M. Hocevar, T. T. T. Vu, T. Zehender, G. G. W. Immink, M. A. Verheijen, J. E. M. Haverkort, and E. P. A. M. Bakkers. "Position-controlled [100] InP nanowire arrays". *Applied Physics Letters* **100**, 053107 (2012).

[34] S. R. Plissard, I. van Weperen, D. Car, M. A. Verheijen, G. W. G. Immink, J. Kammhuber, L. J. Cornelissen, D. B. Szombati, A. Geresdi, S. M. Frolov, L. P. Kouwenhoven, and E. P. A. M. Bakkers. "Formation and electronic properties of InSb nanocrosses". *Nature Nanotechnology* **8**, 859–864 (2013).

[35] W.-C. Chang, C.-H. Kuo, P.-J. Lee, Y.-L. Chueh, and S.-J. Lin. "Synthesis of single crystal Sn-doped In_2O_3 nanowires: size-dependent conductive characteristics". *Physical Chemistry Chemical Physics* **14**, 13041–13045 (2012).

[36] P. Yang, H. Yan, S. Mao, R. Russo, J. Johnson, R. Saykally, N. Morris, J. Pham, R. He, and H.-J. Choi. "Controlled Growth of ZnO Nanowires and Their Optical Properties". *Advanced Functional Materials* **12**, 323–331 (2002).

[37] R. R. Kumar, K. N. Rao, and A. R. Phani. "Growth of silicon nanowires by electron beam evaporation using indium catalyst". *Materials Letters* **66**, 110–112 (2012).

[38] L. Yu, B. O'Donnell, J.-L. Maurice, and P. Roca i Cabarrocas. "Core-shell structure and unique faceting of Sn-catalyzed silicon nanowires". *Applied Physics Letters* **97**, 023107 (2010).

[39] G. Zhang, S. Sasaki, K. Tateno, H. Gotoh, and T. Sogawa. "Au-free InAs nanowires grown in In-particle-assisted vapor-liquid-solid mode: growth, structure, and electrical property". *AIP Advances* **3**, 052107 (2013).

[40] S. Takaki, Y. Aoshima, and R. Satoh. "Growth Mechanism of Indium Tin Oxide Whiskers Prepared by Sputtering". *Japanese Journal of Applied Physics* **46**, 3537–3544 (2007).

[41] A. Goetzberger, C. Hebling, and H. W. Schock. "Photovoltaic materials, history, status and outlook". *Materials Science & Engineering: R* **40**, 1–46 (2003).

[42] D. M. Bagnall and M. Boreland. "Photovoltaic technologies". *Energy Policy* **36**, 4390–4396 (2008).

[43] A. Shah, P. Torres, R. Tscharner, N. Wyrsch, and H. Keppner. "Photovoltaic Technology: The Case for Thin-Film Solar Cells". *Science* **285**, 692–698 (1999).

[44] J. Britt and C. Ferekides. "Thin-film CdS/CdTe solar cell with 15.8% efficiency". *Applied Physics Letters* **62**, 2851 (1993).

[45] A. Morales-Acevedo. "Thin film CdS/CdTe solar cells: Research perspectives". *Solar Energy* **80**, 675–681 (2006).

[46] F. Kessler and D. Rudmann. "Technological aspects of flexible CIGS solar cells and modules". *Solar Energy* **77**, 685–695 (2004).

[47] I. Repins, M. A. Contreras, B. Egaas, C. DeHart, J. Scharf, C. L. Perkins, B. To, and R. Noufi. "19.9%-efficient ZnO/CdS/$CuInGaSe_2$ Solar Cell with 81.2% Fill Factor". *Progress in Photovoltaics: Research and Applications* **16**, 235–239 (2008).

[48] C. W. Tang. "Two-layer organic photovoltaic cell". *Applied Physics Letters* **48**, 183–185 (1986).

[49] H. Hoppe and N. S. Sariciftci. "Organic solar cells: An overview". *Journal of Materials Research* **19**, 1924–1945 (2004).

[50] H. Spanggaard and F. C. Krebs. "A brief history of the development of organic and polymeric photovoltaics". *Solar Energy Materials and Solar Cells* **83**, 125–146 (2004).

[51] J. C. Bernede. "Organic photovoltaic cells: History, principle and techniques". *Journal of the Chilean Chemical Society* **53**, 1549–1564 (2008).

[52] K. S. Leschkies, A. G. Jacobs, D. J. Norris, and E. S. Aydil. "Nanowire-quantum-dot solar cells and the influence of nanowire length on the charge collection efficiency". *Applied Physics Letters* **95**, 193103 (2009).

[53] E. H. Sargent. "Colloidal quantum dot solar cells". *Nature Photonics* **6**, 133–135 (2012).

[54] H. Hoppe and N. S. Sariciftci. "Polymer Solar Cells". *Advanced Polymer Science* **214**, 1–86 (2008).

[55] G. Yu, J. Gao, J. C. Hummelen, F. Wudl, and A. J. Heeger. "Polymer Photovoltaic Cells: Enhanced Efficiencies via a Network of Internal Donor-Acceptor Heterojunctions". *Science* **270**, 1789–1791 (1995).

[56] M. A. Green, K. Emery, Y. Hishikawa, and W. Warta. "Solar cell efficiency tables (version 35)". *Progress in Photovoltaics: Research and Applications* **18**, 144–150 (2010).

[57] M. A. Green, K. Emery, Y. Hishikawa, W. Warta, and E. D. Dunlop. "Solar cell efficiency tables (version 43)". *Progress in Photovoltaics: Research and Applications* **22**, 1–9 (2014).

[58] J.-H. Wee. "Applications of proton exchange membrane fuel cell systems". *Renewable and Sustainable Energy Reviews* **11**, 1720–1738 (2007).

[59] F. T. Wagner, B. Lakshmanan, and M. F. Mathias. "Electrochemistry and the Future of the Automobile". *The Journal of Physical Chemistry Letters* **1**, 2204–2219 (2010).

[60] H. A. Gasteiger, S. S. Kocha, B. Sompalli, and F. T. Wagner. "Activity benchmarks and requirements for Pt, Pt-alloy, and non-Pt oxygen reduction catalysts for PEMFCs". *Applied Catalysis B: Environmental* **56**, 9–35 (2005).

[61] E. B. Easton, A. Bonakdarpour, and J. R. Dahn. "Fe-C-N Oxygen Reduction Catalysts Prepared by Combinatorial Sputter Deposition". *Electrochemical and Solid-State Letters* **9**, A463–A467 (2006).

[62] S. M. Haile. "Fuel cell materials and components". *Acta Materialia* **51**, 5981–6000 (2003).

[63] S. Litster and G. McLean. "PEM fuel cell electrodes". *Journal of Power Sources* **130**, 61–76 (2004).

[64] Y. Shao, G. Yin, Z. Wang, and Y. Gao. "Proton exchange membrane fuel cell from low temperature to high temperature: Material challenges". *Journal of Power Sources* **167**, 235–242 (2007).

[65] W. Schmittinger and A. Vahidi. "A review of the main parameters influencing long-term performance and durability of PEM fuel cells". *Journal of Power Sources* **180**, 1–14 (2008).

[66] V. Mehta and J. S. Cooper. "Review and analysis of PEM fuel cell design and manufacturing". *Journal of Power Sources* **114**, 32–53 (2003).

[67] E. Antolini and E. R. Gonzalez. "Ceramic materials as supports for low-temperature fuel cell catalysts". *Solid State Ionics* **180**, 746–763 (2009).

[68] Y. Shao, J. Liu, Y. Wang, and Y. Lin. "Novel catalyst support materials for PEM fuel cells: current status and future prospects". *Journal of Materials Chemistry* **19**, 46–59 (2009).

[69] J. Wang, G. Yin, Y. Shao, S. Zhang, Z. Wang, and Y. Gao. "Effect of carbon black support corrosion on the durability of Pt/C catalyst". *Journal of Power Sources* **171**, 331–339 (2007).

[70] Y.-J. Wang, D. P. Wilkinson, and J. Zhang. "Noncarbon support materials for polymer electrolyte membrane fuel cell electrocatalysts". *Chemical Reviews* **111**, 7625–7651 (2011).

[71] H. Chhina, S. Campbell, and O. Kesler. "Thermal and electrochemical stability of tungsten carbide catalyst supports". *Journal of Power Sources* **164**, 431–440 (2007).

[72] T. Ioroi, Z. Siroma, N. Fujiwara, S. Yamazaki, and K. Yasuda. "Sub-stoichiometric titanium oxide-supported platinum electrocatalyst for polymer electrolyte fuel cells". *Electrochemistry Communications* **7**, 183–188 (2005).

[73] J. R. Smith, F. C. Walsh, and R. L. Clarke. "Electrodes based on Magneli phase titanium oxides: the properties and applications of Ebonex materials". *Journal of Applied Electrochemistry* **28**, 1021–1033 (1998).

[74] K. Sasaki, L. Zhang, and R. R. Adzic. "Niobium oxide-supported platinum ultra-low amount electrocatalysts for oxygen reduction". *Physical Chemistry Chemical Physics* **10**, 159–167 (2008).

[75] J. Martínez, H. Hansen, J. Rossmeisl, and J. Nø rskov. "Formation energies of rutile metal dioxides using density functional theory". *Physical Review B* **79**, 045120 (2009).

[76] H. Chhina, S. Campbell, and O. Kesler. "Characterization of Nb and W Doped Titania as Catalyst Supports for Proton Exchange Membrane Fuel Cells". *Journal of New Materials for Electrochemical Systems* **12**, 177–185 (2009).

[77] Y. Furubayashi, T. Hitosugi, Y. Yamamoto, K. Inaba, G. Kinoda, Y. Hirose, T. Shimada, and T. Hasegawa. "A transparent metal: Nb-doped anatase TiO_2". *Applied Physics Letters* **86**, 252101 (2005).

[78] H. Chhina, S. Campbell, and O. Kesler. "Ex Situ and In Situ Stability of Platinum Supported on Niobium-Doped Titania for PEMFCs". *Journal of The Electrochemical Society* **156**, B1232–B1237 (2009).

[79] M. K. Debe and A. R. Drube. "Structural characteristics of a uniquely nanostructured organic thin film". *Journal of Vacuum Science & Technology B: Microelectronics and Nanometer Structures* **13**, 1236–1241 (1995).

[80] A. Bonakdarpour, K. Stevens, G. D. Vernstrom, R. Atanasoski, A. K. Schmoeckel, M. K. Debe, and J. R. Dahn. "Oxygen reduction activity

of Pt and PtMnCo electrocatalysts sputtered on nano-structured thin film support". *Electrochimica Acta* **53**, 688–694 (2007).

[81] Y. Liu, J. M. Szeifert, J. M. Feckl, B. Mandlmeier, J. Rathousky, O. Hayden, D. Fattakhova-Rohlfing, and T. Bein. "Niobium-doped titania nanoparticles: synthesis and assembly into mesoporous films and electrical conductivity". *ACS Nano* **4**, 5373–5381 (2010).

[82] M. K. Debe, A. J. Steinbach, G. D. Vernstrom, S. M. Hendricks, M. J. Kurkowski, R. T. Atanasoski, P. Kadera, D. A. Stevens, R. J. Sanderson, E. Marvel, and J. R. Dahn. "Extraordinary Oxygen Reduction Activity of Pt_3Ni_7". *Journal of The Electrochemical Society* **158**, B910–B918 (2011).

[83] A. Garsuch, D. A. Stevens, R. J. Sanderson, S. Wang, R. T. Atanasoski, S. Hendricks, M. K. Debe, and J. R. Dahn. "Alternative Catalyst Supports Deposited on Nanostructured Thin Films for Proton Exchange Membrane Fuel Cells". *Journal of The Electrochemical Society* **157**, B187–B194 (2010).

[84] M. D. Gasda, G. A. Eisman, and D. Gall. "Nanorod PEM Fuel Cell Cathodes with Controlled Porosity". *Journal of The Electrochemical Society* **157**, B437–B440 (2010).

[85] N. Rajalakshmi, H. Ryu, M. M. Shaijumon, and S. Ramaprabhu. "Performance of polymer electrolyte membrane fuel cells with carbon nanotubes as oxygen reduction catalyst support material". *Journal of Power Sources* **140**, 250–257 (2005).

[86] W. J. Khudhayer, N. N. Kariuki, X. Wang, D. J. Myers, A. U. Shaikh, and T. Karabacak. "Oxygen Reduction Reaction Electrocatalytic Activity of Glancing Angle Deposited Platinum Nanorod Arrays". *Journal of The Electrochemical Society* **158**, B1029–B1041 (2011).

[87] W. J. Khudhayer, N. Kariuki, D. J. Myers, A. U. Shaikh, and T. Karabacak. "GLAD Cr Nanorods Coated with SAD Pt Thin Film for Oxygen Reduction Reaction". *Journal of The Electrochemical Society* **159**, B729–B736 (2012).

[88] A. Bonakdarpour, M. D. Fleischauer, M. J. Brett, and J. R. Dahn. "Columnar support structures for oxygen reduction electrocatalysts

prepared by glancing angle deposition". *Applied Catalysis A: General* **349**, 110–115 (2008).

[89] S. A. Francis, R. T. Tucker, M. J. Brett, and S. H. Bergens. "Structural and activity comparison of self-limiting versus traditional Pt electrodepositions on nanopillar Ni films". *Journal of Power Sources* **222**, 533–541 (2013).

[90] M. D. Gasda, G. A. Eisman, and D. Gall. "Sputter-Deposited Pt/CrN Nanoparticle PEM Fuel Cell Cathodes: Limited Proton Conductivity Through Electrode Dewetting". *Journal of The Electrochemical Society* **157**, B71–B76 (2010).

[91] K. Chopra, S. Major, and D. K. Pandya. "Transparent conductors: A status review". *Thin Solid Films* **102**, 1–46 (1983).

[92] C. Granqvist and A. Hultaker. "Transparent and conducting ITO films: new developments and applications". *Thin Solid Films* **411**, 1–5 (2002).

[93] G. Haacke. "New figure of merit for transparent conductors". *Journal of Applied Physics* **47**, 4086–4089 (1976).

[94] A. Kumar and C. Zhou. "The race to replace tin-doped indium oxide: Which material will win?" *ACS Nano* **4**, 11–14 (2010).

[95] K. Badeker. "Über die elektrische Leitfähigkeit und die thermoelektrische Kraft einiger Schwermetallverbindungen". *Annalen der Physik* **22**, 749–766 (1907).

[96] M. J. Brett, R. W. McMahon, J. Affinito, and R. R. Parsons. "High rate planar magnetron deposition of transparent, conducting, and heat reflecting films on glass and plastic". *Journal of Vacuum Science & Technology A: Vacuum, Surfaces, and Films* **1**, 352–355 (1983).

[97] R. G. Gordon. "Criteria for choosing transparent conductors". *MRS Bulletin* **25**, 52–57 (2000).

[98] F. M. Amanullah, K. J. Pratap, and V. H. Babu. "Thickness Dependence of Electrical and Structural Properties of FTO Films". *Crystal Research and Technology* **26**, 1099–1105 (1991).

[99] Y.-S. He, J. C. Campbell, R. C. Murphy, M. F. Arendt, and J. S. Swinnea. "Electrical and optical characterization of Sb:SnO_2". *Journal of Materials Research* **8**, 3131–3134 (1993).

[100] T. Minami. "Present status of transparent conducting oxide thin-film development for Indium-Tin-Oxide (ITO) substitutes". *Thin Solid Films* **516**, 5822–5828 (2008).

[101] E. Joanni, R. Savu, M. de Sousa Goes, P. R. Bueno, J. Nei de Freitas, A. F. Nogueira, E. Longo, and J. A. Varela. "Dye-sensitized solar cell architecture based on indium-tin oxide nanowires coated with titanium dioxide". *Scripta Materialia* **57**, 277–280 (2007).

[102] C. Renault, C. P. Andrieux, R. T. Tucker, M. J. Brett, V. Balland, and B. Limoges. "Unraveling the mechanism of catalytic reduction of O_2 by microperoxidase-11 adsorbed within a transparent 3D-nanoporous ITO film". *Journal of the American Chemical Society* **134**, 6834–6845 (2012).

[103] C. Renault, K. D. Harris, M. J. Brett, V. Balland, and B. Limoges. "Time-resolved UV-visible spectroelectrochemistry using transparent 3D-mesoporous nanocrystalline ITO electrodes". *Chemical Communications* **47**, 1863–1865 (2011).

[104] D. Schaming, C. Renault, R. T. Tucker, S. Lau-Truong, J. Aubard, M. J. Brett, V. Balland, and B. Limoges. "Spectroelectrochemical Characterization of Small Hemoproteins Adsorbed within Nanostructured Mesoporous ITO Electrodes". *Langmuir* **28**, 14065–14072 (2012).

[105] P. Yu, C.-H. Chang, M.-S. Su, M.-H. Hsu, and K.-H. Wei. "Embedded indium-tin-oxide nanoelectrodes for efficiency and lifetime enhancement of polymer-based solar cells". *Applied Physics Letters* **96**, 153307 (2010).

[106] F. Iskandar, A. B. Suryamas, M. Kawabe, M. M. Munir, K. Okuyama, T. Tarao, and T. Nishitani. "Indium Tin Oxide Nanofiber Film Electrode for High Performance Dye Sensitized Solar Cells". *Japanese Journal of Applied Physics* **49**, 010213 (2010).

[107] H.-W. Wang, C.-F. Ting, M.-K. Hung, C.-H. Chiou, Y.-L. Liu, Z. Liu, K. R. Ratinac, and S. P. Ringer. "Three-dimensional electrodes for dye-

sensitized solar cells: synthesis of indium-tin-oxide nanowire arrays and ITO/TiO_2 core-shell nanowire arrays by electrophoretic deposition". *Nanotechnology* **20**, 055601 (2009).

[108] G.-Y. Chen, M.-W. Lee, and G.-J. Wang. "Fabrication of Dye-Sensitized Solar Cells with a 3D Nanostructured Electrode". *International Journal of Photoenergy* p. 585621 (2010).

[109] M. K. Fung, Y. C. Sun, A. M. C. A. Ng, A. B. Djurisić, H. T. Chan, and W. K. Chan. "Indium tin oxide nanorod electrodes for polymer photovoltaics". *ACS Applied Materials & Interfaces* **3**, 522–527 (2011).

[110] H. Kwon, J. Ham, D. Y. Kim, S. J. Oh, S. Lee, S. H. Oh, E. F. Schubert, K.-G. Lim, T.-W. Lee, S. Kim, J.-L. Lee, and J. K. Kim. "Three-Dimensional Nanostructured Indium-Tin-Oxide Electrodes for Enhanced Performance of Bulk Heterojunction Organic Solar Cells". *Advanced Energy Materials* p. 1301566 (2014).

[111] H. K. Yu, W. J. Dong, G. H. Jung, and J.-L. Lee. "Three-Dimensional Nanobranched Indium-Tin-Oxide Anode for Organic Solar Cells". *ACS Nano* **5**, 8026–8032 (2011).

[112] H. K. Yu, S. Kim, B. Koo, G. H. Jung, B. Lee, J. Ham, and J.-L. Lee. "Nano-branched transparent conducting oxides: beyond the brittleness limit for flexible electrode applications." *Nanoscale* **3**, 2–5 (2012).

[113] A. I. Hochbaum and P. Yang. "Semiconductor nanowires for energy conversion". *Chemical Reviews* **110**, 527–546 (2010).

[114] Z. W. Pan, Z. R. Dai, and Z. L. Wang. "Nanobelts of semiconducting oxides". *Science* **291**, 1947–1949 (2001).

[115] Y. W. Heo, D. P. Norton, L. C. Tien, Y. Kwon, B. S. Kang, F. Ren, S. J. Pearton, and J. R. Laroche. "ZnO nanowire growth and devices". *Materials Science and Engineering: R* **47**, 1–47 (2004).

[116] D. Bach, R. Schneider, and D. Gerthsen. "EELS of niobium and stoichiometric niobium-oxide phases–Part II: quantification." *Microscopy and Microanalysis* **15**, 524–538 (2009).

[117] D. Adler. "Mechanisms for Metal–Nonmental Transitions in Transition Metal Oxides and Sulfides". *Reviews of Modern Physics* **40**, 714–736 (1968).

[118] B. Reichman and A. J. Bard. "Electrochromism at Niobium Pentoxide Electrodes in Aqueous and Acetonitrile Solutions". *Journal of The Electrochemical Society* **127**, 241–242 (1980).

[119] N. Kurioka, D. Watanabe, M. Haneda, T. Shimanouchi, T. Mizushima, N. Kakuta, A. Ueno, T. Hanaoka, and Y. Sugi. "Preparation of niobium oxide films as a humidity sensor". *Catalysis Today* **16**, 495–501 (1993).

[120] M. E. Gimon-Kinsel and K. J. Balkus. "Pulsed laser deposition of mesoporous niobium oxide thin films and application as chemical sensors". *Microporous and Mesoporous Materials* **28**, 113–123 (1999).

[121] K. Arshak, G. Hickey, J. Harris, and E. Forde. "Ozone Sensing Properties of NbO_2 Thin Films for Health and Safety Applications". *IEEE Sensors Applications Symposium* pp. 187–192 (2008).

[122] J. Xia, N. Masaki, K. Jiang, and S. Yanagida. "Fabrication and characterization of thin Nb_2O_5 blocking layers for ionic liquid-based dye-sensitized solar cells". *Journal of Photochemistry and Photobiology A: Chemistry* **188**, 120–127 (2007).

[123] B. Varghese, S. C. Haur, and C.-T. Lim. "Nb_2O_5 Nanowires as Efficient Electron Field Emitters". *Journal of Physical Chemistry C* **112**, 10008–10012 (2008).

[124] T. Ushikubo. "Recent topics of research and development of catalysis by niobium and tantalum oxides". *Catalysis Today* **57**, 331–338 (2000).

[125] X. Xiao, G. Dong, C. Xu, H. He, H. Qi, Z. Fan, and J. Shao. "Structure and optical properties of Nb_2O_5 sculptured thin films by glancing angle deposition". *Applied Surface Science* **255**, 2192–2195 (2008).

[126] W. Smith, Z.-Y. Zhang, and Y.-P. Zhao. "Structural and optical characterization of WO_3 nanorods/films prepared by oblique angle deposition". *Journal of Vacuum Science & Technology B: Microelectronics and Nanometer Structures* **25**, 1875–1881 (2007).

[127] D. Deniz, D. J. Frankel, and R. J. Lad. "Nanostructured tungsten and tungsten trioxide films prepared by glancing angle deposition". *Thin Solid Films* **518**, 4095–4099 (2010).

[128] J. Thangala, Z. Chen, A. Chin, C.-Z. Ning, and M. K. Sunkara. "Phase Transformation Studies of Metal Oxide Nanowires". *Crystal Growth & Design* **9**, 3177–3182 (2009).

[129] J. Buha, I. Djerdj, M. Antonietti, and M. Niederberger. "Thermal Transformation of Metal Oxide Nanoparticles into Nanocrystalline Metal Nitrides Using Cyanamide and Urea as Nitrogen Source". *Chemistry of Materials* **19**, 3499–3505 (2007).

[130] N. Schönberg. "Some features of the Nb-N and Nb-N-O systems". *Acta Chemica Scandinavia* **8**, 208–212 (1954).

[131] "Physical Constants of Inorganic Compounds in CRC Handbook of Chemistry and Physics". CRC Press/Taylor and Francis, Boca Raton, FL, internet edition (2011).

[132] W. Pies and A. Weiss. "VI.1.5.3.6 Oxidenitrides". In "The Landolt-Bornstein Database", , edited by K. H. Hellwege and A. M. Hellwege, chapter c565. Springer.

[133] A. Bonakdarpour, R. T. Tucker, M. D. Fleischauer, N. A. Beckers, M. J. Brett, and D. P. Wilkinson. "Nanopillar Niobium Oxides as Support Structures for Oxygen Reduction Electrocatalysts". *Electrochimica Acta* **85**, 492–500 (2012).

[134] X. Yu and S. Ye. "Recent advances in activity and durability enhancement of Pt/C catalytic cathode in PEMFC". *Journal of Power Sources* **172**, 145–154 (2007).

[135] J. P. Meyers and R. M. Darling. "Model of Carbon Corrosion in PEM Fuel Cells". *Journal of The Electrochemical Society* **153**, A1432–A1442 (2006).

[136] H. Tang, Z. Qi, M. Ramani, and J. F. Elter. "PEM fuel cell cathode carbon corrosion due to the formation of air/fuel boundary at the anode". *Journal of Power Sources* **158**, 1306–1312 (2006).

[137] Z. Liu, X. Lin, J. Y. Lee, W. Zhang, M. Han, and L. M. Gan. "Preparation and characterization of platinum-based electrocatalysts on multiwalled carbon nanotubes for proton exchange membrane fuel cells". *Langmuir* **18**, 4054–4060 (2002).

[138] A. L. Patterson. "The Scherrer formula for X-ray particle size determination". *Physical Review* **56**, 978–982 (1939).

[139] L. Gancs, T. Kobayashi, M. K. Debe, R. Atanasoski, and A. Wieckowski. "Crystallographic Characteristics of Nanostructured Thin-Film Fuel Cell Electrocatalysts: A HRTEM Study". *Chemistry of Materials* **20**, 2444–2454 (2008).

[140] J. K. Hulm, C. K. Jones, R. A. Hein, and J. W. Gibson. "Superconductivity in the TiO and NbO systems". *Journal of Low Temperature Physics* **7**, 291–307 (1972).

[141] V. H. Schafer, D. Bergner, and R. Gruehn. "The thermodynamic stability of seven phases of O/Nb between 2.00 and 2.50". *Zeitschrift für Anorganische und Allgemeine Chemie* **365**, 31–50 (1969).

[142] L. Zhang, L. Wang, C. M. B. Holt, T. Navessin, K. Malek, M. H. Eikerling, and D. Mitlin. "Oxygen Reduction Reaction Activity and Electrochemical Stability of Thin-Film Bilayer Systems of Platinum on Niobium Oxide". *Journal of Physical Chemistry C* **114**, 16463–16474 (2010).

[143] C. M. Reich, A. Kaiser, and J. T. S. Irvine. "Niobia based rutile materials as SOFC anodes". *Fuel Cells* **1**, 249–255 (2001).

[144] J.-G. Fan, D. Dyer, G. Zhang, and Y.-P. Zhao. "Nanocarpet Effect: Pattern Formation during the Wetting of Vertically Aligned Nanorod Arrays". *Nano Letters* **4**, 2133–2138 (2004).

[145] R. T. Tucker, N. A. Beckers, M. D. Fleischauer, and M. J. Brett. "Electron beam deposited Nb-doped TiO_2 toward nanostructured transparent conductive thin films". *Thin Solid Films* **525**, 28–34 (2012).

[146] D. S. Ginley and C. Bright. "Transparent conducting oxides". *MRS Bulletin* **25**, 15–18 (2000).

[147] T. Ishida, M. Okada, T. Tsuchiya, T. Murakami, and M. Nakano. "Structural and surface property study of sputter deposited transparent conductive Nb-doped titanium oxide films". *Thin Solid Films* **519**, 1934–1942 (2011).

[148] L. Zhao, X. Zhao, J. Liu, A. Zhang, D. Wang, and B. Wei. "Fabrications of Nb-doped TiO_2 (TNO) transparent conductive oxide polycrystalline films on glass substrates by sol-gel method". *Journal of Sol-Gel Science and Technology* **53**, 475–479 (2009).

[149] C. G. Granqvist. "Transparent conductors as solar energy materials: A panoramic review". *Solar Energy Materials and Solar Cells* **91**, 1529–1598 (2007).

[150] N. Yamada, T. Hitosugi, N. Hoang, Y. Furubayashi, Y. Hirose, S. Konuma, T. Shimada, and T. Hasegawa. "Structural, electrical and optical properties of sputter-deposited Nb-doped TiO_2 (TNO) polycrystalline films". *Thin Solid Films* **516**, 5754–5757 (2008).

[151] M. A. Gillispie, M. F. A. M. van Hest, M. S. Dabney, J. D. Perkins, and D. S. Ginley. "rf magnetron sputter deposition of transparent conducting Nb-doped TiO_2 films on $SrTiO_3$". *Journal of Applied Physics* **101**, 033125 (2007).

[152] N. Yamada, T. Hitosugi, J. Kasai, N. L. H. Hoang, S. Nakao, Y. Hirose, T. Shimada, and T. Hasegawa. "Transparent conducting Nb-doped anatase TiO_2 (TNO) thin films sputtered from various oxide targets". *Thin Solid Films* **518**, 3101–3104 (2010).

[153] Y. Furubayashi, T. Hitosugi, Y. Yamamoto, Y. Hirose, G. Kinoda, K. Inaba, T. Shimada, and T. Hasegawa. "Novel transparent conducting oxide: Anatase $Ti_{1-x}Nb_xO_2$". *Thin Solid Films* **496**, 157–159 (2006).

[154] Y. Furubayashi, N. Yamada, Y. Hirose, Y. Yamamoto, M. Otani, T. Hitosugi, T. Shimada, and T. Hasegawa. "Transport properties of d-electron-based transparent conducting oxide: Anatase $Ti_{1-x}Nb_xO_2$". *Journal of Applied Physics* **101**, 093705 (2007).

[155] S. X. Zhang, S. Dhar, W. Yu, H. Xu, S. B. Ogale, and T. Venkatesan. "Growth parameter-property phase diagram for pulsed laser

deposited transparent oxide conductor anatase Nb:TiO_2". *Applied Physics Letters* **91**, 112113 (2007).

[156] S. X. Zhang, D. C. Kundaliya, W. Yu, S. Dhar, S. Y. Young, L. G. Salamanca-Riba, S. B. Ogale, R. D. Vispute, and T. Venkatesan. "Niobium doped TiO_2: Intrinsic transparent metallic anatase versus highly resistive rutile phase". *Journal of Applied Physics* **102**, 013701 (2007).

[157] X. W. Zheng and Z. Q. Li. "Structural and electrical transport properties of Nb-doped TiO_2 films deposited on $LaAlO_3$ by RF sputtering". *Applied Surface Science* **255**, 8104–8109 (2009).

[158] J. Y. Yang, W. S. Li, H. Li, Y. Sun, R. F. Dou, C. M. Xiong, L. He, and J. C. Nie. "Grain size dependence of electrical and optical properties in Nb-doped anatase TiO_2". *Applied Physics Letters* **95**, 213105 (2009).

[159] M. S. Dabney, M. F. A. M. van Hest, C. W. Teplin, S. P. Arenkiel, J. D. Perkins, and D. S. Ginley. "Pulsed laser deposited Nb doped TiO_2 as a transparent conducting oxide". *Thin Solid Films* **516**, 4133–4138 (2008).

[160] M. A. Gillispie, M. F. A. M. van Hest, M. S. Dabney, J. D. Perkins, and D. S. Ginley. "Sputtered Nb- and Ta-doped TiO_2 transparent conducting oxide films on glass". *Journal of Materials Research* **22**, 2832–2837 (2007).

[161] T. Hitosugi, A. Ueda, S. Nakao, N. Yamada, Y. Furubayashi, Y. Hirose, T. Shimada, and T. Hasegawa. "Fabrication of highly conductive $Ti_{1-x}Nb_xO_2$ polycrystalline films on glass substrates via crystallization of amorphous phase grown by pulsed laser deposition". *Applied Physics Letters* **90**, 212106 (2007).

[162] N. Yamada, T. Hitosugi, N. L. H. Hoang, Y. Furubayashi, Y. Hirose, T. Shimada, and T. Hasegawa. "Fabrication of Low Resistivity Nb-doped TiO_2 Transparent Conductive Polycrystalline Films on Glass by Reactive Sputtering". *Japanese Journal of Applied Physics* **46**, 5275–5277 (2007).

[163] N. L. H. Hoang, N. Yamada, T. Hitosugi, J. Kasai, S. Nakao, T. Shimada, and T. Hasegawa. "Low-temperature Fabrication of Transpar-

ent Conducting Anatase Nb-doped TiO_2 Films by Sputtering". *Applied Physics Express* **1**, 115001 (2008).

[164] Y. Sato, H. Akizuki, T. Kamiyama, and Y. Shigesato. "Transparent conductive Nb-doped TiO_2 films deposited by direct-current magnetron sputtering using a TiO_{2-x} target". *Thin Solid Films* **516**, 5758–5762 (2008).

[165] N. Yamada, T. Hitosugi, J. Kasai, N. L. H. Hoang, S. Nakao, Y. Hirose, T. Shimada, and T. Hasegawa. "Direct growth of transparent conducting Nb-doped anatase TiO_2 polycrystalline films on glass". *Journal of Applied Physics* **105**, 123702 (2009).

[166] K. Tonooka, T.-W. Chiu, and N. Kikuchi. "Preparation of transparent conductive TiO_2:Nb thin films by pulsed laser deposition". *Applied Surface Science* **255**, 9695–9698 (2009).

[167] S.-H. Peng, C.-C. Kuo, M.-C. Li, S.-H. Tsai, and C.-C. Lee. "Nb-doped TiO_2 transparent conducting coating by pulse DC magnetron co-sputtering". *Proceedings of SPIE* **7786**, 77860R1–77860R8 (2010).

[168] Y. Sato, Y. Sanno, C. Tasaki, N. Oka, T. Kamiyama, and Y. Shigesato. "Electrical and optical properties of Nb-doped TiO_2 films deposited by DC magnetron sputtering using slightly reduced Nb-doped TiO_{2-x} ceramic targets". *Journal of Vacuum Science & Technology A: Vacuum, Surfaces, and Films* **28**, 851 (2010).

[169] A. Fouda, K. Hazu, M. Haemori, T. Nakayama, A. Tanaka, and S. F. Chichibu. "Transparent semiconducting Nb-doped anatase TiO_2 films deposited by helicon-wave-excited-plasma sputtering". *Journal of Vacuum Science & Technology B: Microelectronics and Nanometer Structures* **29**, 011017 (2011).

[170] K.-H. Hung, P.-W. Lee, W.-C. Hsu, H. C. Hsing, H.-T. Chang, and M.-S. Wong. "Transparent conducting oxide films of heavily Nb-doped titania by reactive co-sputtering". *Journal of Alloys and Compounds* **509**, 10190–10194 (2011).

[171] M. Z. Atashbar, H. T. Sun, B. Gong, W. Wlodarski, and R. Lamb. "XPS study of Nb-doped oxygen sensing TiO_2 thin films prepared by sol-gel method". *Thin Solid Films* **326**, 238–244 (1998).

[172] C. Wang, J. Meinhardt, and P. Löbmann. "Growth mechanism of Nb-doped TiO_2 sol-gel multilayer films characterized by SEM and focus/defocus TEM". *Journal of Sol-Gel Science and Technology* **53**, 148–153 (2010).

[173] G. Q. Wang, W. Lan, M. L. Yu, G. J. Han, Y. Wang, Q. Su, and X. Q. Liu. "Optical and structural properties of TiO_2 films as a function of Nb doping concentration". *Journal of Materials Science: Materials in Electronics* **22**, 463–466 (2010).

[174] G. Q. Wang, W. Lan, G. J. Han, Y. Wang, Q. Su, and X. Q. Liu. "Effect of Nb doping on the phase transition and optical properties of sol-gel TiO_2 thin films". *Journal of Alloys and Compounds* **509**, 4150–4153 (2011).

[175] J. Liu, X. Zhao, L. Duan, M. Cao, H. Sun, J. Shao, S. Chen, H. Xie, X. Chang, and C. Chen. "Influence of annealing process on conductive properties of Nb-doped TiO_2 polycrystalline films prepared by sol-gel method". *Applied Surface Science* **257**, 10156–10160 (2011).

[176] J. Arbiol, J. Cerda, G. Dezanneau, A. Cirera, F. Peiro, A. Cornet, and J. R. Morante. "Effects of Nb doping on the TiO_2 anatase-to-rutile phase transition". *Journal of Applied Physics* **92**, 853–186 (2002).

[177] A. M. Ruiz, G. Dezanneau, J. Arbiol, A. Cornet, and J. R. Morante. "Insights into the Structural and Chemical Modifications of Nb Additive on TiO_2 Nanoparticles". *Chemistry of Materials* **16**, 862–871 (2004).

[178] H. Nemec, Z. Mics, M. Kempa, and P. Kuzel. "Tuning the Conduction Mechanism in Niobium-Doped Titania Nanoparticle Networks". *The Journal of Physical Chemistry C* **115**, 6968–6974 (2011).

[179] P. S. Archana, R. Jose, M. M. Yusoff, and S. Ramakrishna. "Near band-edge electron diffusion in electrospun Nb-doped anatase TiO_2 nanofibers probed by electrochemical impedance spectroscopy". *Applied Physics Letters* **98**, 152106 (2011).

[180] M. Yang, D. Kim, H. Jha, K. Lee, J. Paul, and P. Schmuki. "Nb doping of TiO_2 nanotubes for an enhanced efficiency of dye-sensitized solar cells". *Chemical Communications* **47**, 2032–2034 (2011).

[181] C. Das, P. Roy, M. Yang, H. Jha, and P. Schmuki. "Nb doped TiO_2 nanotubes for enhanced photoelectrochemical water-splitting." *Nanoscale* **3**, 3094–3096 (2011).

[182] S. L. Gojković, B. M. Babić, V. R. Radmilović, and N. V. Krstajić. "Nb-doped TiO_2 as a support of Pt and Pt-Ru anode catalyst for PEMFCs". *Journal of Electroanalytical Chemistry* **639**, 161–166 (2010).

[183] B. V. Crist. *Handbooks of Monochromatic XPS Spectra 2: Commerically Pure Binary Oxides*. XPS International (1997).

[184] J. Trincavelli and R. Van Grieken. "Peak-to-Background Method for Standardless Electron Microprobe Analysis of Particles". *X-ray Spectrometry* **23**, 254–260 (1994).

[185] C. D. Wagner, A. V. Naumkin, A. Kraut-Vass, J. W. Allison, C. J. Powell, and J. R. Rumble Jr. "NIST X-Ray Photoelectron Spectroscopy Database" (2003).

[186] P. A. DeSario, M. E. Graham, R. M. Gelfand, and K. A. Gray. "The effect of Nb substitution on synthesis and photo-response of TiO_2 thin films prepared by direct current magnetron sputtering". *Thin Solid Films* **519**, 3562–3568 (2011).

[187] T. G. Babich, A. V. Zagorodnyuk, G. A. Teterin, M. Y. Khodos, and A. P. Zhirnova. "Nb_2O_5-TiO_2 system". *Russian Journal of Inorganic Chemistry (English Translation)* **33**, 560–563 (1988).

[188] G. A. Semenov and S. I. Lopatin. "A Study of Evaporation in the TiO_2-Nb_2O_5 Oxide System by High-Temperature Mass-Spectrometry". *Russian Journal of Applied Chemistry* **74**, 901–906 (2001).

[189] A. Lalany, R. T. Tucker, M. T. Taschuk, M. D. Fleischauer, and M. J. Brett. "Axial resistivity measurement of a nanopillar ensemble using a cross- bridge Kelvin architecture". *Journal of Vacuum Science & Technology A: Vacuum, Surfaces, and Films* **31**, 031502 (2013).

[190] A. L. Beaudry, R. T. Tucker, J. M. LaForge, M. T. Taschuk, and M. J. Brett. "Indium tin oxide nanowhisker morphology control by vapour-liquid-solid glancing angle deposition." *Nanotechnology* **23**, 105608 (2012).

[191] R. T. Tucker, A. L. Beaudry, J. M. LaForge, M. T. Taschuk, and M. J. Brett. "Branched Nanowires and Method of Fabrication" (2013).

[192] D. B. Fraser and H. D. Cook. "Highly Conductive, Transparent Films of Sputtered $In_{2x}Sn_xO_{3y}$". *Journal of The Electrochemical Society* **119**, 1368–1374 (1972).

[193] C. W. Tang and S. A. VanSlyke. "Organic electroluminescent diodes". *Applied Physics Letters* **51**, 913–915 (1987).

[194] H. Kim, A. Pique, J. S. Horwitz, H. Mattoussi, H. Murata, Z. H. Kafafi, and D. B. Chrisey. "Indium tin oxide thin films for organic light-emitting devices". *Applied Physics Letters* **74**, 3444–3446 (1999).

[195] F. Yang, M. Shtein, and S. R. Forrest. "Controlled growth of a molecular bulk heterojunction photovoltaic cell". *Nature Materials* **4**, 37–41 (2004).

[196] K. Schulze, B. Maennig, K. Leo, Y. Tomita, C. May, J. Hupkes, E. Brier, E. Reinold, and P. Bauerle. "Organic solar cells on indium tin oxide and aluminum doped zinc oxide anodes". *Applied Physics Letters* **91**, 073521 (2007).

[197] G.-J. Wang, H.-T. Chen, and H. Yang. "Fabrication of Crystalline Indium Tin Oxide Nanobasket Electrodes using Aluminum Anodic Oxide Template". *Japanese Journal of Applied Physics* **47**, 5727–5729 (2008).

[198] F. Yang and S. R. Forrest. "Photocurrent generation in nanostructured organic solar cells". *ACS Nano* **2**, 1022–1032 (2008).

[199] H. Yumoto, J. Hatano, T. Watanabe, K. Fujikawa, and H. Sato. "Properties and surface morphology of indium tin oxide films prepared by electron shower method". *Japanese Journal of Applied Physics* **32**, 1204–1209 (1993).

[200] S. I. Castaneda, F. Rueda, R. Daz, J. M. Ripalda, and I. Montero. "Whiskers in indium tin oxide films obtained by electron beam evaporation". *Journal of Applied Physics* **83**, 1995–2002 (1998).

[201] Y. Q. Chen, J. Jiang, B. Wang, and J. G. Hou. "Synthesis of tin-doped indium oxide nanowires by self-catalytic VLS growth". *Journal of Physics D: Applied Physics* **37**, 3319–3322 (2004).

[202] A. Vomiero, S. Bianchi, E. Comini, G. Faglia, M. Ferroni, and G. Sberveglieri. "Controlled Growth and Sensing Properties of In_2O_3 Nanowires". *Crystal Growth & Design* **7**, 2500–2504 (2007).

[203] N. Kumar, O. Parajuli, M. Feng, J. Xu, and J.-i. Hahm. "Facile fabrication and biological application of tin-rich indium tin oxide nanorods". *Applied Physics Letters* **96**, 053705 (2010).

[204] J. Gao, R. Chen, D. H. Li, L. Jiang, J. C. Ye, X. C. Ma, X. D. Chen, Q. H. Xiong, H. D. Sun, and T. Wu. "UV light emitting transparent conducting tin-doped indium oxide (ITO) nanowires." *Nanotechnology* **22**, 195706 (2011).

[205] S.-T. Jean and Y.-C. Her. "Growth Mechanism and Photoluminescence Properties of In_2O_3 Nanotowers". *Crystal Growth & Design* **10**, 2104–2110 (2010).

[206] S. Takaki, Y. Aoshima, and R. Satoh. "Fabrication of Indium Tin Oxide Whiskers by Sputtering". *Japanese Journal of Applied Physics* **45**, 2714–2721 (2006).

[207] A. Walsh and C. R. A. Catlow. "Structure, stability and work functions of the low index surfaces of pure indium oxide and Sn-doped indium oxide (ITO) from density functional theory". *Journal of Materials Chemistry* **20**, 10438–10444 (2010).

[208] K. H. L. Zhang, A. Walsh, C. R. A. Catlow, V. K. Lazarov, and R. G. Egdell. "Surface energies control the self-organization of oriented In_2O_3 nanostructures on cubic zirconia". *Nano Letters* **10**, 3740–3746 (2010).

[209] X. S. Peng, G. W. Meng, X. F. Wang, Y. W. Wang, J. Zhang, X. Liu, and L. D. Zhang. "Synthesis of oxygen-deficient indium-tin-oxide (ITO) nanofibers". *Chemistry of Materials* **14**, 4490–4493 (2002).

[210] H. Sugata, S. Ohshio, and H. Saitoh. "Heteroepitaxy of In_2O_3 Whiskers Fabricated on Single Crystalline (001) Yittrium Stabilized Zirconia". *Japanese Journal of Applied Physics* **42**, 2786–2790 (2003).

[211] Q. Wan, Z. T. Song, S. L. Feng, and T. H. Wang. "Single-crystalline tin-doped indium oxide whiskers: Synthesis and characterization". *Applied Physics Letters* **85**, 4759–4761 (2004).

[212] H. S. Jang, D.-H. Kim, H.-R. Lee, and S.-Y. Lee. "Field emission from cone-like single crystalline indium tin oxide nanorods". *Materials Letters* **59**, 1526–1529 (2005).

[213] S. Y. Li, C. Y. Lee, P. Lin, and T. Y. Tseng. "Low temperature synthesized Sn doped indium oxide nanowires". *Nanotechnology* **16**, 451–457 (2005).

[214] R. Savu and E. Joanni. "Low-temperature, self-nucleated growth of indium-tin oxide nanostructures by pulsed laser deposition on amorphous substrates". *Scripta Materialia* **55**, 979–981 (2006).

[215] Q. Wan, P. Feng, and T. H. Wang. "Vertically aligned tin-doped indium oxide nanowire arrays: Epitaxial growth and electron field emission properties". *Applied Physics Letters* **89**, 123102 (2006).

[216] Q. Wan, M. Wei, D. Zhi, J. L. MacManus-Driscoll, and M. G. Blamire. "Epitaxial Growth of Vertically Aligned and Branched Single-Crystalline Tin-Doped Indium Oxide Nanowire Arrays". *Advanced Materials* **18**, 234–238 (2006).

[217] X.-Y. Xue, S.-L. Shi, Z.-X. Lin, K.-L. Zheng, Y.-A. Zhang, T.-L. Guo, and T.-H. Wang. "Optoelectronic characteristics and field emission properties of indium-doped tin oxide nanowire arrays". *Chinese Physics Letters* **24**, 3492–3494 (2007).

[218] R. Savu and E. Joanni. "Effect of processing conditions on the nucleation and growth of indium-tin-oxide nanowires made by pulsed laser ablation". *Journal of Materials Science* **43**, 609–613 (2007).

[219] A. Vomiero, M. Ferroni, E. Comini, G. Faglia, and G. Sberveglieri. "Insight into the Formation Mechanism of One-Dimensional Indium Oxide Wires". *Crystal Growth & Design* **10**, 140–145 (2010).

[220] C. H. Chang, M.-H. Hsu, P. Yu, H. C. Kuo, W. L. Chang, and W. C. Sun. "Novel indium-tin-oxide nano-whiskers for enhanced transmission of surface-textured silicon photovoltaic cells". *IEEE Photovoltaic Specialists Conference* pp. 000540–000543 (2009).

[221] C. H. Chiu, P. Yu, C. H. Chang, C. S. Yang, M. H. Hsu, H. C. Kuo, and M. A. Tsai. "Oblique electron-beam evaporation of distinctive indium-tin-oxide nanorods for enhanced light extraction from InGaN/GaN light emitting diodes." *Optics Express* **17**, 21250–21256 (2009).

[222] J. H. Park, H. K. Park, J. Jeong, W. Kim, B. K. Min, and Y. R. Do. "Wafer-scale growth of ITO nanorods by radio frequency magnetron sputtering deposition". *Journal of The Electrochemical Society* **158**, K131–K135 (2011).

[223] A. S. Alagoz and T. Karabacak. "Fabrication of Crystalline Semiconductor Nanowires by Vapor-Liquid-Solid Glancing Angle Deposition (VLS-GLAD) Technique". *MRS Proceedings* **1350** (2011).

[224] R. T. Tucker, A. L. Beaudry, J. M. LaForge, M. T. Taschuk, and M. J. Brett. "A little ribbing: Flux starvation engineering for rippled indium tin oxide nanotree branches". *Applied Physics Letters* **101**, 193101 (2012).

[225] A. L. Beaudry, J. M. LaForge, R. T. Tucker, P. Li, M. T. Taschuk, and M. J. Brett. "Flux Engineering for Indium Tin Oxide Nanotree Crystal Alignment and Height-Dependent Branch Orientation". *Crystal Growth & Design* **13**, 212–219 (2013).

[226] J. M. LaForge, T. L. Cocker, A. L. Beaudry, K. Cui, R. T. Tucker, M. T. Taschuk, F. A. Hegmann, and M. J. Brett. "Conductivity control of as-grown branched indium tin oxide nanowire networks". *Nanotechnology* **25**, 035701 (2014).

[227] M. T. Taschuk, R. T. Tucker, J. M. LaForge, A. L. Beaudry, M. R. Kupsta, and M. J. Brett. "Towards engineered branch placement: Unreal^{TM} match between vapour-liquid-solid glancing angle deposition nanowire growth and simulation". *Journal of Applied Physics* **114**, 244304 (2013).

[228] R. Park (editor). *Manual on the use of thermocouples in temperature measurement*. West Conshohocken, PA, 4th edition (1993).

[229] W. S. Rasband. *ImageJ*. National Institutes of Health, Bethesda, MA (1997–2005).

[230] G. S. Smith and R. L. Snyder. "F_N: A criterion for rating powder diffraction patterns and evaluating the reliability of powder-pattern indexing". *Journal of Applied Crystallography* **12**, 60–65 (1979).

[231] M. K. Fung, Y. C. Sun, A. M. C. Ng, X. Y. Chen, K. K. Wong, A. B. Djurišić, and W. K. Chan. "Indium tin oxide nanowires growth by dc sputtering". *Applied Physics A* **104**, 2–7 (2011).

[232] J. Zhou, Y. Ding, S. Z. Deng, L. Gong, N. S. Xu, and Z. L. Wang. "Three-Dimensional Tungsten Oxide Nanowire Networks". *Advanced Materials* **17**, 2107–2110 (2005).

[233] K. A. Dick, K. Deppert, M. W. Larsson, W. Seifert, L. Reine Wallenberg, and L. Samuelson. "Height-controlled nanowire branches on nanotrees using a polymer mask". *Nanotechnology* **18**, 035601 (2007).

[234] E. I. Givargizov. "Periodic instability in whisker growth". *Journal of Crystal Growth* **20**, 217–226 (1973).

[235] Y. Yuan and J. Pan. "The morphology and growth mechanism of TiC whisker prepared by chemical vapour deposition". *Journal of Materials Science* **33**, 5773–5780 (1998).

[236] H. Kohno and S. Takeda. "Periodic instability in growth of chains of crystalline-silicon nanospheres". *Journal of Crystal Growth* **216**, 185–191 (2000).

[237] J. X. Wang, S. S. Xie, Y. Gao, X. Q. Yan, D. F. Liu, H. J. Yuan, Z. P. Zhou, L. Song, L. F. Liu, W. Y. Zhou, and G. Wang. "Growth and characterization of axially periodic Zn_2SnO_4 (ZTO) nanostructures". *Journal of Crystal Growth* **267**, 177–183 (2004).

[238] H. Kohno and H. Yoshida. "Lévy-type complex diameter modulation in semiconductor nanowire growth". *Solid State Communications* **132**, 59–62 (2004).

[239] Y. Lilach, J.-P. Zhang, M. Moskovits, and A. Kolmakov. "Encoding morphology in oxide nanostructures during their growth". *Nano Letters* **5**, 2019–2022 (2005).

[240] X. M. Cai, A. B. Djurisic, M. H. Xie, C. S. Chiu, and S. Gwo. "Growth mechanism of stacked-cone and smooth-surface GaN nanowires". *Applied Physics Letters* **87**, 183103 (2005).

[241] L. Cao, B. Garipcan, J. S. Atchison, C. Ni, B. Nabet, and J. E. Spanier. "Instability and transport of metal catalyst in the growth of tapered silicon nanowires". *Nano Letters* **6**, 1852–1857 (2006).

[242] J. B. Hannon, S. Kodambaka, F. M. Ross, and R. M. Tromp. "The influence of the surface migration of gold on the growth of silicon nanowires". *Nature* **440**, 69–71 (2006).

[243] Y. Zhang, Y. Yan, and F. Zhu. "The Periodic Instability of Diameter of ZnO Nanowires via a Self-oscillatory Mechanism". *Nanoscale Research Letters* **2**, 492–495 (2007).

[244] Y. Yan, L. Zhou, J. Zou, and Y. Zhang. "Synthesis and growth discussion of novel ZnO nanotetrapods with pearl-necklace-shaped arms". *Applied Physics A* **94**, 559–565 (2009).

[245] M. Kolibal, R. Kalousek, T. Vystavel, L. Novak, and T. Sikola. "Controlled faceting in 110ł germanium nanowire growth by switching between vapor-liquid-solid and vapor-solid-solid growth". *Applied Physics Letters* **100**, 203102 (2012).

[246] M. Suzuki, K. Hamachi, H. Hara, K. Nakajima, K. Kimura, C.-W. Hsu, and L.-J. Chou. "Vapor-liquid-solid growth of Ge nanowhiskers enhanced by high-temperature glancing angle deposition". *Applied Physics Letters* **99**, 223107 (2011).

[247] H. Yumoto, T. Sako, Y. Gotoh, K. Nishiyama, and T. Kaneko. "Growth mechanism of vapor-liquid-solid (VLS) grown indium tin oxide (ITO) whiskers along the substrate". *Journal of Crystal Growth* **203**, 136–140 (1999).

[248] S. N. Mohammad. "Analysis of the Vapor-Liquid-Solid Mechanism for Nanowire Growth and a Model for this Mechanism". *Nano Letters* **8**, 1532–1538 (2008).

[249] J. Johansson, B. A. Wacaser, K. A. Dick, and W. Seifert. "Growth related aspects of epitaxial nanowires". *Nanotechnology* **17**, S355–S361 (2006).

[250] I. V. Markov. *Crystal Growth For Beginners*. World Scientific Publishing, 2nd edition (2003).

[251] D. Kashchiev. "Dependence of the growth rate of nanowires on the nanowire diameter". *Crystal Growth & Design* **6**, 1154–1156 (2006).

[252] V. G. Dubrovskii and N. V. Sibirev. "General form of the dependences of nanowire growth rate on the nanowire radius". *Journal of Crystal Growth* **304**, 504–513 (2007).

[253] E. J. Schwalbach and P. W. Voorhees. "Phase equilibrium and nucleation in VLS-grown nanowires." *Nano Letters* **8**, 3739–3745 (2008).

[254] P. Caroff, K. A. Dick, J. Johansson, M. E. Messing, K. Deppert, and L. Samuelson. "Controlled polytypic and twin-plane superlattices in III-V nanowires". *Nature Nanotechnology* **4**, 50–55 (2009).

[255] V. Schmidt, S. Senz, and U. Gösele. "Diameter-dependent growth direction of epitaxial silicon nanowires". *Nano Letters* **5**, 931–935 (2005).

[256] Z. W. Wang and Z. Y. Li. "Structures and energetics of indium-catalyzed silicon nanowires". *Nano Letters* **9**, 1467–1471 (2009).